Final Report: NASA Award Number, NNX07AR95G, entitled, "COMPARISON OF A - TRAIN CLOUD RETRIEVALS AND MULTI-INSTRUMENT ALGORITHM STUDIES".

For the period of August 15, 2007 – August 14, 2010

Principal Investigator: Steven Ackerman

Highlights:

This is the final report for grant NNX07AR95G. This funding has resulted in significant progress in understanding and developing cloud retrieval methods from active and passive sensors resulting in four peer-reviewed publications. The grant has helped supported the development of new collocation methods providing global, spatially co-register, active (CALIOP) and passive (MODIS and AIRS). Using this capability we have developed combined active and passive cloud retrievals, improved characterization of the MODIS cloud retrievals algorithms uncertainties with the final year of funding resulting in improved understanding of Marine cloud microphysics and the development of a combined CALIPSO and MODIS Aerosol retrieval. An overview of these accomplishments is now presented with the corresponding publications attached at the end of this report.

1. Collocation methods developed for MODIS and CALOP

The collocation methods developed provide the capability to identify the occurrence of Simultaneous Nadir Observations (SNO's), collocation of sounder, imager, and active remote sensed measurements on the NASA Earth Observation System (EOS), and collocation of the polar orbiting imager, sounder, and microwave measurements with geostationary observations. The algorithms are computationally efficient allowing for rapid global processing of global satellite data sets provided by the NASA Earth Observing System. This work has been published in JTECH. A copy of the manuscript is attached as part of this report (Nagle; Holz 2009).

2. Investigation of MODIS Cloud Top Height and cloud Detection using CALIOP

Using the collocated data set the MODIS cloud mask, effective radius, multilayer, phase, and cloud top height (pressure) have been investigated. The results identified significant differences between the CALIOP and MODIS cloud to height retrievals for thin cirrus and a systematic over-estimation of the MODIS cloud top heights in marine stratus regions. From these findings, modifications to the MODIS collection 5 retrievals algorithms are being investigated to improve the MODIS sensitivity to thin cirrus. A modification has been applied that significantly reduces the marine stratus high bias with the results being published in JGR-Atmospheres. A copy of the manuscript is attached as part of this report (Holz et al. 2008). In addition to cloud top height we leveraged the collocated observations to investigate the sensitivity of the MODIS cloud mask using lidar observations (CALIOP and HSRL). From this comparison we found the MODIS

cloud mask provides sensitivity to optically thin clouds with optical depths greater then approximately 0.4. This work is published in JTECH (Ackerman et al. 2008).

3. Investigation of the MODIS Cloud Microphysical Retrievals

The retrieval of cloud optical thickness (OD) is a critical property required to characterize the radiative impact of clouds on the earth's energy balance but has proven one of the more difficult properties to measure accurately. With the launch of CALIPSO in 2006, simultaneous active (CALIOP) and passive (MODIS) cloud OD are provided as part of the A-Train observations. A comparison between these retrievals finds significant systematic differences for single layer thin ice clouds (visible optical depth < 3) with the MODIS optical depths found be a factor of two larger then CALIPSO. Explanations for these differences are many, ranging from algorithm implementation to differences resulting from the physical assumption built into the MODIS and CALIOP OD retrieval methods. This work is continuing with support from the CALIPSO project.

4. Ice in Low Level Marine Clouds Investigated

Investigating low-level convective marine clouds using collocated CALIOP, CloudSat, and MODIS we found that a significant fraction (up to 20%) of these clouds in the mid and upper latitudes are composed of ice with a large fraction having an oriented signature as determined by CALIOP depolarization and backscatter cross-section measurements. In addition, we find that the ice frequency has a strong seasonal dependence in the north hemisphere that peaks in the northern winter in contrast to the southern hemisphere that lacks a seasonal dependence and has a much lower fraction of ice. This work is currently being prepared for publication.

5. Developed Combined CALIPSO and MODIS Aerosol Retrievals

This work aimed to both evaluate the MODIS and CALIOP Aerosol Optical Depth (AOD) retrieval and develop a combined MODIS/CALIOP AOD retrieval leveraging multi-spectral MODIS observations. We found a significant bias between CALIOP V3 and MODIS C005 AOD that is attributed to the CALIOP aerosol lidar ratio selection methodology. We demonstrated that the MODIS sensitivity to the aerosol fine/coarse ratio can be use to better constraint the aerosol lidar ratio and improve the CALIOP AOD retrieval. We present results from this combine approach. We find that the CALIOP total attenuated color ratio is correlated with the MODIS fine/coarse ratio providing an opportunity to improve CALIOP only AOD retrieval. This work has been recently accepted for publication with revisions in JGR-Atmospheres (Oo; Holz 2011).

Journal Publications:

Ackerman, S. A., R. E. Holz, R. Frey, E. W. Eloranta, B. Maddux, and M. J. McGill, 2008: Cloud detection with MODIS: Part II Validation. *Journal of Atmospheric and Oceanic Technology*,

Holz, R. E., S. A. Ackerman, F. W. Nagel, R. Frey, S. Dutcher, R. E. Kuehn, M. A. Vaughan, and B. A. Baum, 2008: Global MODIS Cloud Detection and Height Evaluated Using CALIOP. *Journal of Geophysical Research*.

Nagle, F. W., and R. E. Holz, 2009: Computationally Efficient Methods of Collocating Satellite, Aircraft, and Ground Observations. *Journal of Atmospheric and Oceanic Technology*, **26,** 1585-1595.

Oo, M., and R. E. Holz, 2011: Improving the CALIOP aerosol optical depth retrieval using combined MODIS-CALIOP observations. *J. Geophys. Res.*

JOURNAL OF GEOPHYSICAL RESEARCH, VOL. 113, D00A19, doi:10.1029/2008JD009837, 2008

Global Moderate Resolution Imaging Spectroradiometer (MODIS) cloud detection and height evaluation using CALIOP

R. E. Holz,[1] S. A. Ackerman,[1] F. W. Nagle,[1] R. Frey,[1] S. Dutcher,[1] R. E. Kuehn,[2] M. A. Vaughan,[2] and B. Baum[1]

Received 16 January 2008; revised 4 August 2008; accepted 26 August 2008; published 19 December 2008.

[1] A global 2-month comparison is presented between the Cloud-Aerosol Lidar with Orthogonal Polarization (CALIOP) and the Moderate Resolution Imaging Spectroradiometer (MODIS) for both cloud detection and cloud top height (CTH) retrievals. Both CALIOP and MODIS are part of the NASA A-Train constellation of satellites and provide continuous near-coincident measurements that result in over 28 million cloud detection comparisons and over 5 million CTH comparisons for the months of August 2006 and February 2007. To facilitate the comparison, a computationally efficient and accurate collocation methodology is developed. With the collocated MODIS and CALIOP retrievals, nearly instantaneous comparisons are compiled regionally and globally. Globally, it is found that the MODIS 1-km cloud mask and the CALIOP 1-km averaged layer product agreement is 87% for cloudy conditions for both August 2006 and February 2007. For clear-sky conditions the agreement is 85% (86%) for August (February). The best agreement is found for nonpolar daytime and the poorest agreement in the polar regions. Differences in cloud top heights depend strongly on cloud type. Globally, MODIS underestimates the CTH relative to CALIOP by 1.4 ± 2.9 km for both August 2006 and February 2007. This value of 1.4 km is obtained using the CALIOP 1 km layer products. When compared to the CALIOP 5-km products, the differences increase to −2.6 ± 3.9 km as a result of CALIOP's increased sensitivity to optically thin cirrus. When only high clouds above 5 km are considered, the differences are found to be greater than 4 km with individual comparisons having differences larger than 10 km. These large differences (>10 km) represent approximately 16% of the nonpolar high cloud retrievals (>5 km). For high clouds it is found that MODIS retrieves a cloud top height for 90% of the clouds detected by the CALIOP 5-km layer products. The large MODIS underestimates for optically thin cirrus occur for cases when MODIS reverts to a window brightness temperature retrieval instead of CO_2 slicing. A systematic bias is found for marine low-level stratus clouds, with MODIS overestimating the CTH by over 1 km in dense marine stratocumulus regions. The cause of the bias was identified in the MODIS Collection 5 algorithm; an application of a modified algorithm reduced this bias.

Citation: Holz, R. E., S. A. Ackerman, F. W. Nagle, R. Frey, S. Dutcher, R. E. Kuehn, M. A. Vaughan, and B. Baum (2008), Global Moderate Resolution Imaging Spectroradiometer (MODIS) cloud detection and height evaluation using CALIOP, *J. Geophys. Res.*, *113*, D00A19, doi:10.1029/2008JD009837.

1. Introduction

[2] Understanding the impact of clouds on the Earth's radiation balance and detecting changes in the amount and distribution of global cloud cover requires an accurate global cloud climatology with well-characterized uncertainties. To meet this challenge, significant effort has been given to generating climate quality long-term cloud data sets using over 30 years of polar-orbiting infrared satellite measurements [*Ackerman et al.*, 1998; *Heidinger*, 2003; *Rossow and Schiffer*, 1999; *Wylie and Menzel*, 1999] with plans to continue the cloud record using the next generation of polar orbiting sensors. A "Climate Quality" climatology requires that both the uncertainties and the physical sensitivities are quantified and are smaller than the expected climate signature. Uncertainties resulting from the fundamental measurement (instrument noise, radiometric bias) can be determined analytically as part of the retrieval process [*Heidinger*, 2003]. However, these uncertainties account for only part of the total error budget. The more difficult uncertainties result from physical approximations used to develop the retrieval methodology. Additionally, further uncertainties

[1]Cooperative Institute for Meteorological Satellite Studies, University of Wisconsin-Madison, Madison, Wisconsin, USA.
[2]Science Systems and Applications, Inc., Hampton, Virginia, USA.

0148-0227/08/2008JD009837$09.00

may be introduced by the ancillary data sets used in the retrieval process, such as land emissivity and atmospheric profiles of temperature, water vapor, and ozone. The difficulty in characterizing these uncertainties is compounded by their strong regional dependence. For example, an infrared (IR) cloud height retrieval algorithm may work very well near the equator, yet be very uncertain over the polar regions owing to the lack of thermal contrast between the clouds and the surface. Assessing these uncertainties requires comparisons with sets of well-characterized measurements having global extent. This study provides such an assessment using global lidar measurements provided by the Cloud-Aerosol Lidar with Orthogonal Polarization (CALIOP).

[3] Significant effort has been given to characterizing the uncertainties and sensitivities of various global cloud climatologies using independent evaluation measurements from ground, aircraft, and more recently satellite platforms [*Ackerman et al.*, 2008; *Holz et al.*, 2006; *Kahn et al.*, 2007a; *Mahesh et al.*, 2004; *Min et al.*, 2004; *Thomas et al.*, 2002; *Zhao and Girolamo*, 2006]. These comparisons have provided important insight but have been limited by the relatively small number of comparisons and the lack of global coverage. Recent advances in active remote sensing technology have provided satellite-based lidar and radar measurements. For example, the Geosciences Laser Altimeter System (GLAS) was launched on the Ice, Cloud and Land Elevation Satellite (ICESat) platform in January 2003, and provided the first satellite-based atmospheric lidar measurements [*Abshire et al.*, 2005]. The GLAS measurements provided a valuable resource for evaluating cloud retrievals [*Ackerman et al.*, 2008; *Mahesh et al.*, 2004; *Wylie et al.*, 2007]. In a comparison of GLAS to HIRS, the HIRS global cloud frequency was 5% greater than GLAS and HIRS underestimated CTH with differences larger than 4 km in the tropics. The comparison was done statistically because of the infrequent intersections of GLAS with the sun synchronous NOAA polar-orbiting satellites carrying HIRS.

[4] The successful launch of the CALIOP onboard NASA's Cloud Aerosol Lidar and Infrared Pathfinder Satellite Observation (CALIPSO) satellite provides vertically resolved measurements of both cloud and aerosols with near coincident sampling to MODIS on the Aqua satellite. This new data set provides a new opportunity to evaluate the passive retrievals. A recent 5-day evaluation of the Atmospheric Infrared Sounder (AIRS) cloud retrievals using CALIOP found significant biases in the cloud height determination compared to CALIOP for thin cirrus but with smaller biases for low clouds [*Kahn et al.*, 2007b]. When accurately collocated with MODIS, CALIOP provides a global evaluation data set that can be compared directly to the MODIS passive cloud retrievals. The resulting evaluation of the MODIS cloud mask and cloud top height (CTH) retrievals are presented in this paper.

[5] This paper is organized as follows. A description of the MODIS and CALIOP cloud retrievals is provided in section 2 including a discussion of the MODIS/CALIOP collocation algorithm developed for the comparison. The results of 2 months (August 2006 and February 2007) of global collocated CALIOP and MODIS comparisons of cloud detection and cloud top height are presented in section 3, followed by a detailed discussion of the results. Conclusions are then presented in section 4.

2. Measurements and Collocation

[6] The NASA Earth Observing System (EOS) A-Train [*Stephens et al.*, 2002] is a series of satellites flying in close formation carrying passive and active sensors that provide a diverse suite of coincident measurements that characterize the three-dimensional structure of the Earth's atmosphere. This paper focuses on comparing the active sensor cloud profiles provided by CALIOP onboard CALIPSO with the passive sensor cloud products from MODIS on the Aqua platform. There are significant differences in the spatial sampling between MODIS and CALIOP that are discussed later in this section. Furthermore, there are also temporal sampling differences as the CALIPSO orbit trails MODIS on Aqua by approximately 80 s. To minimize the uncertainties resulting from the spatial and temporal sampling differences, a collocation methodology has been developed and as outlined in Appendix A. Accurate collocation provides the ability to perform direct comparisons between CALIOP and MODIS ground-projected instantaneous field-of-view (GIFOV) measurements. Descriptions of the MODIS and CALIOP instruments, and of their respective Level-2 cloud retrieval algorithms, are now presented.

2.1. MODIS

[7] MODIS (Moderate Resolution Imaging Spectroradiometer) measures radiances at 36 wavelengths, including infrared and visible bands with spatial resolution 250 m to 1 km. The cloud mask is part of the MODIS Cloud Product Suite and is described by *Ackerman et al.* [2008, 1998], *Frey et al.* [2008], *King et al.* [2003], and *Platnick et al.* [2003].

[8] The MODIS cloud mask algorithm uses a series of sequential tests on the passive reflected solar and infrared observations to indicate a level of confidence that MODIS is observing a clear-sky scene. Produced for the entire globe, day and night, and at 1-km resolution, the cloud mask algorithm employs up to nineteen MODIS spectral bands to maximize reliable cloud detection. In addition, a 250-m mask is derived from the two 250 m resolution bands (0.65 and 0.86 μm).

[9] As cloud cover can occupy less than the full pixel (i.e., subpixel clouds), the MODIS cloud mask is designed for varying degrees of clear sky confidence; that is, it provides more information than a simple yes/no decision. The cloud mask consists of 48 bits of output per pixel and includes information on individual cloud test results, the processing path, and ancillary information (e.g., land/sea tag). The first two bits of the mask summarize the results from all individual tests by classifying cloud contamination in every pixel of data as either confident clear, probably clear, uncertain/probably cloudy, or cloudy.

[10] The MODIS cloud mask algorithm identifies several conceptual domains according to surface type and solar illumination including land, water, snow/ice, desert, and coast for both day and night. Once a pixel is assigned to a particular domain, thereby defining an algorithm path, a series of threshold tests attempts to detect the presence of clouds or optically thick aerosol in the instruments FOV. Each test returns a confidence level that the pixel is clear, ranging in value from 1 (high confidence clear) to 0 (low

Table 1. CALIOP Instrument Characteristics

Characteristic	Value
Laser wavelengths	532,1064 nm
Rep rate	20.16 Hz
Pulse length	20 nsec
Beam divergence	100 urad
Telescope IFOV	130 μrad
Surface GIFOV diameter	70 m

confidence clear). There are several types of threshold tests used to detect various cloud conditions. Those capable of detecting similar cloud conditions are grouped together. It should be noted that few, if any, spectral tests are completely independent. *Ackerman et al.* [2008] compared the MODIS cloud mask with various ground based and aircraft based active systems and found agreement approximately 85% of the time. Through comparison with high-spectral resolution lidar, *Ackerman et al.* [2008] found that over land the optical depth detection limit of MODIS is approximately 0.3 to 0.4.

[11] Cloud top pressure (CTP) is derived using 5 thermal infrared bands (both day and night) at 5 km spatial resolution by applying the CO_2 slicing technique as discussed in detail by *Menzel et al.* [2008]. The CO_2 slicing technique is used to infer CTP and effective cloud amount for opaque and nonopaque midlevel to high-level single layer clouds. Retrievals are derived from ratios of differences in radiances between cloudy and clear-sky regions at two nearby wavelengths. In MODIS operational processing, CTP is calculated for the following ratio pairs: 14.2 μm/13.9 μm; 13.9 μm/13.6 μm, 13.6 μm/13.3 μm, and 13.9 μm/13.3 μm. The cloud emissivity is assumed to be identical in the spectral band pairs. The optimal CTP is selected that best satisfies the forward radiative transfer calculations [*Menzel et al.*, 2008]. The fundamental CO_2 slicing retrievals are pressure and effective emissivity (defined as cloud emissivity multiplied by cloud fraction) applied to a 5×5 pixel array, for a product at a nominal resolution of 5 km^2 where at least 4 of the 25 pixels must be flagged as probably cloudy or cloudy by the cloud mask. The algorithm uses analyses from the Global Data Assimilation System (GDAS) meteorological profile product (1° spatial and 6 h temporal resolution), and the National Center for Environmental Prediction (NCEP) Reynolds Blended Sea Surface Temperature (SST) product to calculate the required clear-sky radiances. Once the CTP is determined for a given 5 km^2 FOV, a cloud top height (CTH) and cloud temperature is determined using the NCEP Global Forecast System (GFS). Differences between model-derived and measured clear-sky radiances are mitigated with a radiance bias adjustment to avoid height assignment errors [*Menzel et al.*, 2008].

[12] Error analyses in CTP/CTH retrievals from the CO_2 slicing method have been investigated in several studies [*Hawkinson et al.*, 2005; *Holz et al.*, 2006; *Naud et al.*, 2004; *Smith and Platt*, 1978; *Wielicki and Coakley*, 1981]. Cloud height accuracy increases as the observed cloud signal (the clear sky minus the measured radiance) increases for a FOV. For clouds at pressures greater than 700 hPa (i.e., close to the surface), the signal-to-noise ratio decreases, thereby precluding application of the method. For multilayer clouds, CO_2 slicing produces a CTP for the radiative mean of the two clouds, thus misrepresenting the height of both. For low-level clouds, the 11-μm infrared window brightness temperature is used to determine a cloud top temperature assuming the cloud is opaque, and a cloud top pressure is assigned by comparing the measured brightness temperature to that calculated using a simple radiative transfer model using NCEP (GDAS) temperature and humidity profiles. To date, comparisons of the CO_2 slicing method with active sensors have been limited in scope, either to a field campaign or a limited geographic region.

2.2. CALIOP

[13] The Cloud-Aerosol Lidar with Orthogonal Polarization (CALIOP) instrument aboard CALIPSO uses a diode-pumped Nd:YAG laser transmitting at wavelengths of 1064 and 532 nm. In addition to range-resolved measurements of backscatter intensity at each of the two wavelengths, CALIOP also measures linear depolarization ratios at 532 nm, using polarization sensitive optics in the receiver to separate the backscattered radiation into components perpendicular and parallel to the polarization vector of the linearly polarized output of the laser transmitter [*Winker et al.*, 2004, 2007]. CALIOP provides nadir only measurements. Table 1 presents the instrument transmitter and receiver characteristics.

[14] A significant amount of preprocessing is conducted onboard CALIOP before the data is downlinked to the receiving stations. This includes vertical and spatial averaging of the raw lidar profiles, with the amount of averaging a function of altitude above mean sea level. At the maximum resolution, the CALIOP surface footprint has a horizontal spacing of ~333 m with a vertical resolution of 30 m. This resolution is only available for those portions of the profiles lower than 8.2 km. Above 8.2 km the vertical and horizontal averaging varies according to the specifications presented in Table 2. The raw data received from CALIOP are geolocated and calibrated, so that Level 1 profiles of attenuated backscatter coefficients can be generated [*Reagan et al.*, 2002]. The Level-2 cloud products are then derived directly from the Level 1 profile products. To identify layer boundaries, a feature finder is used to separate legitimate features of interest from the noise and calibration uncertainties associated with the Level 1 attenuated backscatter profiles [*Vaughan et al.*, 2004]. Just as the MODIS cloud mask uses detection thresholds, the sensitivity and accuracy of the CALIOP feature finder is dependent on the amount of averaging applied and the threshold levels used to differentiate between noise excursions and genuine atmospheric features. Unlike passive measurements, the active CALIOP measurements resolve the vertical profile with a signal intensity measured at each range interval, allowing for accurate vertical detection sensitivity. The ability for the Level-2 feature finder to detect a feature is thus additionally dependent on both the feature's backscatter intensity and the magnitude of the background signal. The signal at the receiver is a function of the intensity of the backscatter and the attenuation of the atmosphere between the layer of interest and the instrument. For this reason, the sensitivity of the feature finder is not a constant. Fortunately, for this comparison the primary interest is the first layer detected by CALIOP. For this layer, the only attenuation is from molecules and ozone, and the influence of each is small at 532 nm.

[15] The total intensity of the background signal measured by the lidar is dependent on the detector noise,

Table 2. CALIOP Vertical and Horizontal Averaging

Altitude (km)	Horizontal Resolution (km)	Vertical Resolution (m)
31.1–40	5.0	300
20.2–30.1	1.67	180
8.2–20.2	1.0	60
−0.5–8.2	0.33	30

receiver instantaneous field-of-view (IFOV) and width of the spectral filter used to reduce solar background energy scattered into the receiver. For daylight operations the solar background signal dominates the total background signal, decreasing the CALIOP sensitivity to optically thin clouds.

[16] Once a feature is detected, the type is determined using multidimensional probability functions to distinguish clouds from aerosol layers [*Liu et al.*, 2004]. This determination is made using the layer center altitude, the layer mean 532 nm attenuated backscatter and the ratio between the 532 nm and 1064 nm channels (color ratio). A confidence function based on these two measurements is used to determine the probability of the layer containing aerosols or cloud. Once the determination has been made, the layer properties are recorded in separate output files. For this investigation, only the cloud property files are used. As will be discussed, uncertainties in the CALIOP determination of cloud versus aerosol can impact the MODIS evaluation.

[17] Averaging the CALIOP measurements increases the signal to noise, thus increasing the feature finder's sensitivity to optically thin aerosol and cloud layers, but at the cost of reduced spatial and vertical resolution. CALIOP employs a nested, multigrid averaging and detection scheme that searches for layers at horizontal resolutions of 5 km, 20 km, and 80 km. The layers detected during these successive searches are all reported in the 5-km layer products. If a layer is detected within a profile averaged to a 5-km horizontal resolution, the data in that region are subsequently analyzed at progressively finer resolutions of 1 km and 333 m. Layers detected at these higher spatial resolutions are recorded in the 1-km and 333-m cloud layer files. If the backscatter return is too weak to be detected by the 1-km or 333-m averages, the cloud layer will only be reported in the lower resolution files. At the highest resolution, approximately 3–4 CALIPSO profiles will fall within a single MODIS 1-km pixel. At the 5-km resolution, the CALIOP data are undersampled relative to the MODIS 1-km pixel, presenting an interesting problem for comparing the measurements. Using the 5-km cloud boundary file maximizes the CALIOP sensitivity to thin cirrus, but can lead to increased uncertainty because of the sampling differences if the cloud features are smaller than the CALIOP 5-km sampling. To correctly represent the full layer profile information in the 5-km layer products it is necessary to merge the 1-km and 5-km layer products since the 5-km layer products do not always contain all layers detected by CALIOP. The layer products are merged into a new 5 km mask filled using both the CALIOP 5 km and 1-km products. New 5-km cloud boundaries were then generated from this mask. In contrast, the high spatial resolution 333-m data, which have reduced cloud sensitivity and are only available below 8.2 km, oversamples the 1-km MODIS pixel, enabling investigation of subpixel cloud features. The CALIOP retrieval products used in the comparison was version V1–10.

2.3. Collocation and Evaluation Methodology

[18] To avoid sampling regions of the MODIS swath affected by sun glint, the CALIPSO orbit has a slightly different inclination relative to Aqua, resulting in CALIPSO slowly precessing across the MODIS swath crossing the Aqua nadir position near the poles. Comparisons require that both the MODIS pixel transected by CALIOP be identified along with the associated CALIOP shots within the selected MODIS pixel. An accurate and computationally efficient collocation process has been developed to facilitate global comparisons of the MODIS and CALIOP cloud retrievals (see Appendix A). Figure 1 presents a graphical representation of the different combination of the MODIS and CALIOP spatial resolutions: a MODIS 250-m resolution broken cloud image is layered under simulated MODIS 1-km and 5-km footprints to illustrate the importance of accounting for spatial sampling differences between CALIOP and MODIS.

[19] In this study there are three combinations of CALIOP and MODIS spatial resolutions. For MODIS, the cloud mask is generated at 1-km resolution while the cloud top heights are retrieved using a 5 × 5 group of 1-km pixels. For CALIOP, the cloud layer products are available at 333-m, 1-km, 5-km, 20-km, and 80-km horizontal resolutions. Figure 1b presents the collocation geometry for the MODIS 1-km cloud mask and the CALIOP 330-m and 1-km retrievals. In this configuration the MODIS 1-km GIFOV is the "reference" with multiple CALIOP measurements

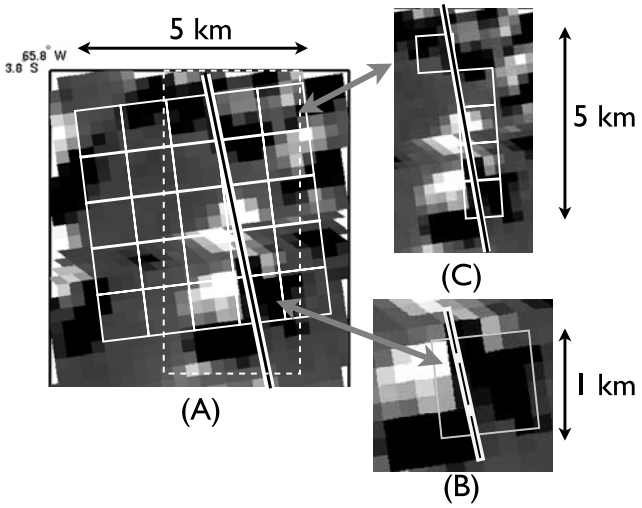

Figure 1. MODIS 0.855 μm MODIS image is overlaid with the three collocation geometries. The surface footprint of CALIOP is presented as the white and black line. (a) The 5-km MODIS footprint (large single box) with the MODIS 1-km footprint geometry (small boxes). (b) The 1-km MODIS GIFOV collocated with the 330-m CALIOP measurements. There are approximately 3 CALIOP shots within the 1-km footprint. (c) Collocation geometry for the 5 km CALIOP averaged retrieval collocated with the 1-km MODIS data. For case C, there are multiple MODIS GIFOV for each CALIOP retrieval.

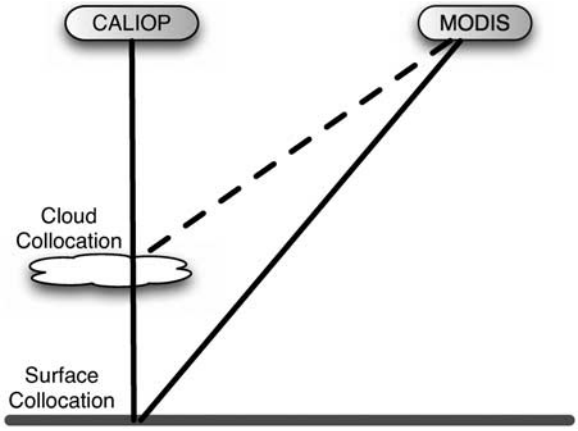

Figure 2. Geometry of the cloud height dependence on the MODIS/CALIOP collocation is presented. The dashed line represents the MODIS cloud collocated scan position while the solid line is the ground collocation.

within the MODIS GIFOV. The CALIOP beam width is approximately 90 m and does not sample the entire MODIS 1 km GIFOV. The collocation of the CALIOP 5 km averaged cloud products is presented in Figure 1c. For this case, multiple MODIS 1-km GIFOV are collocated with the single 5-km CALIOP averaged retrieval which now serves as the reference. In this configuration multiple MODIS GIFOVs are collocated for a single CALIOP retrieval.

[20] The collocation geometry for the MODIS cloud top height comparison with CALIOP is presented in Figure 1a. The collocation geometry is similar to that in Figure 1b but now the MODIS footprint is 5 × 5 km. For the CALIOP full resolution 330-m retrievals, up to 16 CALIOP cloud heights can fall within a single MODIS 5-km FOV. Because the width of the CALIOP footprint does not change with averaging, the sampling percentage of the MODIS 5-km scenes sampled by CALIOP is significantly smaller than the samples within the MODIS 1-km GIFOV. Uncertainties in the comparison resulting from the spatial mismatch need to be considered when interpreting the cloud top height comparisons.

[21] Because CALIOP does not follow the nadir flight track of Aqua, there is a parallax effect resulting in a CTH dependence on the collocation as illustrated in Figure 2. The CTH dependence on the collocation can result in a shift/offset of more than 5 pixels compared to the surface collocation. The collocation algorithm accounts for this offset using the CALIOP CTH. The parallax corrected collocation is presented in this paper.

3. Results

[22] Two months (August 2006 and February 2007) of global collocated MODIS and CALIOP cloud detection and CTH retrievals were compared. The 2 months of collocated MODIS/CALIOP comparisons results in approximately 28 million GIFOV; the 5 km CTH retrievals include over 5 million cases. The selection of a month each in summer and winter allows for the investigation of seasonal changes on the MODIS cloud mask and height detection. The results have been separated by month and include global and regional statistics of the agreement with CALIOP.

3.1. Cloud Mask

[23] The MODIS 1-km cloud mask was evaluated using the collocated CALIOP Level-2 1-km, and 5-km cloud layer retrievals. The MODIS cloud mask results are compared with CALIOP and the results presented as a fractional agreement between the two systems. At the extremes, there are two cases: (1) if the MODIS cloud mask agrees perfectly with CALIOP, the fractional agreement will be one, while (2) no agreement results in a fraction of zero.

[24] The global results of the cloud mask comparison for both the 1-km and 5-km CALIOP cloud products for August 2006 and February 2007 are presented in Table 3. For the comparison, a MODIS cloud mask result is considered cloudy if the cloud mask returns confident cloud or probably cloudy, while a MODIS pixel is defined clear if the MODIS cloud mask returns probably clear or confidently clear. Only MODIS pixels where all the collocated CALIOP retrievals are identical (i.e., either all clear or all cloudy) are included in the statistics in Table 3. As a result of this requirement, approximately 7% of the collocated scenes are not included in the statistics.

[25] The results for August 2006 and February 2007 are separated by clear and cloudy FOVs as determined by CALIOP in columns 2–4 of Table 3. Comparisons of MODIS with both 1-km and 5-km (shown in parentheses)

Table 3. Fractional Agreement That a Clear/Cloudy Scene was Consistently Identified by Both MODIS and CALIOP Instruments, During the Periods August 2006 and February 2007[a]

	August 2006 Clear	August 2006 Cloudy	February 2007 Clear	February 2007 Cloudy
Global CALIOP 1 km (5 km)	0.85 (0.75)	0.87 (0.85)	0.86 (0.77)	0.87 (0.84)
Nonpolar ocean CALIOP 1 km (5 km)	0.87 (0.83)	0.92 (0.86)	0.88 (0.79)	0.92 (0.86)
Nonpolar land CALIOP 1 km (5 km)	0.90 (0.86)	0.85 (0.78)	0.82 (0.74)	0.85 (0.81)
Northern midlatitude CALIOP 1 km (5 km)	0.89 (0.82)	0.88 (0.85)	0.78 (0.68)	0.91 (0.89)
Tropics CALIOP 1 km (5 km)	0.88 (0.84)	0.90 (0.83)	0.89 (0.86)	0.87 (0.80)
Southern midlatitude CALIOP 1 km (5 km)	0.87 (0.81)	0.94(0.92)	0.88 (0.81)	0.93 (0.90)
Arctic > 60° latitude	0.74 (0.62)	0.91 (0.92)	0.83 (0.66)	0.72 (0.76)
Antarctic < −60° latitude	0.79 (0.57)	0.71 (0.75)	0.92 (0.87)	0.88 (0.86)
Northern midlatitude day/night CALIOP 1 km	0.91/0.87	0.88/0.88	0.77/0.80	0.92/0.89
Tropics day/night CALIOP 1 km	0.89/0.86	0.89/0.90	0.90/0.86	0.86/0.87
Southern midlatitude day/night CALIOP 1-km	0.91/0.84	0.93/0.94	0.91/0.86	0.93/0.94

[a]Columns 2–5 show the comparison results for clear and cloudy scenes as determined CALIOP. The first eight rows show the impact of CALIOP averaging over 1 km, and the 5-km averaging in parentheses. The bottom three rows show the results of regional day and night comparisons.

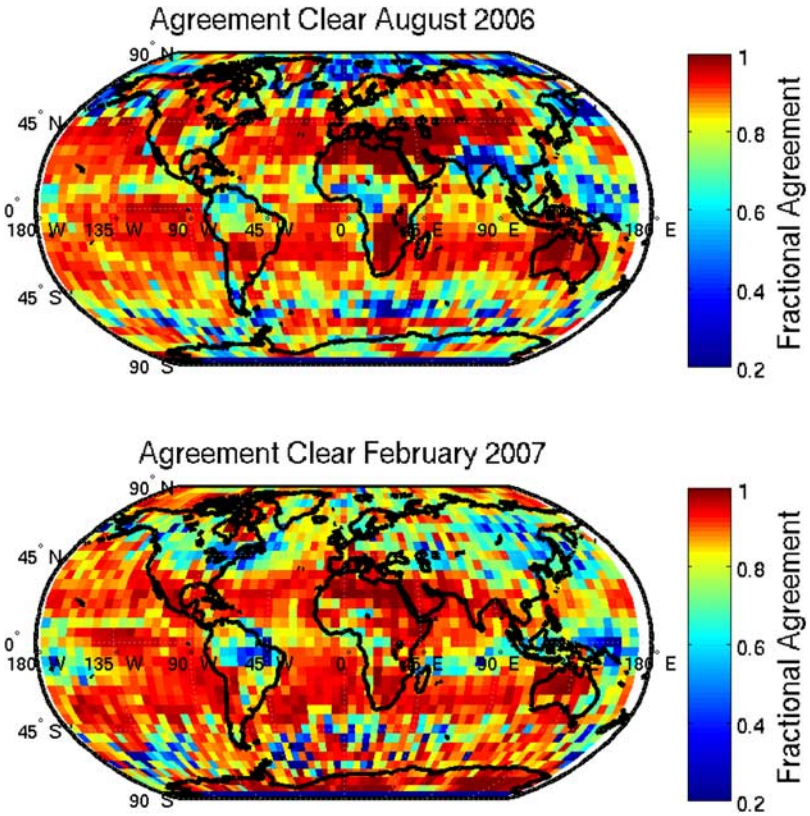

Figure 3. Fractional agreement between the MODIS 1-km and CALIOP 1-km cloud mask for clear scenes is presented. The fractional agreement is calculated here at 5-degree resolution. A grid cell with perfect MODIS agreement will have a fractional agreement of 1 (red), while regions of poorer agreement are colored blue.

CALIOP averaged cloud products are shown in rows 1–8, categorized by region. Rows 9–11 categorize the comparisons by day and night for the 1-km CALIOP and MODIS products.

[26] The global agreement between MODIS and CALIOP 1-km layer products in identifying clear scenes is greater than 85%, which is in general agreement with previous results [*Ackerman et al.*, 2008]. The agreement between both instruments in labeling a nonpolar ocean scene as cloudy is approximately 92% for either month. The best agreement for nonpolar land occurs in August at 90%, and drops to 85% for February. In August, warmer land surfaces and the reduced amount of surface snow/ice in the northern hemisphere both contribute to the increased contrast between clear and cloudy scenes, resulting in an improved clear scene classification. Compared to land, ocean surfaces exhibit less variation in temperature and albedo, and so the agreement over nonpolar oceans is similar for both months.

[27] In general, the MODIS cloud mask compares more favorably with the CALIOP 1-km averaging cloudy scenes than for clear scenes. This result is expected as the MODIS cloud mask was designed to be clear-sky conservative; that is, if there is uncertainty in the spectral tests, the MODIS cloud mask tends to label the scene as cloudy. The exception is the Arctic in February and the Antarctic in both months. In the Arctic region, CALIOP and MODIS agree that the scene is clear 74% of the time in August and 83% of the time in February; they agree that the scene is cloudy 91% of the time in August and only 72% in February. This suggests that during the summer months the MODIS cloud mask applied to the Arctic is biased cloudy while in the winter it is biased clear. [*Ackerman et al.*, 2008] also found better agreement in daylight conditions in the Arctic when comparing MODIS cloud detection to GLAS lidar on ICESAT. For the Antarctic the clear sky agreement is 79% for August and 92% for February; for cloudy scenes the agreement is 71% in August and 88% in February. Detection of a target requires a good contrast between the targets (clouds) and the background (surface). The difficulty of cold background scenes on the algorithm confidence to assign the pixel as clear is also seen in a comparison of the Northern midlatitude region, where the agreement in clear scenes is generally better in the summer month. The cold background scenes of the polar regions make cloud and clear scene discrimination problematic, particularly in the wintertime when only IR channels are available.

[28] Surprisingly, there is little difference in the results when separated by day and night. The agreement in cloud detection is generally within 0.03 for the day and night detection of each region.

[29] A similar comparison was conducted with the CALIOP 5-km layer products using the collocation geometry described in Figure 1c. When the comparisons are made between the MODIS and the CALIOP at 5-km resolution, the clear-sky agreement generally decreases, by 0.05 or

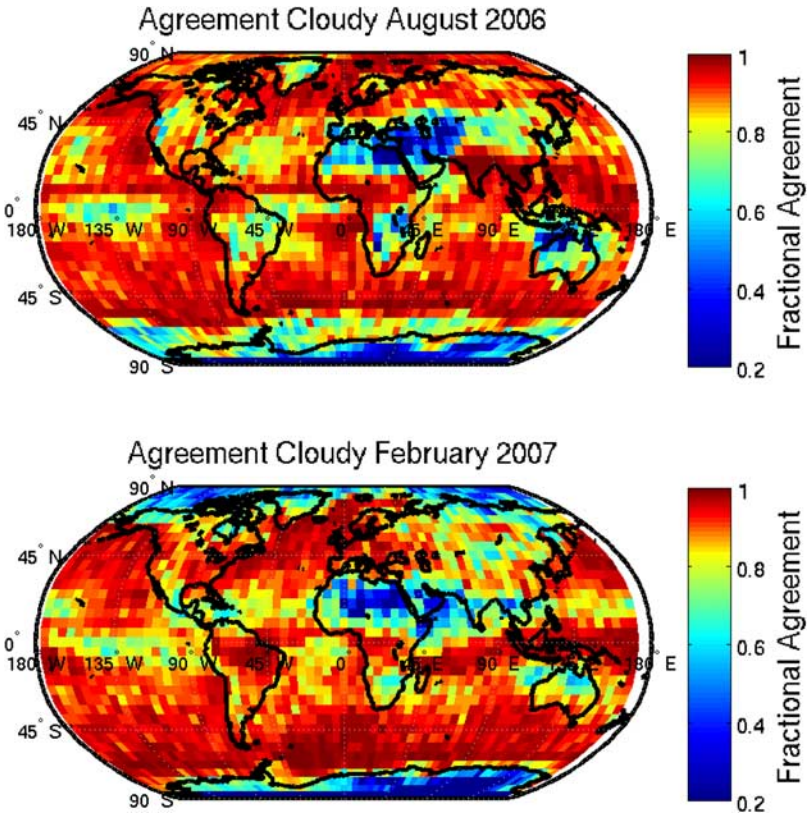

Figure 4. Fractional agreement between the MODIS 1-km and CALIOP 1-km cloud mask for cloudy scenes is presented. The fractional agreement is calculated here at 5-degree resolution. A grid cell with perfect MODIS agreement will have a fractional agreement of 1 (red), while regions of poorer agreement are colored blue.

more, in comparison to the 1-km resolution comparison. When the CALIOP algorithm makes use of an averaging over a 5-km swath, the detection method becomes more sensitive to thin cloud. Since the optical depth limit of cloud detection of MODIS is approximately 0.3–0.4 [*Ackerman et al.*, 2008], optically thin clouds flagged by CALIOP are likely to be labeled clear by MODIS, thereby decreasing the amount of agreement in scene identification. At the larger scale, CALIOP can detect high thin clouds, such as stratospheric clouds, and flag a previously clear scene in the 1-km product as cloudy. This is further discussed below. The increased sensitivity of CALIOP 5-km retrievals to thin cirrus will in general lower the agreement in cloudy scenes as MODIS will continue to label the scene as clear. The increased sensitivity of the CALIOP 5-km product causes the agreement with MODIS to decrease by a few percent for cloudy FOV when compared to the 1-km comparison as presented in Table 3.

[30] The MODIS cloud mask retrieval requires contrast between clear-sky and cloudy-sky conditions that are dependent on both surface and atmospheric properties, and can have significant regional variation. To investigate the regional performance of the cloud mask, the collocated data was divided into five-degree grid cells with the results presented in Figures 3 and 4. While CALIOP and MODIS are in good agreement (i.e., better than 90%) over much of the world, there are regional variations. To help interpret these differences, Figure 5 shows the average cloud height determined from CALIOP for the month of August 2006 for those cases where CALIOP 5-km algorithm detected a cloud and MODIS flagged the scene as clear.

[31] As shown in Figure 3 for clear-sky conditions, MODIS shows disagreement with CALIOP immediately north of the coast of Antarctica. MODIS requires a snow/ice mask in its selection of thresholds. Incorrect scene identification leads to cloud detection errors, which likely contributes to the disagreement around the coast of Antarctica. In February, the disagreement in the midlatitude regions around Russia is associated with cold surfaces, causing misclassification by MODIS. In August, there is also a large difference over the Indian subcontinent that occurs during the summer monsoon season when there are few clear pixels; only a few hundred within a grid box instead of several thousands as in other grid boxes. Disagreement in clear classification also occurs in the periphery of high clouds, the Amazon and the maritime convection region near Indonesia.

[32] In general there is very good agreement in the regional classification of a cloudy scene (Figure 4). The largest differences occur over the polar regions during the winter when the MODIS retrievals rely on thermal methods over cold surfaces. Disagreement occurs over the Antarctica highlands (Figure 4), and Figure 5 indicates that the average height of these clouds missed by MODIS is greater than 12 km, and thus likely optically thin polar stratospheric clouds detected by CALIOP. Disagreement in cloud detec-

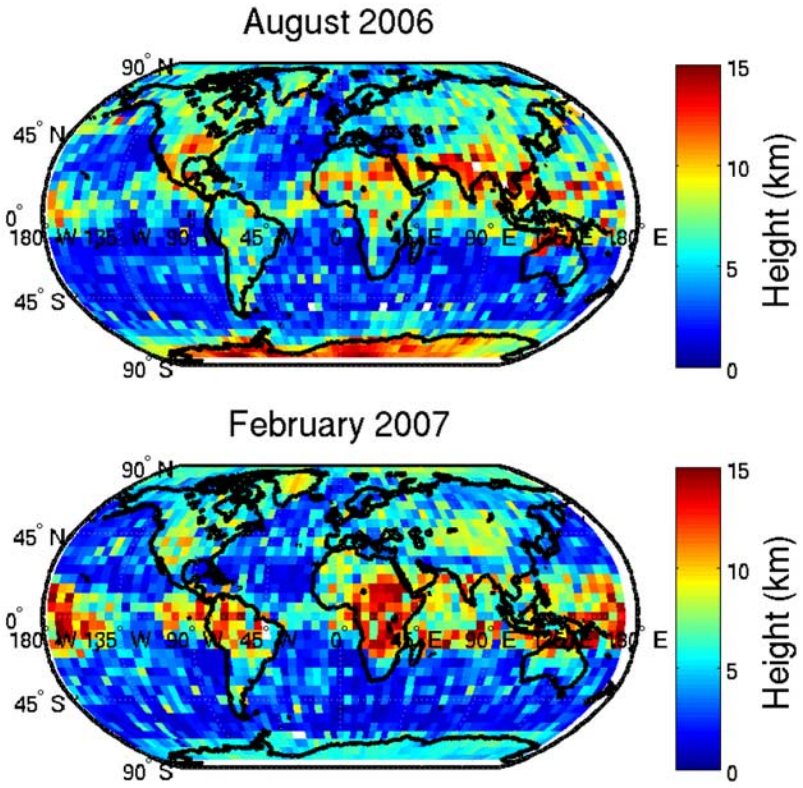

Figure 5. Average 5-km averaged CALIOP derived cloud height over a 5-degree region when the MODIS misses clouds detected by CALIOP.

tion in regions near the intertropical convergence zone (Figure 4) is likely due to optically thin cirrus that is undetected by MODIS (Figure 5). The disagreements in labeling a scene as cloudy also occur over the tropical deserts, caused by MODIS missing high thin cirrus and misclassification of aerosols as clouds by CALIOP. While the fraction of disagreement is large, the number of cases of cloudy scenes is generally small in comparison to other geographic regions. The next section further explores the differences the two approaches to cloud height.

3.2. Detecting High and Low Clouds

[33] Figure 5 shows the mean CTH, as determined by the CALIOP 5-km product, for cases when CALIOP detects a cloud and MODIS does not. This categorization reveals that differences in the tropical regions generally occur with high cloud. Disagreement in the summer monsoon region in August also is associated with high-level clouds, where the CALIOP has a greater sensitivity. The disagreement over the Siberian region in February occurs for clouds below 5 km. Also notice that during the Antarctic winter the mean cloud height of missed clouds is very high (15 km) and results from MODIS being insensitive to polar stratospheric clouds. A histogram of the CTH missed by MODIS is presented in Figure 6, with the results separated by the surface type. Over ocean the cloud mask primarily disagrees for low-level clouds while over land, the CTH distribution is more evenly distributed between high and low clouds. Over ocean, the disagreement between MODIS and CALIOP for low clouds occurs during both day and night, and can be attributed in part to spatial sampling differences for subpixel-scale cumulus. Investigation of individual granules supports this conclusion. An example subpixel-scale sampling differences is presented in Figure 1 with MODIS 1 km and CALIOP sampling overlaid over an observed 250 m MODIS reflectance image. Figure 6 reveals that for desert regions there are two modes in the missed CTH distribution; one peaks at 3 km and the other at 7 km. Investigation of

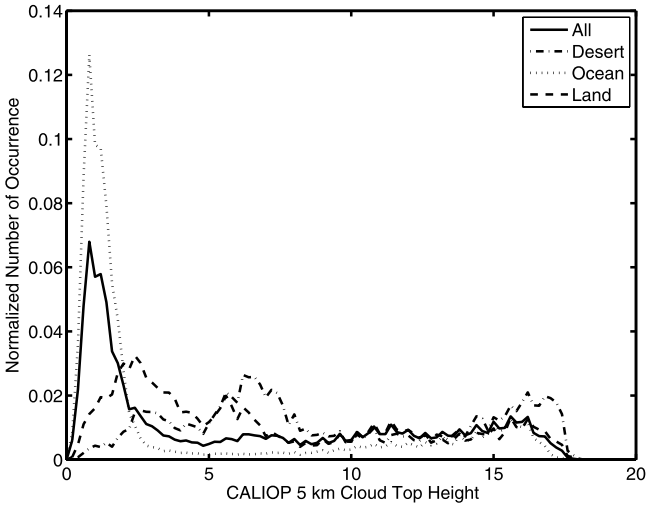

Figure 6. Normalized histogram of the CALIOP measured cloud top height for cases when the MODIS 1-km cloud mask misidentified the GIFOV as clear. The histograms are separated by the MODIS cloud mask land classification.

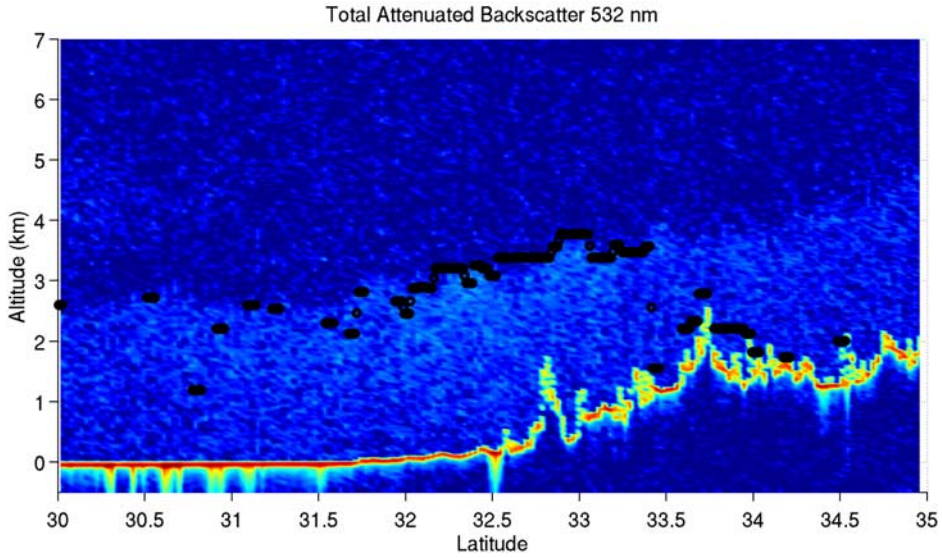

Figure 7. CALIOP attenuated backscatter profile with the CALIOP 5-km cloud top heights presented as black dots. Notice that CALIOP misidentifies the aerosol layer as cloud.

individual granules reveals that the higher mode in the desert distribution results from cases when the MODIS cloud mask misses thin cirrus. The lower mode at 3 km results from CALIOP incorrectly identifying thick aerosol layers as cloud with an example presented in Figure 7. This finding highlights the importance of considering the uncertainties in the evaluation measurements (CALIOP) when interpreting the comparison results.

3.3. Cloud Top Height

[34] Collocated 1-km and 5-km CALIOP CTH retrievals are compared with the MODIS 5-km cloud top pressure retrievals. Interpretation of the results is complex, with biases and uncertainties resulting from a combination of CALIOP and MODIS cloud sensitivity differences, systematic algorithm biases from MODIS and CALIOP, as well as uncertainties resulting from spatial sampling differences.

[35] As earlier discussed (section 2) either one or two CALIOP 5-km averaged CTH retrievals can fall within a single 5-km MODIS cloud top pressure retrieval. It is the averaged CALIOP CTH that is compared to the MODIS product. Even with an accurate collocation, CALIOP only samples a small fraction of the MODIS 5-km pixel array as shown in Figure 1a; introducing random uncertainty. To compare the MODIS CTP to the CALIOP cloud top height retrieval, the MODIS CTP is converted to CTH using a model profile. The difference between MODIS and CALIOP (MODIS - CALIOP) is calculated using the MODIS CTH and the mean of the collocated CALIOP CTH within the MODIS 5-km FOV.

[36] On the basis of this approach, CTH retrievals are collocated, and the CTH differences compared, for August 2006 and February 2007. The mean collocated CTH differences are presented in Table 4 with results separated by both CALIOP 1-km and 5-km layer averaging, high and low clouds, and global and nonpolar averages. For all nonpolar regions, the CTH differences are negative; suggesting that on average the CTH retrieved by MODIS is less than CALIOP. This negative difference is most pronounced for the CALIOP 5-km averaged cloud top heights which have the highest sensitivity to optically thin clouds. For high clouds (i.e., CTH > 5 km), the nonpolar mean CTH difference is −4.5 ± 4.6 km, a considerably larger absolute

Table 4. Cloud Top Height Global Statistics of the Mean Differences Between MODIS and CALIOP[a]

	August 2006 Mean ± STD (km)	February 2007 Mean ± STD (km)
Global 1 km (5 km)		
All clouds	−1.4 (−2.6) ± 2.9 (3.9)	−1.4(−2.6) ± 2.9(3.9)
High (>5 km)	−2.7 (−4.3) ± 2.9 (4.3)	−2.7 (−4.4) ± 3.5(4.4)
Low (<5 km)	−0.1 (−0.3) ± 1.3(1.3)	−0.3 (−0.4) ± 1.3(1.3)
Nonpolar (−60°–60° latitude)		
All Clouds	−1.5 (−2.8) ± 3.0(4.1)	−1.5(−2.8) ± 3.0(4.2)
High (>5 km)	−2.7 (−4.5) ± 3.7(4.6)	−2.7 (−4.5) ± 3.7(4.8)
Low (<5 km)	−0.3 (−0.4) ± 1.3(1.2)	−0.3 (−0.5) ± 1.3(1.3)
Arctic (>60° latitude)		
All Clouds	−0.7 (−1.7) ± 2.1(2.8)	−1.7 (−2.4) ± 2.7(3.0)
High (>4 km)	−1.5 (−2.8) ± 2.3(2.9)	−3.4 (−3.9) ± 2.4(2.6)
Low (<4 km)	0.3 (0.2) ± 1.2(1.2)	0.1(0.0) ± 1.7(1.7)
Northern midlatitude (25°–60° lat)		
All clouds	−1.3 (−2.4) ± 2.8(3.7)	−1.4 (−2.1) ± 2.4(2.8)
High (>5 km)	−2.2 (−3.7) ± 3.5 (4.1)	−2.3(−3.1) ± 2.7(3.1)
Low (<5 km)	−0.1 (−0.3) ± 1.4 (1.3)	−0.4(−0.6) ± 1.3(1.3)
Tropics (−25°–25° latitude)		
All clouds	−1.9 (−3.7) ± 3.6 (5.0)	−2.2(−4.1) ± 3.8(5.4)
High (>4 km)	−3.4 (−5.9) ± 4.4 (5.4)	−3.4(−6.2) ± 4.5(5.7)
Low (<5 km)	−0.4 (−0.6) ± 1.3(1.3)	−0.6(−0.8) ± 1.3(1.1)
Southern midlatitudes (−60°–−25° latitude)		
All clouds	−1.1 (−1.8) ± 2.2 (2.7)	−0.8(−1.6) ± 2.3(3.0)
High (>5 km)	−2.3 (−3.2) ± 2.6 (5.4)	−2.1(−3.3) ± 2.9(3.6)
Low (<5 km)	−0.3 (0.4) ± 1.1 (1.1)	0.0(−0.2) ± 1.3(1.2)
Antarctic < −60° latitude 1 km (5 km)		
All clouds	−1.9 (−3.2) ± 2.8(3.6)	−0.7 (−1.3) ± 1.7(2.2)
High (>4 km)	−3.1 (−4.4) ± 2.6(3.4)	−1.6 (−2.5) ± 1.9(2.3)
Low (<4 km)	0.5 (0.4) ± 1.4(1.4)	0.1 (0.0) ± 1.0(1.0)

[a]A mean less than zero occurs if the MODIS cloud top height is on average lower than CALIOP. The results are separated by month, global, and nonpolar with nonpolar including all regions except those above 60°N and below 60°S and polar regions. The results are also separated by 1-km and 5-km CALIOP cloud top heights with the 5-km differences within the parentheses.

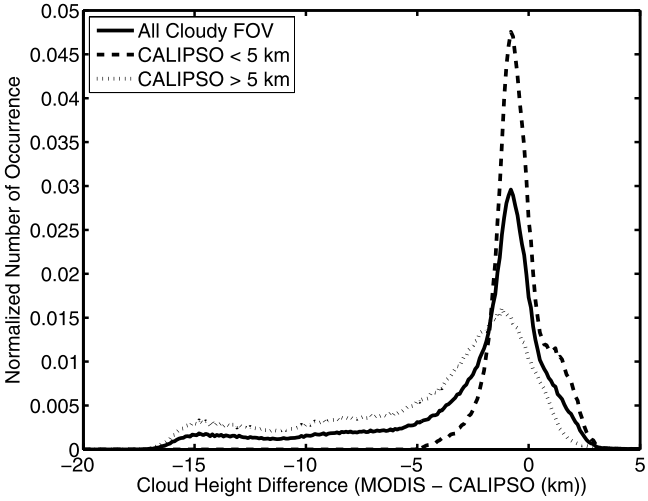

Figure 8. Normalized histogram of the global cloud height differences between MODIS and CALIOP for August 2006. The polar regions (60° latitude) have been excluded from the comparison. A negative difference occurs if the MODIS cloud top height is below CALIOP. The solid black distribution includes both high and low clouds. The red and blue distribution have been separated into high and low clouds, respectively. The distributions include over 2.4 million collocated comparisons.

difference than reported in previous aircraft studies [*Frey et al.*, 1999; *Holz et al.*, 2006]. The CTH difference changes significantly when comparing MODIS CTH to the 1-km averaged CALIOP CTH; a bias of −2.7 ± 3.7 km is found for August 2006, representing a change of more than 30%. For low clouds, (i.e., CTH < 5 km), the nonpolar mean global CTH differences are −0.4 ± 1.2 km, significantly smaller.

[37] To further investigate the global mean CTH differences, a histogram of the CTH differences is presented in Figure 8 between MODIS and the 5-km CALIOP products. The distribution encompassed by the solid black line includes all collocated nonpolar data where both CALIOP and MODIS retrieved a CTH. This distribution has a prominent peak just less than zero with a pronounced tail extending to beyond −15 km. There are a significant number of comparisons where MODIS retrieves a CTH higher than CALIOP in the distribution (a positive difference in the histogram).

[38] On the basis of the CALIOP CTH retrieval, the distribution was separated by low (<5 km) and high (>5 km) clouds as presented by the dashed distributions in Figure 8. The large negative differences are associated with high clouds. The pronounced positive "bump" at +1 km is associated with low-level clouds.

[39] Both the CALIOP and MODIS CTH retrievals are sensitive to the cloud optical properties and the local surface and atmospheric conditions. These characteristics have

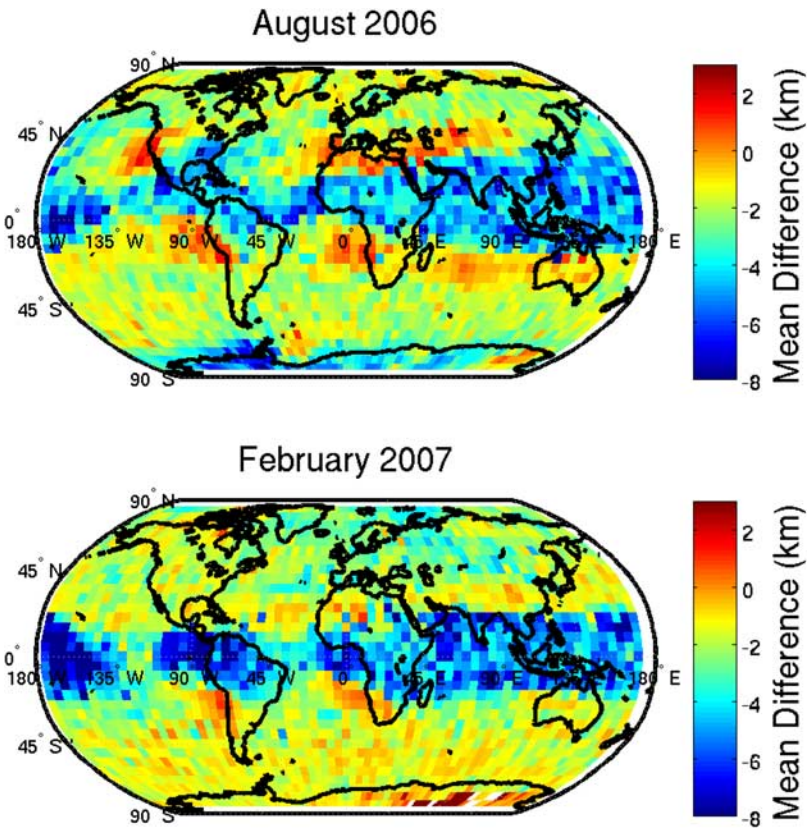

Figure 9. A 5-degree grid of the mean cloud top height differences are presented. For each 5-degree grid box the mean of all the collocated differences (MODIS – CALIOP) is calculated. A negative difference (blue) results when the mean MODIS cloud height is below the CALIOP, while the red values represent MODIS overestimating the cloud top height relative to CALIOP.

Table 5. Fractional Cloud Detection Agreement and Mean Cloud Top Height and Standard Deviation of the Differences Between MODIS and CALIOP for the Month of August 2006 for Clouds With Heights Greater than 5 km as Determined by CALIOP[a]

	All CALIOP Clouds CTH > 5 km X, Mean ± STD	CALIOP Attenuated CTH > 5 km X, Mean ± STD	CALIOP Not Attenuated CTH > 5km X, Mean ± STD
Nonpolar	0.90, −4.5 ± 4.7 km	1.00, −1.0 ± 1.6 km	0.88, −5.2 ± 4.7 km
Arctic	0.92, −2.8 ± 2.9 km	0.99, −0.3 ± 1.5 km	0.91, −3.4 ± 2.8 km
North midlatitudes	0.85, −3.7 ± 4.1 km	0.99, −0.7 ± 1.6.km	0.84, −4.3 ± 4.2 km
Tropics	0.88, −5.9 ± 5.4 km	1.00, −1.1 ± 1.8 km	0.87, −6.6 ± 5.4 km
South midlatitudes	0.97, −3.2 ± 3.1 km	1.00, −1.1 ± 1.5 km	0.96, −3.9 ± 3.2 km
Antarctica	0.72, −4.4 ± 3.4 km	0.95, −2.3 ± 2.5 km	0.70, −4.7 ± 3.4 km

[a]X denotes fractional cloud detection agreement. Results are separated by cases when CALIOP was and was not attenuated by the first cloud layer.

strong regional dependencies that are evident in our analysis of the monthly global data. Figure 9 presents the collocated mean CTH differences separated into 5° grid boxes for August 2006 and February 2007. Each grid cell presents the mean CTH differences for all the collocated MODIS/CALIOP data within the cell.

[40] Figure 9 reveals a significant geographical dependence in the CTH differences found in Figure 8. The large underestimation of the MODIS CTH for high clouds is strongly correlated with latitude, with mean CTH differences greater than 6 km near the Intertropical Convergence Zone (ITCZ) for August 2006. This region has a considerable amount of optically thin cirrus during the northern hemisphere summer. The region of negative CTH differences migrates slightly south during February 2007 with a more pronounced region of large negative differences found over northern South America and the Western Pacific. The mean cloud height differences for high tropical clouds is found to be −5.9 ± 5.4 km with the largest differences for nonopaque clouds with mean differences of −6.6 ± 5.4 km as presented in Table 5. The CTH agreement improves near Florida and the Caribbean in February, likely resulting from the decrease in convection during the winter months. Significant CTH differences are found in the polar regions, with MODIS significantly underestimating the CTH relative to CALIOP over much of the Antarctic during winter (August 2006). The magnitude of the polar disagreement lessens considerably in February due largely to a substantial increase in the MODIS overestimation of the CTH (Antarctic summer).

3.4. Comparison for Marine Low-Level Clouds

[41] The systematic MODIS CTH overestimation in Figure 9 is most pronounced off the North American Pacific coast, the west coast of South America and off the Eastern coast of Southern Africa. These three regions have a frequent occurrence of marine stratus and stratocumulus clouds. To investigate this bias, the MODIS CTH is compared to the CALIOP attenuated backscatter profiles with an example presented in Figure 10. For the regions with a high bias (>1 km), the mean MODIS CTH retrievals are approximately 1.5 km above the CALIOP-based CTH. The possible presence of thin cirrus above the lower water cloud layer could explain the MODIS overestimation; however, cirrus is notably absent in the CALIOP attenuated backscatter data. Further investigation of the MODIS CTP retrieval algorithm revealed that overestimation occurs in regions with low-level temperature inversions. In the Collection-5 operational retrieval approach, the 11-μm window Brightness Temperature (BT) is matched to that calculated using the GDAS temperature and water vapor profile. The algorithm searches the model profile from the troposphere to the surface (i.e., a top-down approach). The first match in brightness temperature provides the CTP. In the presence of a temperature inversion, there may be multiple solutions for the CTP. Marine stratus frequently occurs near the bottom of a

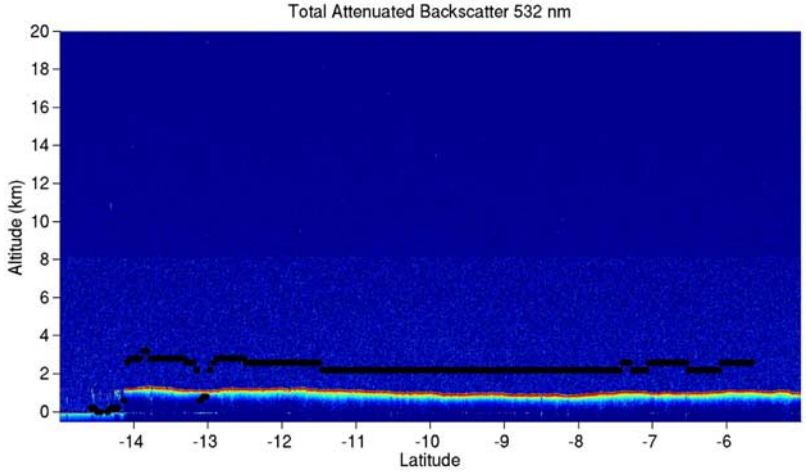

Figure 10. CALIOP attenuated backscatter profile of Marine stratus from 24 August 2006 off the coast of South America. The black dots are the collocated MODIS cloud height retrieval.

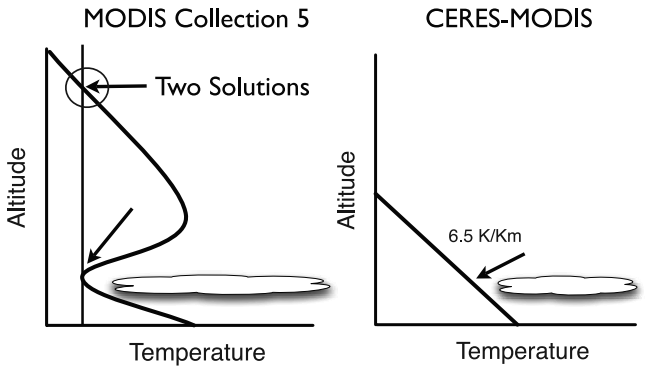

Figure 11. A graphical representation of the MODIS Collection-5 window BT retrieval over (left) marine stratus and (right) the CERES methodology. The Collection-5 retrieval typically selects the window BT intersection circled in the left panel.

temperature inversion as depicted in Figure 11. Because the current MODIS algorithm selects the temperature intersection at the top of the inversion, the CTP is underestimated.

[42] As part of the University of Wisconsin Product Evaluation and Test Element (PEATE), the MODIS Collection-5 cloud top height retrieval was modified to use the marine stratus retrieval algorithm given by [*Minnis et al.*, 1992], which assumes a constant lapse rate normalized to the GDAS ocean surface temperature. The MODIS Collection-5 algorithm was reprocessed with the modified retrieval and then reevaluated using CALIOP for August 2006 with the results presented in Figure 12. The revised MODIS CTH assignment for low clouds yields significantly improved comparisons with CALIOP with a mean difference of −0.2 km.

3.5. Comparisons for MODIS High-Level Clouds (CTH > 5 km)

[43] A surprisingly large negative bias was found in Figure 8 for high clouds (CTH > 5 km). A negative bias can be expected for optically thin but geometrically thick cirrus, because the CO_2 slicing retrieval is sensitive to the cloud radiative mean pressure. For the case of an optically thin but geometrically thick cloud, the inferred CTH is expected to fall below the lidar-retrieved CTH [*Holz et al.*, 2006; *Naud et al.*, 2005]. For single-layered ice clouds, the expected CTH differences can be as large 5 km. However, these CTH differences are still considerably smaller than the differences found for the global distribution in Figure 8.

[44] Globally, the largest differences occur immediately north and south of the equator as shown in Figure 9. This region has frequent high thin cirrus, often with complex multilayered cloud formations. Table 5 presents the August 2006 mean cloud height differences for high clouds greater than 5 km, separated by latitude region and attenuating and nonattenuating clouds as determined by the CALIOP opacity flag. For attenuating tropical high clouds, the mean cloud height difference between CALIOP and

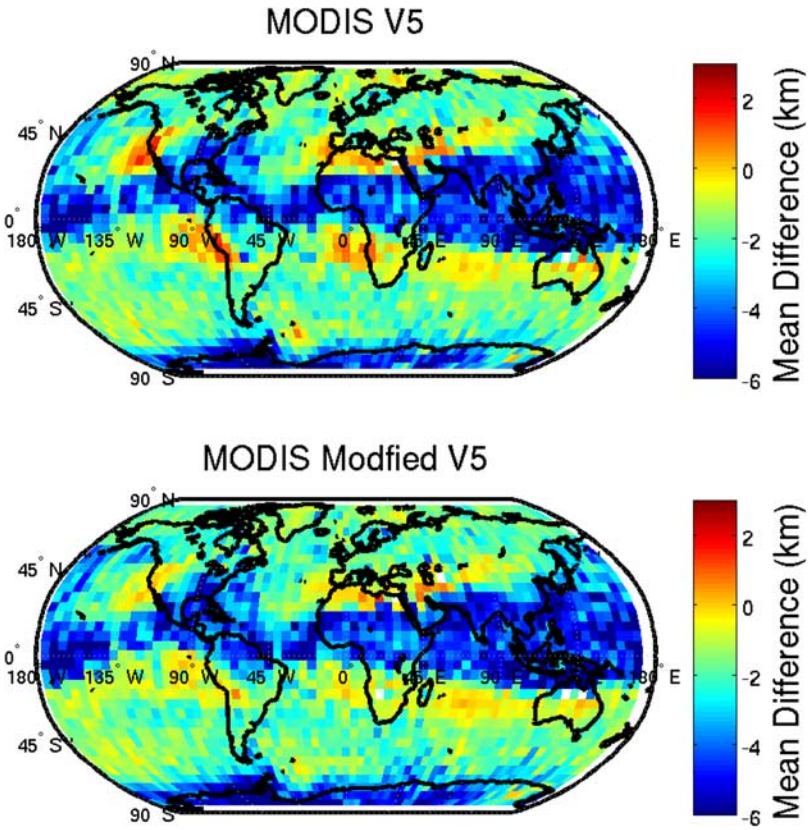

Figure 12. (top) The 5-degree grid of the mean differences between CALIOP and MODIS (MODIS – CALIOP) for the Collection-5 MODIS retrieval compared with (bottom) the modified marine stratus retrieval.

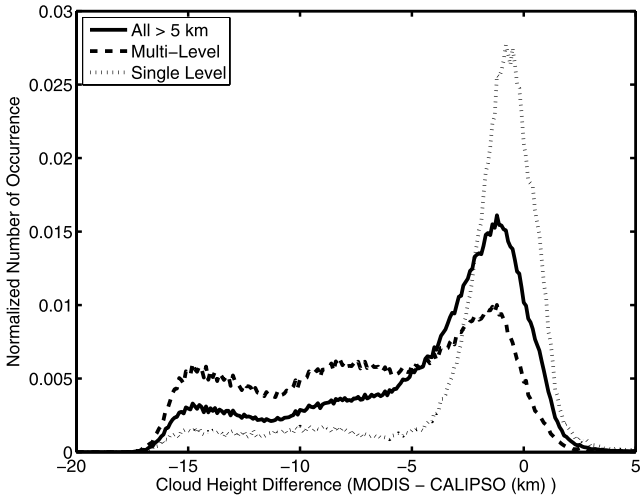

Figure 13. Histogram of global cloud height differences for August 2006 are presented filtered by single and multilayer clouds using CALIOP. A multilayer cloud is defined using CALIOP and requires that maximum cloud top height be greater than 5 km and the separation between the top cloud layer base and cloud top height of the bottom layer be greater than 4 km.

MODIS is approximately -1.1 ± 1.8 km in contrast to the nonattenuated cases with mean differences greater than -6.6 ± 5.4 km. Multilayered clouds can result in large cloud height underestimation when applying CO_2 slicing [*Baum and Wielicki*, 1994], providing possibly one explanation for the large negative bias for nonattenuating clouds. The impact of multilayered clouds on MODIS is investigated using the collocated CALIOP CTH retrievals. When the column optical thicknesses are less than approximately 3, CALIOP can accurately detect both base heights and top heights within multilayered cloud scenes. On the basis of the CALIOP 5-km layer product, the global data set was separated into both single-layered high clouds (CTH > 5 km) and multilayered clouds, with multilayered clouds being defined as having more than one cloud layer in a vertical column with at least one layer separated from another by more than 4 km from the nearest neighbor. Figure 13 presents the histogram for August 2006 for cloud height differences separated by single and multilevel clouds. When interpreting the results, it is important to consider CALIOP's sensitivity to multilayered clouds and the optical thickness limit. CALIOP is sensitive to a lower layer only if the signal is not totally attenuated by the upper layer(s). Because the MODIS sensitivity to multilayered clouds is also reduced as the optical thickness of the uppermost cloud layer increases, it is expected that the CALIOP multilayered cloud filter should be representative of the MODIS sensitivity. In Figure 13 the multilayered cloud histogram displays a significantly larger CTH bias then the single layer histogram indicating that multilayered clouds have a considerable impact on the MODIS CTH biases. However, even with the multilayered cases removed, the single-layered cloud histogram still has a considerable number of cases that show a large negative bias.

[45] Multilayered clouds do not fully explain the negative CTH biases found in Figure 8. The MODIS algorithm retrieval estimates the CTP/CTH using one of two methods. If the CO_2 slicing algorithm does not converge to an acceptable solution, the retrieval reverts to a water vapor corrected 11-μm window BT retrieval. If MODIS reverts to the window BT retrieval for cases with optically thin cirrus, a significant cloud top height underestimation can be expected [*Baum et al.*, 2003]. A limited comparison with ground-based measurements found that MODIS often reverts to an 11-um window retrieval for very thin cirrus resulting in significant biases [*Naud et al.*, 2004]. To investigate this impact, the collocated data set was separated on the basis of the MODIS retrieval method with results presented in Figure 14. For scenes when MODIS successfully applies CO_2 slicing, the distribution becomes considerably narrower, almost eliminating the very large negative CTH biases found in the distribution containing all MODIS CTH retrievals (window BT and CO_2 slicing). The mean bias compared to the CALIOP 5 km layer products for CO_2 slicing during August 2006 was -2.4 ± 2.8 km. For scenes determined by CALIOP to include single-layer clouds, the MODIS CO_2 slicing histogram is narrower than both the combined and CO_2-slicing-only results with a mean bias of -1.0 ± 1.8 and agrees with the expected biases resulting from the physical sensitivity differences between a passive IR-based and active sensor CTH retrieval [*Holz et al.*, 2006]. The accuracy of the MODIS CO_2 slicing retrieval can be perturbed by several external factors, including instrument noise, radiometric biases, and uncertainties in the calculated clear sky radiances. The ability of MODIS to retrieve an accurate cloud top height using CO_2 slicing thus depends on a combination of the uncertainties inherent in the retrieval process and the magnitude of the cloud signal present in the measured radiances. The cloud signal magnitude in turn depends primarily on the cloud top height and the cloud optical thickness. However, because estimates of cloud optical thickness are not presently available in the

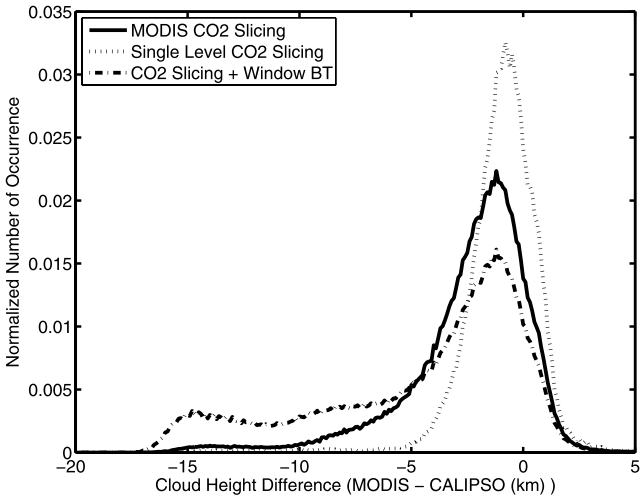

Figure 14. Histogram of the global cloud height differences during August 2006 for CALIOP determined high clouds (>5 km) filtered for cases where the MODIS retrieval applied CO_2 slicing (solid line) and CALIOP determined single level clouds (dotted line). The distribution for all high clouds (combined CO_2 slicing + window BT retrieval) is also presented.

CALIOP data stream, it is not possible to quantify the optical thickness limitations in the MODIS retrievals that contribute to the large negative biases. However, the results suggest that the MODIS CTH retrieval could be improved by applying CO_2 more often instead of the window BT retrieval for the thin cirrus. This remains an active area of investigation.

4. Conclusions

[46] This paper compares CALIOP and MODIS Collection 5 cloud detection and cloud top height (CTH) assignments. To facilitate the comparison an accurate collocation algorithm was developed. The comparison is conducted globally for the months of August 2006 and February 2007.

[47] For cloud detection, the two approaches (CALIOP and MODIS) agree on a scene being clear or cloudy over 75% of the time excluding the polar regions. However, the agreement is dependent on the methodology used in the comparison, including the collocation process and the CALIOP averaging approach. The agreement is generally better for cloudy scenes than clear. At regional scales, cloud detection differences can be significant, with the largest disagreements found in the polar and desert regions. Over deserts the disagreement results from MODIS missing high thin cirrus but also CALIOP incorrectly identifying thick aerosol layers as cloud. A small diurnal detection dependence is found, with, on average, 2–3% better agreement occurring for daytime measurements. Significant disagreement found in the Arctic and Antarctic regions, including the southern ocean near the sea ice boundary that is attributed to the highly variable surface emissivity of broken ice and the lack of contrast between the surface and clouds. Disagreement during the Antarctic winter can be partially attributed to polar stratospheric clouds that are detected by CALIOP but not MODIS.

[48] For CTH retrievals, the comparison reveals disagreements with a strong regional and cloud type dependence. A systematic high CTH bias of 1–2 km is found in the MODIS results for both August 2006 and February 2007 in oceanic regions with high frequencies of occurrence of stratocumulus. The cause of the bias is traced to the window BT cloud height retrieval in the MODIS Collection 5 algorithm, and is attributed to the approach used to infer CTH when low-level temperature inversions exist. The temperature profile near the surface was modified to a constant lapse rate, the MODIS data subsequently reprocessed, with results again compared to CALIOP for August 2006. The CTH bias was mitigated using the modified cloud retrieval approach. This correction will be implemented into the next version of the MODIS cloud software.

[49] For optically thin, but geometrically thick high clouds (CTH > 5 km), MODIS underestimates the CTH relative to CALIOP. When compared to the CALIOP 1-km averaged products, the nonpolar mean CTH difference between CALIOP and MODIS was found to be approximately 3 km for both August 2006 and February 2007. The 5-km CALIOP CTH products have mean differences with MODIS that are greater than 4 km. The larger bias for the CALIOP 5-km averages results from the sensor's increased sensitivity to optically thin cirrus. For cases when the first cloud layer did not attenuate CALIOP, the mean difference for high clouds for August 2006 was −6.6 km. The large CTH differences were investigated, with the largest differences found for high thin cirrus in the equatorial region with differences greater than 15 km. For these cases it was found that the MODIS reverted to a water vapor corrected window brightness temperature retrieval instead of using CO_2 slicing. When the differences were filtered to only include CO_2 slicing retrievals, the agreement improved significantly, with the best agreement when CO_2 slicing was applied to single layered clouds with a mean difference of -1.0 ± 1.9 km.

Appendix A

[50] A detailed description of the method developed to collocate MODIS with CALIOP is presented. The algorithm is designed to be computationally efficient and accurate allowing for rapid identification of the coincident CALIOP and MODIS observations. Before proceeding to describe the details of the collocation algorithm we need to first define the coordinate systems in use. No explanation needs to be given of latitude and longitude, except to point out that latitudes must be distinguished as either geodetic or geocentric, and that failure to do so leads to errors that vitiate any results. Neglecting this distinction can lead to a maximum error of about 21 km. The celestial coordinate system, which some may refer to as inertial, has its origin at the center of the Earth, its x axis in the equatorial plane directed toward the Vernal Equinox, its y axis 90 degrees to the east of the Vernal Equinox, and the z axis through the North Pole. This basis is fixed to the heavens, and points of the Earth change their celestial coordinates continually as the Earth rotates. The terrestrial coordinate system is fixed to the rotating Earth, with the x axis in the plane of the equator directed toward the Greenwich meridian, and y axis 90 degrees to the east, and the z axis again through the North Pole. Knowledge of the longitude of the Vernal Equinox as a function of time allows easy conversion between celestial and terrestrial frames. Simple trigonometry allows conversion between geocentric latitude/longitude and the terrestrial frame. Conversions between geodetic and geocentric latitude can use the relation

$$b^2 \tan D = \tan C,$$

where $b^2 = 0.99327730$, and where D and C are geodetic and geocentric latitude, respectively.

[51] Suppose that we are given a single MODIS scan line containing 1354 points, the Earth locations of which are provided. We seek to know which of a large number of CALIOP GIFOV intersect this MODIS scan line. We suppose further that these MODIS locations are in the form of geodetic latitude, longitude, and a corresponding time. Our task is to determine which of the 1354 FOVs on this scan line coincide with which of the roughly 65000 FOVs in the CALIOP data set, a total of about 9×107 possible overlaps to be checked. A tedious computer search to ascertain these overlaps is undesirable, whereas the collocation algorithm allows us to restrict the point-by-point search to a mere handful of MODIS and CALIOP observations. At a bare minimum, before undertaking any search, one would at least wish to ascertain that the MODIS scan

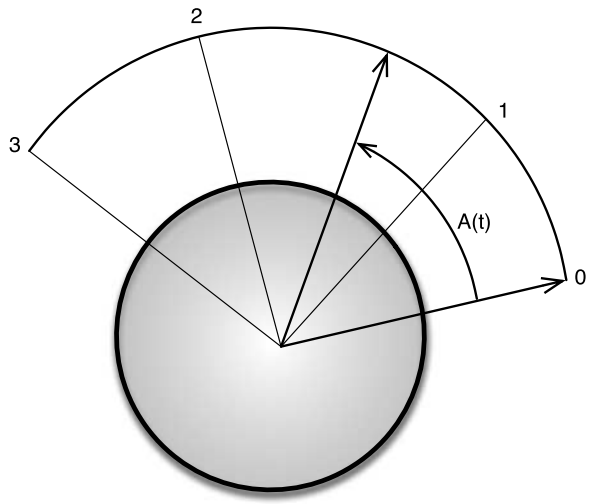

Figure A1. Knowledge of a satellite's angular displacement at four points along an orbital segment allows us to express its instantaneous displacement as a cubic polynomial. Being differentiable, the polynomial can be numerically inverted to find the time of a given displacement.

line and the CALIOP traces even intersect. In the following, we shall disregard terrain elevation, with the understanding that its consideration is not a major complication.

[52] The given MODIS scan line does not describe a great circle across the face of the Earth. The satellite moves and the Earth rotates during the time required to make the scan (less than 0.5 s). Moreover, the satellite when looking at nadir may not be looking directly toward the center of the Earth, but rather looking normal to the Earth's underlying surface. But because the satellite's motion during the scan is on the order of 3 kilometers, and the movement of a point of the Earth is at most 0.231 km during the scan, we make the slightly inaccurate assumption that the MODIS scan across the Earth is a great circle in the terrestrial system described by the vector cross product

$$\mathbf{M} = \mathbf{A} \times \mathbf{B},$$

where **A** and **B** are the initial and final MODIS scan position vectors, with the center of the Earth as origin, and **M** is the vector quasi-plane of the scan. Since MODIS scans from right to left, the vector **M** is oriented backward along the MODIS subsatellite track.

[53] Consider next the trace of the CALIOP nadir-viewing instrument across the Earth. Both CALIPSO and AQUA are sun-synchronous satellites. The right ascension of there ascending nodes precess about 360 degrees in 365 days, or about 0.07 degrees per orbit. Hence over a fraction of an orbit, we can consider the satellite's motion to lie in a quasi-plane in the celestial coordinate system, which simplifies the task of estimating its motion in the absence of its orbital parameters. The Earth-located points which lie along the CALIOP path have a time associated with each, and can hence be converted to celestial coordinates. Two cubic polynomials with time as the independent variable, computed from four points chosen at roughly equal intervals along the CALIOP path, enable us to estimate both the angular displacement of the CALIOP satellite from the first CALIOP point, and the satellite's radius vector from the center of the Earth, in the celestial frame. For instance, we can compute the coefficients of a cubic polynomial which expresses the satellite's arc distance A from some initial position vector (e.g., the first CALIOP position) within the quasi-plane of the satellite's orbit, and within a limited time span (e.g., 25 min), as a function of time

$$A(t) = C_0 + C_1 t + C_2 t^2 + C_3 t^4,$$

where A(t) is the angular displacement from an initial time.

[54] *Froberg* [1965] has suggested a simple means of computing such polynomials. The four times needed to compute these coefficients are normally provided with the MODIS and CALIOP data sets, and the four needed values of arc distance are likewise inferred from the Earth-located CALIOP data (see Figure A1). A polynomial is differentiable and therefore the above can be inverted to obtain t, given arc length, by a Newton-Raphson successive approximation

$$t_1 = t_0 - A(t)/A'(t),$$

where the iteration continues until some threshold is reached. (A Newton-Raphson technique is valid for finding real roots of a polynomial A(t) provided the polynomial does not have a repeated root within the region of interest which would cause its derivative $A'(t)$ to vanish at that root.) We now have a scheme for inverse navigation; that is, the ability to compute the time when a satellite (e.g., CALIOP) will be over or abeam of a given point (e.g., a MODIS FOV) on the Earth, and hence we know approximately the CALIOP observation closest to the given MODIS FOV. Somewhat less importantly, a similar polynomial can be used to express the scalar radius vector of a satellite within the same time interval.

[55] These two polynomials can serve for inverse navigation, allowing us to estimate the time when CALIOP is over a given point on the Earth surface. Finally, these polynomials can be differentiated to obtain satellite velocity. We might add that it is by no means necessary to use polynomials as a simple navigation model. One could, for instance, create a table of satellite positions directly from the data files, separated by small time intervals, and interpolate directly into these tables. Polynomials, however, by being easily differentiable, provide a simple means of both forward and inverse navigation, and for estimating velocity.

[56] The subsatellite track created by CALIOP points is certainly not a great circle when plotted on the Earth, but this path is nearly a great circle in celestial space. The path of the satellite over the ground is the projection of its path through space, adjusted to correct for the satellite's apparent westward movement by virtue of the Earth's eastward rotation. If we choose an arbitrary CALIOP FOV from the given CALIOP set as a first guess for the one overlapping the given MODIS scan, then the satellite's apparent velocity with respect to the Earth at that FOV is its velocity through space, obtained by differentiating our polynomials for satellite position, adjusted by the eastward movement of the underlying Earth, i.e.,

$$\mathbf{V}_t = \mathbf{V}_s - E\cos(L)\mathbf{U}_e,$$

where the vector $\mathbf{V_t}$ is terrestrial satellite velocity, $\mathbf{V_s}$ is the velocity through space diminished by the ratio of Earth radius to satellite radius vector, and $\mathbf{U_e}$ is a unit vector pointing toward local east at the given FOV. The scalar E is the eastward speed of the Earth's rotation at the equator. The vector osculating plane of the satellite's movement in terrestrial space is given by

$$\mathbf{P} = \mathbf{R} \times \mathbf{V}_t,$$

where $\mathbf{R}$ is the terrestrial position vector of the chosen FOV. This osculating plane contains the CALIOP's instantaneous velocity vector in the terrestrial frame at the chosen FOV with respect to the underlying Earth. The cross product of the two terrestrial vectors $\mathbf{P}$ and $\mathbf{M}$ points approximately to the intersection on the Earth's surface of these two planes, which is roughly the point at which the CALIOP trace intersects the given MODIS scan line. The initially chosen CALIOP FOV may be far removed from this intersection, and hence the CALIOP/MODIS intersection may be erroneous. However, we can inverse-navigate the CALIPSO satellite to find the time when it is over this conjectural intersection, and we now have a more accurate estimate of the CALIOP FOV closest to the MODIS scan. We can hence iterate the procedure, thus obtaining a more accurate fix on the MODIS/CALIPSO intersection, etc., until some criterion is satisfied. At length we need only search for a few MODIS and a few CALIOP FOVs to find the ones that precisely overlap.

[57] Further iterations of this scheme for subsequent MODIS scan lines are more rapid since we already have an excellent first guess for the CALIOP point which overlies the next MODIS scan line.

[58] The question of ascertaining whether a CALIOP FOV actually overlies a given MODIS FOV may be viewed as follows: The CALIOP is a nadir-viewing instrument, but the MODIS scanner may view a particular MODIS FOV at an angle which departs significantly from nadir. In such a case the MODIS FOV, projected onto the ground, is quasi-elliptical rather than circular. Let us deal first with this case.

[59] If r is the nominal radius of the MODIS FOV at nadir, then the semiminor axis of an elliptical FOV is

$$m = rs/h,$$

where s is the slant range from satellite to the FOV, and h is the altitude of the MODIS-carrying spacecraft. We define the unit vector $\mathbf{j}$ as the cross product

$$\mathbf{j} = U(\mathbf{R} \times \mathbf{S}),$$

where $\mathbf{R}$ is the position vector of the MODIS FOV, and $\mathbf{S}$ is the slant range vector from the MODIS FOV to the AQUA satellite. The operator U is a normalizing operator that reduces its vector argument to unit length. The vector semiminor axis is thus m$\mathbf{j}$. The semimajor axis of the FOV lies along the unit vector $\mathbf{i}$ and is given by

$$\mathbf{i} = U(\mathbf{j} \times \mathbf{S}),$$

and the vector semimajor axis is $\mathbf{M}$ = m sec(A)$\mathbf{i}$; that is, it has the length of the semiminor axis elongated by the secant of the azimuth angle A. If $\mathbf{C}$ is the vector position of a CALIOP observation, then the x and y coordinates of a CALIOP point relative to the center of the elliptical MODIS FOV are the dot products

$$x = (\mathbf{C} - \mathbf{R})^* \mathbf{i}$$

$$y = (\mathbf{C} - \mathbf{R})^* \mathbf{j}.$$

The radial distance r^2 is given by the Pythagorean theorem $r^2 = x^2 + y^2$. If r^2 is less than m^2, the semiminor axis, then the CALIOP observation lies within the MODIS oval. If it is greater than M^2, the semimajor axis, it lies outside. In the intermediate case, if

$$y^2 < m^2\left(1 - x^2/M^2\right),$$

it lies inside, and in this event we assign to the CALIOP observation a weight

$$w = 1 - \left(x^2 + y^2\right)/\left(x^2 + m^2\left(1 - x^2/M^2\right)\right).$$

This weight is one if x, y = 0, i.e., the CALIOP point lies at the dead center of the MODIS FOV, and the weight is zero if it lies at the periphery of the MODIS FOV.

[60] It may happen that the MODIS FOV lies at or near the nadir of the AQUA, in which case we simply treat the MODIS FOV as if it were a circle with nominal nadir radius.

[61] **Acknowledgments.** We would like to acknowledge the NASA atmospheric Product Evaluation and Test Element for supporting this research. We would like to thank Liam Gumley, Scott Mindock, and Paul Menzel for their support. This research was funded under NASA grants NNG04HZ38C, NAS1–99106, and NNX07AR95G; NNG05GN47A also contributed to this study. We would also like to thank the MODIS and CALIPSO teams for supplying the data used in for this research.

References

Abshire, J., X. Sun, H. Riris, J. M. Sirota, J. F. McGarry, S. Palm, D. Yi, and P. Liiva (2005), Geoscience Laser Altimeter System (GLAS) on the ICESat mission: On-orbit measurement performance, *Geophys. Res. Lett.*, *32*, L21S02, doi:10.1029/2005GL024028.

Ackerman, S. A., K. I. Stabala, W. P. Menzel, R. A. Frey, C. Moeller, and L. E. Gumley (1998), Discriminating clear sky from clouds with MODIS, *J. Geophys. Res.*, *103*, 32,141–32,157, doi:10.1029/1998JD200032.

Ackerman, S. A., R. E. Holz, R. Frey, E. W. Eloranta, B. Maddux, and M. J. McGill (2008), Cloud detection with MODIS: Part II. Validation, *J. Atmos. Oceanic Technol.*, *25*, 1073–1086.

Baum, B. A., and B. Wielicki (1994), Cirrus cloud retrieval using infrared sounding data: Multilevel cloud errors, *J. Appl. Meteorol.*, *33*, 107–117, doi:10.1175/1520-0450(1994)033<0107:CCRUIS>2.0.CO;2.

Baum, B. A., R. A. Frey, G. G. Mace, M. K. Harkey, and P. Yang (2003), Nighttime multilayered cloud detection using MODIS and ARM data, *J. Appl. Meteorol.*, *42*, 905–919, doi:10.1175/1520-0450(2003)042<0905:NMCDUM>2.0.CO;2.

Frey, R. A., B. A. Baum, W. P. Menzel, S. A. Ackerman, C. C. Moeller, and J. D. Spinhirne (1999), A comparison of cloud top heights computed from airborne lidar and MAS radiance data using CO_2 slicing, *J. Geophys. Res.*, *104*, 24,547–24,555, doi:10.1029/1999JD900796.

Frey, R., S. A. Ackerman, Y. Liu, K. I. Strabala, H. Zhang, J. Key, and X. Wang (2008), Cloud detection with MODIS: Part I. Improvements in the MODIS Cloud Mask for Collection 5, *J. Atmos. Oceanic Technol.*, *25*, 1057–1072.

Froberg, C. E. (1965), *Introduction to Numerical Analysis*, Addison-Wesley, New York.

Hawkinson, J. A., W. Feltz, and S. A. Ackerman (2005), A comparison of GOES sounder- and cloud lidar- and radar-retrieved cloud-top heights, *J. Appl. Meteorol.*, *44*, 1234–1242, doi:10.1175/JAM2269.1.

Heidinger, A. K. (2003), Rapid day-time estimation of cloud properties over a large area from radiance distributions, *J. Atmos. Oceanic Technol.*, *20*, 1237–1250, doi:10.1175/1520-0426(2003)020<1237:RDEOCP>2.0.CO;2.

Holz, R. E., S. Ackerman, P. Antonelli, F. Nagle, R. O. Knuteson, M. McGill, D. L. Hlavka, and W. D. Hart (2006), An improvement to the high-spectral-resolution CO_2-slicing cloud-top altitude retrieval, *J. Atmos. Oceanic Technol.*, *23*, 653–670, doi:10.1175/JTECH1877.1.

Kahn, B. H., A. Eldering, A. J. Braverman, E. J. Fetzer, J. H. Jiang, E. Fishbein, and D. L. Wu (2007a), Towards the characterization of upper tropospheric clouds using Atmospheric Infrared Sounder and Microwave Limb Sounder observations, *J. Geophys. Res.*, *112*, D05202, doi:10.1029/2006JD007336.

Kahn, B. H., et al. (2007b), Cloud-type comparison of AIRS, CloudSat, and CALIPSO cloud height and amount, *Atmos. Chem. Phys. Discuss.*, *7*, 13,915–13,958.

King, M. D., W. P. Menzel, Y. J. Kaufman, D. Tanre, B. C. Gao, S. Platnick, S. A. Ackerman, L. A. Remer, R. Pincus, and P. A. Hubanks (2003), Cloud and aerosol properties, precipitable water, and profiles of temperature and humidity from MODIS, *IEEE Trans. Geosci. Remote Sens.*, *41*, 442–458, doi:10.1109/TGRS.2002.808226.

Liu, Z., M. A. Vaughan, D. M. Winker, C. A. Hostetler, L. R. Poole, D. L. Hlavka, W. Hart, and M. McGill (2004), Use of probability distribution functions for discriminating between cloud and aerosol in lidar backscatter data, *J. Geophys. Res.*, *109*, D15202, doi:10.1029/2004JD004732.

Mahesh, A., M. A. Gray, S. Palm, W. Hart, and J. D. Spinehirne (2004), Passive and active detection of clouds: Comparisons between MODIS and GLAS observations, *Geophys. Res. Lett.*, *31*, L04108, doi:10.1029/2003GL018859.

Menzel, W. P., F. Richard, H. Zhang, D. P. Wylie, C. Moeller, R. E. Holz, B. Maddux, K. I. Strabala, and L. E. Gumley (2008), MODIS global cloud-top pressure and amount estimation: Algorithm description and results, *J. Appl. Meteorol. Climatol.*, *47*, 1175–1198, doi:10.1175/2007JAMC1705.1.

Min, Q., P. J. Minnett, and M. M. Khaiyer (2004), Comparison of cirrus optical depths derived from GOES 8 and surface measurements, *J. Geophys. Res.*, *109*, D15207, doi:10.1029/2003JD004390.

Minnis, P., P. W. Heck, D. F. Young, C. W. Fairall, and J. Snider (1992), Simultaneous satellite and island-based instrumentation during FIRE, *J. Appl. Meteorol.*, *31*, 317–339, doi:10.1175/1520-0450(1992)031<0317:SCPDFS>2.0.CO;2.

Naud, C., J. Muller, M. Haeffelin, Y. Morille, and A. Delaval (2004), Assessment of MISR and MODIS cloud top heights through inter-comparison with a back-scattering lidar at SIRTA, *Geophys. Res. Lett.*, *31*, L04114, doi:10.1029/2003GL018976.

Naud, C., J. Muller, and P. de Valk (2005), On the use of ICESAT-GLAS measurements for MODIS and SEVIRI cloud-top height accuracy assessment, *Geophys. Res. Lett.*, *32*, L19815, doi:10.1029/2005GL023275.

Platnick, S., M. D. King, S. A. Ackerman, W. P. Menzel, B. A. Baum, J. C. Riedi, and R. A. Frey (2003), The MODIS cloud products: Algorithms and examples from Terra, *IEEE Trans. Geosci. Remote Sens.*, *41*, 459–473.

Reagan, J. A., X. Wang, and M. T. Osborne (2002), Spaceborne lidar calibration from cirrus and molecular backscatter returns, *IEEE Trans. Geosci. Remote Sens.*, *40*, 2285–2290, doi:10.1109/TGRS.2002.802464.

Rossow, W. B., and R. A. Schiffer (1999), Advances in understanding clouds from ISCCP, *Bull. Am. Meteorol. Soc.*, *80*, 2261–2287, doi:10.1175/1520-0477(1999)080<2261:AIUCFI>2.0.CO;2.

Smith, W. L., and C. M. R. Platt (1978), Comparison of satellite-deduced cloud heights with indications from radiosonde and ground-based laser measurements, *J. Appl. Meteorol.*, *17*, 1796–1802, doi:10.1175/1520-0450(1978)017<1796:COSDCH>2.0.CO;2.

Stephens, G. L., et al. (2002), The CloudSat mission and the A-Train: A new dimension of space-based observations of clouds and precipitation, *Bull. Am. Meteorol. Soc.*, *83*, 1771–1790, doi:10.1175/BAMS-83-12-1771.

Thomas, A., et al. (2002), In situ measurements of background aerosol and subvisible cirrus in the tropical tropopause region, *J. Geophys. Res.*, *107*(D24), 4763, doi:10.1029/2001JD001385.

Vaughan, M. A., S. A. Young, D. M. Winker, K. Powell, A. Omar, Z. Liu, Y. X. Hu, and C. Hostetler (2004), Fully automated analysis of space-based lidar data: An overview of the CALIPSO retrieval algorithms and data products, *Proc. SPIE Int. Soc. Opt. Eng.*, *5575*, 16–30, doi:10.1117/12.572024.

Wielicki, B. A., and J. A. Coakley (1981), Cloud retrieval using infrared sounder data: Error analysis, *J. Appl. Meteorol.*, *20*, 157–169, doi:10.1175/1520-0450(1981)020<0157:CRUISD>2.0.CO;2.

Winker, D. M., W. H. Hunt, and C. A. Hostetler (2004), Status and performance of the CALIOP lidar, *Proc. SPIE Int. Soc. Opt. Eng.*, *5575*, 8–15.

Winker, D. M., W. H. Hunt, and M. J. McGill (2007), Initial performance assessment of CALIOP, *Geophys. Res. Lett.*, *34*, L19803, doi:10.1029/2007GL030135.

Wylie, D. P., and W. P. Menzel (1999), Eight years of high cloud statistics using HIRS, *J. Clim.*, *12*, 170–184.

Wylie, D., E. Eloranta, J. D. Spinhirne, and S. P. Palm (2007), A comparison of cloud cover statistics from the GLAS lidar with HIRS, *J. Clim.*, *20*, 4968–4981, doi:10.1175/JCLI4269.1.

Zhao, G., and L. D. Girolamo (2006), Cloud fraction errors for trade wind cumuli from EOS-Terra instruments, *Geophys. Res. Lett.*, *33*, L20802, doi:10.1029/2006GL027088.

S. A. Ackerman, B. Baum, S. Dutcher, R. Frey, R. E. Holz, and F. W. Nagle, Cooperative Institute for Meteorological Satellite Studies, University of Wisconsin-Madison, 1225 West Dayton Street, Madison, WI 53706, USA. (reholz@ssec.wisc.edu)

R. E. Kuehn and M. A. Vaughan, Science Systems and Applications, Inc., MS 475, Hampton, VA 23681, USA.

Cloud Detection with MODIS: Part II Validation

S. A. Ackerman[1], R. E. Holz[1], R. Frey[1], E. W. Eloranta[2],

B. Maddux[1], and M. McGill[3]

[1]Cooperative Institute for Meteorological Satellite Studies (CIMSS)

[2]Space Science and Engineering Center

University of Wisconsin, Madison, WI

[3]NASA Goddard Space Flight Center

Greenbelt MD 20771

Submitted to Journal of Atmospheric and Oceanic Technology

August 2007, revised December 2007

* Corresponding author address:

Steven A. Ackerman

CIMSS

University of Wisconsin-Madison

1225 W. Dayton St.

Madison, WI 53706

e-mail: stevea@ssec.wisc.edu

ABSTRACT

An assessment of the performance of the MODIS cloud mask algorithm for Terra and Aqua satellites is presented. The MODIS cloud mask algorithm output is compared with lidar observations from ground (Arctic High Spectral Resolution Lidar; AHSRL), aircraft (Cloud Physics Lidar; CPL) and satellite borne (GLAS). The comparison with 3-years of coincident observations of MODIS and combined radar and lidar cloud product from the Department of Energy (DOE) Atmospheric Radiation Measurement (ARM) program Southern Great Plains (SGP) site in Lamont, Oklahoma, indicates that the MODIS algorithm agrees with the lidar about 85% of the time. A comparison with the CPL and AHSRL, indicates that the optical depth limitation of the MODIS cloud mask is approximately 0.4. While MODIS algorithm flags scenes with cloud optical depth of 0.4 as cloudy, approximately 90% of the mis-labeled scenes have optical depths less than 0.4. A comparison with the GLAS cloud data set indicates that cloud detection in polar regions at night remains challenging with the passive infrared imager approach.

In anticipation of comparisons with other satellite instruments, the sensitivity of the cloud mask algorithm to instrument characteristics (e.g. instantaneous field of view and viewing geometry) and thresholds are demonstrated. As expected, cloud amount generally increases with scan angle and IFOV. Nadir sampling represents zonal monthly mean cloud amounts but can have large differences for regional studies when compared to full swath width analysis.

Introduction

What is a cloud? According to the American Meteorological Society Glossary, a cloud is "a visible aggregate of minute water droplets and/or ice particles in the atmosphere above the earth's surface". From the perspective of remote sensing, the application and the instrument determine the answer. What is considered a cloud in one application may be defined as clear in another. For example, detection of thin cirrus clouds is important for infrared remote sensing of sea surface temperature and climate, but of little concern for microwave remote sounding of atmospheric temperature. This paper focuses on clear vs. cloudy sky discrimination using passive reflected solar and infrared observations from the NASA EOS Terra and Aqua polar orbiting satellites, in particular, the Moderate Resolution Imaging Spectroradiometer (MODIS) (Barnes, et al., 1998). Developed in collaboration with members of the MODIS science team, the MODIS cloud screening approach includes new approaches while still incorporating many previously existing techniques to detect obstructed fields of view (Ackerman et al., 1998).

Part I of this paper summarized the recent improvements to the cloud mask detection algorithm. Part II provides an assessment of cloud detection capability of the MODIS cloud mask algorithm in MODIS instantaneous fields-of-view (IFOV) (Ackerman et al 1998). The assessment is primarily made through comparisons of MODIS results with observations from active sensors. Measurements from passive imaging satellite systems provide a long time series of global observations; however, understanding the constraints in cloud detection from these measurements is required to assure proper interpretation of existing and future cloud data sets. In this context, we make use of MODIS observations to investigate the sensitivity of cloud detection to the various spatial and spectral constraints of the instrument. Thresholds are chosen to discriminate between clouds and clear sky but may vary according to view angle, surface type, time of year or solar zenith angle. We demonstrate the sensitivity of cloud detection to various thresholds and the

impacts on derived global cloud amount. We also consider the impacts of IFOV and sampling strategies on derived cloud amount. Some comparisons to existing satellite cloud data sets are presented here, but a separate paper will provide detailed comparisons of MODIS cloud products with those derived from other satellites. Finally, this paper does not assess the detection capability for all scenes types. For example, in the comparison with the land-based active sensors sun-glint does not become an issue as noted in the study of Zhao and Di Girolamo (2006).

Global view of MODIS cloud amount

Figure 1 shows the global distribution of cloud amount derived from MODIS from both Terra and Aqua satellites. As expected, the large-scale patterns are similar to other satellite data sets of cloud amount (Rossow, et al., 1993; Thomas, et al., 2004; Wylie, et al., 1994). The Inter-tropical convergence zone (ITCZ) is clearly evident as are the subtropical high-pressure systems and the marine stratocumulus regions. While there are differences in the performance between the two instruments, the algorithms are essentially the same. Therefore the differences result from either instrument performance or diurnal variations in cloud amount. Globally, results between the two satellites are offset by about 2% with Terra greater then Aqua in the long term mean.

Figure 2 shows the differences between MODIS Aqua and Terra monthly mean daytime cloud fractions for August 2002 through July 2007. These plots show Aqua minus Terra, (i.e., 1:30 pm minus 10:30 am local time) values. Whether the differences in cloud amounts are due to threshold differences, calibration differences, instrument differences, or are real are difficult to completely assess. The Aqua $R_{0.86}$ ocean cloud thresholds are higher than those of Terra due to observed clear-sky differences in reflectance; however, threshold differences would yield a consistent bias in cloud amount, while the differences shown in Figure 2 are not biased in this way and do contain expected variations in geographic regions characterized by specific cloud regimes. For example, over ocean surfaces, Aqua generally has a greater cloud fraction, with the notable exception over the marine stratocumulus regions.

Because of the diurnal variation in stratocumulus (Minnis and Harrison, 1984; Minnis et al., 1992) it is expected that Terra and Aqua cloud amounts in regions of stratocumulus will vary with a seasonal dependence on the magnitude. The difference is greater in the Peruvian and Namibian regions in December and March than during June and September. Static stability reaches a maximum in these regions during September-November (Klein and Hartmann, 1993) leading to smaller diurnal variations. During December, the Peruvian stratus deck is seen to erode most along the edges between Terra and Aqua observation times. At the center of the cloud deck, where the marine boundary inversion would be climatologically the strongest, the differences between Aqua and Terra are at a minimum. Generally, convective regions over land show greater cloud amounts in the afternoon as detected by Aqua. There are interesting differences in Polar Regions during the equinox months. In March, Terra detects more cloud at both poles, while in September Aqua observes more cloud in the Artic.

The three-hour difference between the Terra and Aqua MODIS data results in global differences on the order of a couple of percent, while regional studies have demonstrated differences of up to 20%. This comparison, contrasting cloud amounts from essentially the same instrumentation and algorithm demonstrates expected variations in the cloud field and encourages us to treat the two satellites products as similar data sets. The next section explores differences that can result from selection of spectral thresholds.

Cloud Detection

Cloud detection is fundamentally a function of the contrast between the target (cloud) and background environment (e.g. ground or atmosphere). The MODIS algorithm relies heavily on contrast in several spectral bands, assigning confidence thresholds to a series of spectral cloud tests (Ackerman et al 1998, King et al, 2003, Platnick et al. 2003). In this section, we explore the sensitivity of cloud detection to specific spectral tests and instrument characteristics.

Figure 3 shows the zonal mean frequencies of cloud conditions in daytime ocean scenes on October 16, 2003, as functions of three cloud detection tests and the combination of all 16 tests from MODIS. Comparing the final results of the cloud mask with the individual tests shows that for this scene type a single spectral test, the reflectance at 0.86 μm, does very well alone. The largest error, only a few percent, occurs around 10°N. This single test works because of the high contrast between clear sky and cloudy conditions and suggests that a comparison of different algorithms should include a comparison of this reflectance test alone to better understand any discrepancies between algorithms. We will use this result later to explore the sensitivity of cloud detection to a specific threshold and viewing geometry.

The BT_{11}-$BT_{3.9}$ difference test is not as sensitive to total cloud cover as the reflectance test. The daytime ocean threshold for assigning cloud to a pixel (outside sun-glint) is BT_{11}-$BT_{3.9}$ < -8 .0 K. During the daylight hours the difference between BT_{11} and $BT_{3.9}$ is large and negative because of reflection of solar energy at 3.9 μm. This technique has proven useful for detecting low-level water clouds. In addition, moderate to large differences between BT_{11} and $BT_{3.9}$ result when a non-uniform scene (e.g., broken cloud) is observed. These differences are due to the differential spectral responses of the two bands to varying scene temperatures as a result of Planck's law.

As expected, the $R_{1.38}$ threshold test underestimates the zonal mean cloud amount. While cloud tests using this MODIS channel detect low-level clouds in dry atmospheres, it is primarily sensitive to thick upper level clouds. The MODIS cloud mask also has a thin cirrus detection algorithm that is not included in the overall results of the final cloud mask, but included as a separate result. The zonal fraction of thin cirrus detected by the $R_{1.38}$ channel, and not detected by any other tests, is shown in Figure 4. This analysis indicates that very thin cirrus generally occupy less that 2% of most zonal regions.

The zonal mean frequencies of cloudy conditions for October 16, 2003 for nighttime ocean scenes as a function of three cloud detection tests and the combination of all nighttime tests from MODIS indicate that the multi-spectral mask (Figure 5) is more sensitive then a single cloud test. This results from the lower contrast between cloud and clear sky at night. The best approach seen here, that makes use of a brightness temperature difference between the observed BT_{11} and the estimated sea surface temperature (SST), still misses approximately 10% of the clouds.

Since the 0.86 μm reflectance test alone is capable of detecting nearly all the clouds over the ocean not affected by sun-glint, it is useful to use this test to explore the sensitivity of cloud detection to a specific visible threshold. Figure 6 demonstrates this sensitivity for daytime ocean conditions equatorward of 60° and away from sun-glint. The figure shows the 0.86 μm reflectance (x-axis) versus the percentage of pixels greater than that value (e.g. cloud fraction if this reflectance was the threshold) as a function of MODIS viewing angle. As viewing geometries vary, cloud detection thresholds also vary (Minnis, 1989). At low reflectances, a small change in the threshold can result in a large change in cloud amount. Since 100% of the pixels have a reflectance greater than 1%, if $R_{0.86} < 1\%$ were set as the threshold for clear sky, all pixels would be labeled cloudy. While the thresholds are a function of view angle, the differences in derived cloud amount become more evident for view angles greater than about 40°. For a fixed reflectance of, say 3%, more cloud would be derived for viewing angles greater than 40° compared to less then 40°. This behavior results from the reflectance properties of clouds, increased IFOV with view angle and a parallax effect (cloud fraction within the IFOV will naturally increase with view angle). A decrease of the threshold from 5.5% to 4% percent would decrease the cloud fraction by approximately 5% for this particular test. The direct impact of any one test on the final result is ameliorated by the use of confidence levels and fuzzy logic in the MOD35 algorithm (Ackerman et al. 1998). The Aqua MODIS thresholds for this test are 3.0%, 4.5%, and 6.5% for 1.0, 0.5, and 0.0 confidence of clear sky, respectively.

As a final test of the sensitivity of cloud detection to a particular threshold, we varied the MODIS band 1 and 2 reflectances ($R_{0.66}$ and $R_{0.86}$ respectively) and the threshold of the 0.86/0.66 μm ratio test to explore the global impact on the derived total cloud amount (Table 1). The tests were performed on daytime Terra data collected on April 1, 2003 between 60°N and 60°S. It is found that the impact is small with a change in cloud amount of less then 1%, except for ocean scenes, where the effect is slightly greater than 2%.

Satellite imager IFOVs are not always completely cloudy or clear, so that cloud edges and sub-pixel scale clouds can cause ambiguity when defining appropriate thresholds (Di Girolamo and Davies, 1997). Because many clouds are organized into spatially non-random systems by radiative and dynamic processes in the atmosphere, a higher proportion of larger IFOVs contain cloud edges and sub-pixel clouds than do smaller IFOVs. To explore the impact of IFOV size on cloud detection, clear sky fractions were determined by increasing the MODIS IFOV from 1 km to larger groupings (e.g. 2 km on a side, 4 km on a side, etc.) but cloud test thresholds were held constant. To be classified as clear in this analysis, all MODIS pixels within a group were required to be labeled as confidently clear or probably clear. Figure 7 shows the percentage of clear sky on Nov 5, 2000 as a function of these simulated footprint sizes. For the increased IFOV to be classified as clear, the reflectance has to satisfy the threshold set by the 1-km pixel so the clear-sky amounts rapidly decrease with increasing footprint size. The value in a 6 km IFOV is typically half that of a 1 km IFOV. IFOV size has a large impact on observed cloud amounts due to sub-pixel cloud fields. The sub-pixel effects can be ameliorated in an algorithm by modifying the clear-sky threshold. Because IFOV size has a large impact on observed cloud amounts, care should be taken when comparing cloud fraction from sensors with differing IFOV sizes.

Instrument swath widths also impact estimates of global cloud amount distributions. To explore this impact on zonal clear-sky amounts, we computed clear-sky fractions from 1-km MODIS observations during October 16 – November 15, 2003 using only pixels within 1° of

nadir (extreme nadir) and pixels within 20° of nadir. Figure 8 details differences in zonal mean clear-sky amounts during this period. As expected, the nadir sampling strategies result in greater clear-sky fractions, or less clouds, when compared to use of the entire swath width. Generally, the difference between the nadir views and the full swath is less than 5%. The impact of sampling is much larger on a regional scale as shown in Figure 9, where differences in cloud amount for a 1° grid can differ by more than ±30%. Thus, nadir and near-nadir viewing can produce similar zonal means but yield large differences regionally.

The studies presented in this section provide insight into the sensitivity of the cloud mask algorithm results to instrument characteristics and algorithm thresholds. Awareness of this sensitivity is necessary for comparing the MODIS cloud detection to other observations, covered in the next section.

Comparison with Lidar/Radar Observations

Ground-based observations

The performance of the MODIS cloud mask has been addressed in several recent papers (King et al, 2003, Platnick et al. 2003, Lee et al, 2004, and Li et al, 2007). In this section we compare MODIS cloud mask results with active sensors from ground, aircraft and satellite platforms.

Three years (2003 through 2005) of the Collection-5 cloud mask algorithm results were compared with those from the Department of Energy (DOE) Atmospheric Radiation Measurement (ARM) program Active Remotely Sensed Cloud (ARSCL) product that combines ground-based observations from a micropulse lidar (MPL) and a millimeter-wavelength cloud radar (MMCR) to determine cloud presence and cloud-top heights (Clothiaux et al., 2000). This investigation utilizes the ARSC: retrievals at the Southern Great Plains (SGP) site in Lamont, Oklahoma (Stokes and Schwartz, 1994).

The ARSCL algorithm processes and combines data from the MPL and MMCR to determine cloud-base and cloud-top altitude at a vertical spatial resolution of forty-five meters and a temporal resolution of ten seconds. The ARSCL algorithm processes the four modes of MMCR operational output and merges it with the output of the MPL to produce cloud-top height retrievals. The present comparison with MODIS focuses on the cloud detection of the algorithm, using ARSCL cloud height retrieval only as an analysis tool.

Comparing cloud detection methods from two independent sources that retrieve cloud properties based on different physical principles over different spatial and temporal scales and viewing geometry makes for a difficult process. A group of 5×5 MODIS observations centered on the ARM site is used in the comparison, averaging the final cloud mask confidences (Ackerman et al 1998) and assuming a value of greater than 0.95 represents a clear scene. The radiances were collected from the MODIS direct broadcast system at the University of Wisconsin-Madison and used as input to the Collection 5 MODIS cloud mask. The ARSCL cloud fraction is defined as the fraction of samples determined cloudy over a 30 minute time period, with a cloud fraction of less than 5% considered to be clear.

Table 2 lists the comparison between the Terra and Aqua MODIS and the ARSCL cloud data sets. There is agreement between MODIS and ARSCL in approximately 83% of the collocated observations with little difference in skill score with season. Next, we explore cases when the two results differ and propose some possible causes.

First, we explore cases where MOD35 flagged the scene as cloudy while the ARSCL data set indicated clear. Figure 10 plots the average confidence level of these cases as a function of the standard deviation of the MODIS confidence level in the group of pixels around the ARM site. Those observations that are determined by MODIS as cloudy while ARCL is indicating clear are mostly associated with the average MODIS confidence flag near 0.90 (Figure 10), where we have defined a value of greater than 0.95 as clear. The low standard deviation indicates that the scenes are likely to be uniform, suggesting errors in the MODIS classification.

Those cases in which MODIS defines clear and ARSCL cloudy are explored in Figure 11 by plotting the ARSCL cloud altitude versus the average ARSCL cloud fraction over the 30-minute sampling period. Discrepancies occur for low cloud fractions, but these are not the majority of cases. Most differences occur for cloud top altitudes greater than 8 km, suggesting MODIS is missing some cirrus. The MODIS sensitivity to cirrus is greatest over the topical waters and thick vegetation as the $R_{1.38}$ threshold can be set low and variations of the IR window surface emissivity are small. In the mid-latitudes, lower water vapor amounts and spectral variations of the surface make detection of thin cirrus more difficult.

The difference in cloud detection rates for high clouds raises the issue of algorithm sensitivity to cloud optical depth. Next, we determine the minimum cloud optical depth that the MODIS algorithm can flag as cloudy.

Optical Depth Sensitivity

We take two independent approaches to estimating cloud optical detection limits: 1) compare observations of the MODIS Airborne Simulator (MAS) taken on board a high-altitude aircraft with coincident lidar observations, and 2) compare cloud mask results from the MODIS cloud mask with ground-based measurements of visible optical depth from the Arctic High-Spectral Resolution Lidar (HSRL). The MAS has a different fov and noise performance compared to MODIS and thus cannot be used to directly validate MODIS. Since the MAS cloud detection algorithm is essentially the same as the MODIS, we use the MAS to assess the capability of the algorithm approach to detecting clouds.

Comparisons were made using the ER-2 borne cloud physics lidar (CPL) and collocated observations of the MAS (King et al. 1996). The CPL, developed by NASA Goddard, flies on the ER-2 high altitude aircraft (McGill, 2002). The CPL is an active remote sensing system, capable of high vertical resolution cloud height determinations

(30 meters), cloud visible optical depth, and backscatter depolarization. The CPL laser transmits at 355, 532, and 1064 nm and fires 5000 shots/sec. The high sample rate of the CPL results in a surface footprint that can be approximated as a continuous line with a diameter of 2 meters. The MAS is a scanning spectrometer with a 2.5 mrad field of view. The MAS scene mirror scans at 7.25/sec with a swath width of 42.96° from nadir resulting in a 50-meter nadir surface resolution with a swath width of 37.2 km at the 20 km ER2 flight altitude (King, 1996). The MAS has 50 spectral channels located within the 0.55 – 14.2 μm spectral region.

The MODIS cloud detection algorithm was based on using the MAS observations as proxy to the MODIS, as discussed by Ackerman et al (1998). The collocation of these data sets is discussed in Holz et al (2006). Because CPL is a nadir only measurement only MAS nadir fov are compared for this investigation. To explore the optical depth sensitivity we consider those cases where the MAS detects clear sky and the lidar detects a cloud, and analyze the lidar retrieved optical depth. Figure 12 shows the number of occurrences where the MAS scene was identified as clear and the cloud physics lidar (McGill, 2002) detected a cloud as a function of the visible optical depth. This analysis suggests that a minimum requirement for cloud detection as defined by optical depth is approximately 0.4, as clouds with smaller optical depths are often classified as clear. To explore this further, we consider a comparison with the High Spectral Resolution Lidar (HSRL).

The HSRL observes both the Rayleigh and Mie (i.e., molecular and aerosol) backscatter simultaneously in two separate channels. The addition of a molecular channel where the backscattering cross-section is known, allows the cloud extinction profile to be derived directly from the observations without assumptions. The HSRLs observes cloud extinction profiles with a high spatial and temporal resolution, a capability that makes HSRL observations unique and very powerful for invetigating the MODIS cloud mask sensitivity to cloud optical depth. The

UW-Madison has pioneered the advancement of HSRLs over the last three decades (e.g. Eloranta, 2005). The current Arctic-HSRL (AHSRL) provides time histories of the following cloud and aerosol variables: 1) optical depth profiles as a function of altitude, 2) circular depolarization profiles as a function of altitude, which allows discrimination between ice crystals and water droplets, 3) backscatter cross-section as a function of altitude, 4) cloud base altitude, and 5) cloud top altitude for clouds of optical depths less than approximatly 2.5. Raw data is acquired at 7.5 m range intervals with 0.5 second time resolution. All vertical profiles begin at an altitude of 100 m and extend to 30 km. A cloud is considered to occupy a layer when the aerosol backscatter cross-section is greater than $1E^{-6}$ $(m\ str)^{-1}$. When dense clouds are present, useful data will be present up to an altitude where the optical depth reaches approximately 2.5.

The AHSRL was operated at Madison, WI in an automated manner during January through September 2004. Table 3 shows the comparison between MODIS cloud detection and the AHSRL including both day and night cases for both Terra and Aqua satellites. The two cloud detection methods agree approximately 70% of the time. Figure 13 is a scatter diagram of AHSRL optical depth versus AHSRL determined cloud top for MODIS cloudy (Figure 13 left panel) and clear scenes (Figure 13 right panel.) While there are cases when MODIS detects clouds for AHSRL optical depths less then 0.4, much of the disagreement between the AHSRL and MODIS occurs for optical depths less than 0.4. Figure 14 presents an example of optically thin cirrus where MODIS labels the scene as clear and AHSRL detects cloud. The observation is for August 22, 2004, and the MODIS views the AHSRL region at approximately 8:39 UTC. During this time, the AHSRL is clearly detecting an optically thin cloud with an optical depth less then 0.1 at approximately 10 and 11.5 km along with an aerosol layer near the surface. The total optical depth of the cloud/aerosol column is 0.2 with the aerosol optical depth contributing approximately three quarters of the total optical depth. The MODIS cloud mask does not have sensitivity to this thin cirrus.

Figure 15 is the cumulative frequency of AHSRL optical depth for when collocated MODIS detects a clear scene. Of those cases where the lidar detected a cloud or aerosol and MODIS indicated clear, more than 60% of the time the optical depth was less than 0.2 and 90% of the time the non-molecular optical depth was less than 0.4.

We next compare the MODIS cloud detection over the Arctic with observations from Geoscience Laser Altimeter System (GLAS). Polar regions at night are the most challenging scenes in which to detect clouds with passive radiometers.

GLAS Satellite Observations

The launch of GLAS on board the Ice, Cloud and Land Elevation Satellite (ICESat Zwally et al., 2002) platform in January 2003 provides space-borne laser observations of atmospheric layers. Mahesh et al (2004) compared GLAS cloud observations with an earlier version of the MODIS cloud mask and found that in more than three-quarters of the cases, MODIS scene identification agreed with GLAS. Disagreement between the two instruments was largest over snow-covered surfaces in the northern hemisphere, and MODIS cloud detection with sunlit observations was more robust than observations made at night.

The comparison in this study uses MODIS Terra Collection-5 cloud mask data from the period October 16 – November 18, 2003. The MODIS data were aggregated from Level 2 (5-minute granule) files while the GLAS were averaged from medium-resolution daily values. The time period coincides with that of the fully functional 532 nm channel on the GLAS. MODIS spatial resolution is 1-km and GLAS is about 70-m across-track × 7000-m along-track (one result per second). Both data sets were sorted into 2.5-degree equal-area grids, then converted to equal-angle for display purposes. MODIS and GLAS mean cloud amounts are compared for 2.5-degree equal area grid cells in the Arctic. MODIS cloud fractions for this region are shown in Figure 16 along with MODIS minus GLAS cloud frequencies. The GLAS detects more clouds for most grid cells, especially over the Arctic Ocean and Greenland ice sheet where reduced visible and thermal

contrast make cloud detection more difficult for passive retrievals. This comparison includes all MODIS observations, so there are times when MODIS indicates large cloud amount, which results from a combination of different measurements but also the nadir only viewing of the GLAS. Differences are largest north of the Laptev Sea and the East Siberian Sea, where differences are larger than –30%. An analysis of the distribution of MODIS minus GLAS cloud fractions indicates a mode of -10%.

The GLAS is nadir viewing only and since cloud detection is a function of view angle (see Figure 9), a comparison with only nadir views of MODIS was conducted. The impact of including only nadir views is shown in Figure 17; zonal mean MODIS and GLAS cloud fraction differences for the time period are plotted. The differences are approximately –5% for the daylight regions of this comparison, and get as large as –20% for regions that lack solar illumination. The comparison shown in Figure 17 includes all MODIS pixels as well as nadir only, defined as the middle two pixels of each scan line. Including only nadir pixels reduces the MODIS cloud cover by approximately 5%, worsening the agreement with GLAS. The results of this comparison with GLAS are similar, though a slightly better comparison, than the earlier study of Mahesh et al (2004).

Summary

This paper provides a comprehensive study of the cloud detection capability of the MODIS cloud mask algorithm. Validation was conducted through comparison with active observing systems that are generally more sensitive to the presence of clouds; however, the ground-based observations do not allow an assessment of the cloud detection capability for all scenes types. The comparisons with four different lidar systems can be summarized as follows:

- Agreement between MODIS and the ARSCL for both cloud and clear scenes is approximately 85%.

- Comparison with GLAS during October 16 – November 18, 2003, indicates that issues remain with cloud detection over polar regions during night. A more detailed analysis with CALIPSO is underway.
- Through a comparison with cloud optical depths measured by a ground-based Arctic High-spectral Resolution Lidar (HSRL), the MODIS cloud mask algorithm appears most sensitive to clouds with an optical depth greater than 0.4. This is consistent when analogy is made with the CPL and MAS analysis on the ER-2.

The paper also demonstrates the sensitivity of the cloud masking approach to various thresholds and conditions. Nadir viewing sampling generally yields less cloud amount regionally than does the use of an entire swath, and a small IFOV generally detects more clear-sky scenes. Over clear-sky, sun-glint free ocean, the reflection test at 0.86 μm detects nearly all the clouds found by the complete algorithm. As many satellites have this channel it would be a valuable exercise for various cloud detection algorithms to compare cloud amounts using only this test to understand the impacts of various instrument-sampling characteristics.

Acknowledgement

This research was funded under NASA grants NNG04HZ38C and NNG04GL14G; NNG04GB93G also contributed to this study. The authors continue to appreciate the support provided by the MODIS Characterization and Support Team and the MODIS Science Data Support Team. These research efforts have been supported by a number of agencies and research programs; a particular acknowledgement is due the NASA Radiation Sciences Program and the NASA Earth Observing System Project Science Office. Thanks to the MODIS science team for many fruitful discussions. DOE ARM SGP site ARSCL data were obtained from the Atmospheric Radiation Measurement (ARM) Program sponsored by the U.S. Department of Energy, Office of Science, Office of Biological and Environmental Research, Environmental Sciences Division.

References

Ackerman, S. A., K. I. Strabala, W. P. Menzel, R. A. Frey, C. C. Moeller, and L. E. Gumley (1998), Discriminating clear-sky from clouds with MODIS, J. Geophys. Res., 103(D24), 32,141– 32,157.

Barnes, W. L., T. S. Pagano, and V. V. Salomonson (1998), Prelaunch characteristics of the Moderate Resolution Imaging Spectroradiometer (MODIS) on EOS-AM1, IEEE Trans. Geosci. Remote Sens., 36, 1088-1100.

Clothiaux, E. E., T.P. Ackerman, G. G. Mace, K. P. Moran, R. T. Marchand, M. A. Miller, and B. E. Martner, 2000: Objective determination of cloud heights and radar reflectivities using a combination of active remote sensors at the ARM CART sites. *J. Appl. Meteor.,* **39,** 645-665.

Di Girolamo, L. and R. Davies, 1997: Cloud fraction errors caused by finite resolution measurements. *Jour. Geo. Res.,* **102**, D2, 1739–1756.

King, M. D., W. P. Menzel, P. S. Grant, J. S. Myers, G. T. Arnold, S. E. Platnick, L. E. Gumley, S. C. T say, C. C. Moeller, M. Fitzgerald, K. S. Brown and F. G. Osterwisch, 1996: Airborne scanning spectrometer for remote sensing of cloud, aerosol, water vapor and surface properties. *J. Atmos. Oceanic Technol*., **13**, 777-794.

King, M. D., W. P. Menzel, Y. J. Kaufman, D. Tanre´, B. C. Gao, S. Platnick, S. A. Ackerman, L. A. Remer, R. Pincus, and P. A. Hubanks (2003), Cloud and aerosol properties, precipitable water, and profiles of temperature and humidity from MODIS, IEEE Trans. Geosci. Remote Sens., 41, 442– 458.

Kline, S. A. and D. L. Hartmann, 1993: The seasonal cycle of low stratiform clouds. J. Climate, 6, 1587-1606.

Lee, Y., G. Wahba, and S. A. Ackerman, 2004: Cloud Classification of Satellite Radiance Data by Multicategory Support Vector Machines. *J. Atmos. Oceanic Tech.* **21**, 159-169.

Li, Z., J. Li, W. P. Menzel, T. J. Schmit, and S. A. Ackerman, 2007: Comparison between current and future environmental satellite imagers on cloud classification using MODIS. Accepted for publication in *Remote Sensing of Environment*.

Liu, Y., J. Key, R. Frey, S. Ackerman, and W. Menzel, Nighttime polar cloud detection with MODIS, Remote sensing of environment, **92**, 181-194, 2004.

Mahesh, A., M. A. Grey, S. P. Palm, W. D. Hart and J. D. Spinhirne, Passive and active detection of clouds: Comparisons between MODIS and GLAS observations, *J. Geophys. Res.,*108, L04108-L04108, 2004.

McGill, M., D. Hlavka, W. Hart, V. S. Scott, J. D. Spinhirne, and B. Schmid, 2002: Cloud Physics Lidar: Instrument description and initial measurement results. *Appl. Opt.,* **41,** 3725–3734.

Minnis, P. and E. F. Harrison, 1984: Diurnal variability of regional cloud and clear-sky radiative parameters derived from GOES data. Part II: November 1978 cloud distributions. *J. Climate Appl. Meteor.,* **23,** 1012–1051.

Minnis, P., 1989: Viewing Zenith Angle Dependence of Cloudiness Determined >From Coincident GOES East and GOES West Data. *J. Geophys. Res*., **94**, 2303-2320.

Minnis, P., P. W. Heck, D. F. Young, C. W. Fairall, and J. B. Snider, 1992: Stratocumulus cloud properties derived from simultaneous satellite and island-based instrumentation during FIRE. *J. Appl. Meteor.,* **31,** 317–339.

Platnick, S., M. D. King, S. A. Ackerman, W. P. Menzel, B. A. Baum, J. C. Rie´di, and R. A. Frey (2003), The MODIS cloud products: Algorithms and examples from Terra, IEEE Trans. Geosci. Remote Sens., 41, 459– 473.

Rossow, W. B., A. W. Walker, and L. C. Gardner, 1993: Comparison of ISCCP and other cloud amounts, *J. Climate*, 6:2394-2418.

Rossow, W. B., 1989: Measuring cloud properties from space. A review. *J. Climate*, **2**, 201-213.

Stokes, G. M., and S. E. Schwartz, 1994: The Atmospheric Radiation Measurement (ARM) Program: programmatic background and design of the cloud and radiation test bed. *Bull. Amer. Meteor. Soc.,* **75,** 1201-1221.

Thomas, S. M., A. K. Heidinger, and M. J. Pavolonis, Comparison of NOAA's operational AVHRR-derived cloud amount to other satellite-derived cloud climatologies. Journal of Climate, Volume 17, Issue 24, 2004, pp.4805-4822. Call Number: Reprint # 3992

Wylie, D. P., W. P. Menzel, H. M. Woolf, and K. I. Strabala, 1994: Four years of global cirrus cloud statistics using HIRS. *J. Climate,* 7, 1972-1986.

Zhao, G. and L. Di Girolamo, 2006: Cloud fraction errors for trade wind cumuli from EOS-Terra instruments. *Geo. Res. Lett.*, **33**, L20802. 5p

Zwally, H. J., B. Schutz, W. Abdalati, J. Abshire, C. Bentley, A. Brenner, J. Bufton, J. Dezio, D. Hancock, D. Harding, T. Herring, B. Minster, K. Quinn, S. Palm, J. Spinhirne, R. Thomas, 2002: ICESat's laser measurements of polar ice, atmosphere, ocean and land. *Jour. Geodynamics* **34**, 405–445.

Table 1 Cloud amount (60S-60N) as a function of Reflectance Biases and Reflectance Thresholds

	Cloud Amount
Collection 5 cloud mask	Water 72.7% Land 54.1%
Increase all B1 and B2 reflectance by 5% of the original	Water 73.3% Land 54.6%
Decrease all B1, B2 reflectance by 5% of original	Water 72.2% Land 53.6%
Increase VIS/NIR Reflectance test threshold by 1%	Water 70.7% Land 54.1%
Decrease VIS/NIR Reflecatnce test threshold by 1%	Water 75.5% Land 54.7%

Table 2 Comparison of MODIS cloud detection with the ARSCL over the ARM site of the Southern Great Plains.

	ARCL clear	ARCL cloudy
MODIS clear	Terra: 146 Aqua: 117	Terra: 45 Aqua: 58
MODIS cloudy	Terra: 38 Aqua: 12	Terra: 298 Aqua: 185

Table 3 Comparison of MODIS cloud detection with the AHSRL over Madison, WI.

	AHSRL clear	AHSRL cloudy
MODIS clear	39	133
MODIS cloudy	46	362

Terra Cloud Fraction Daytime

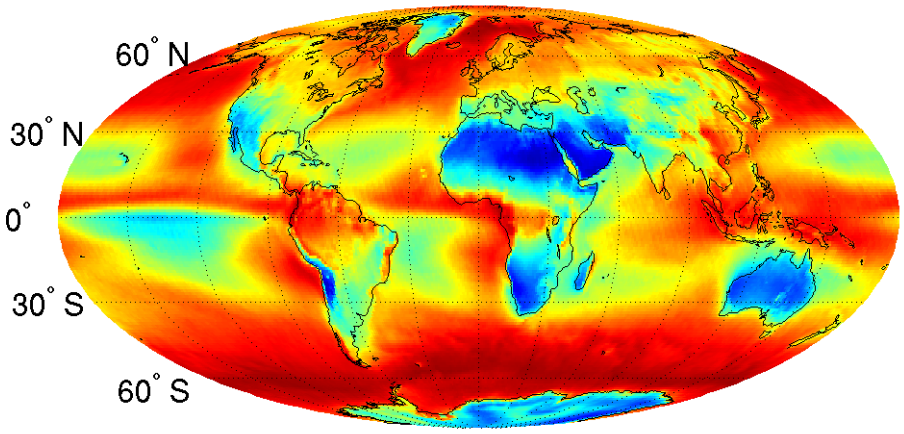

Aqua Cloud Fraction Daytime

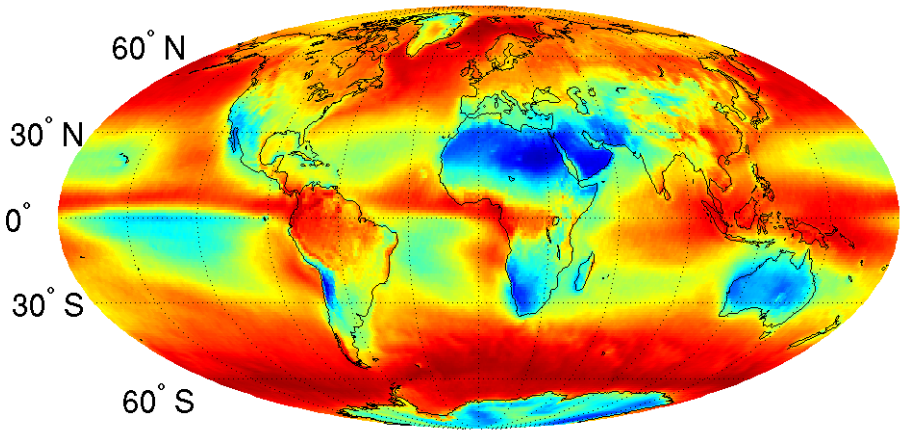

Figure 1: The mean daytime cloud fractions for MODIS Terra (top) and MODIS Aqua (bottom) for August 2002 through July 2007. Overall these cloud patterns over much of the globe are similar.

March

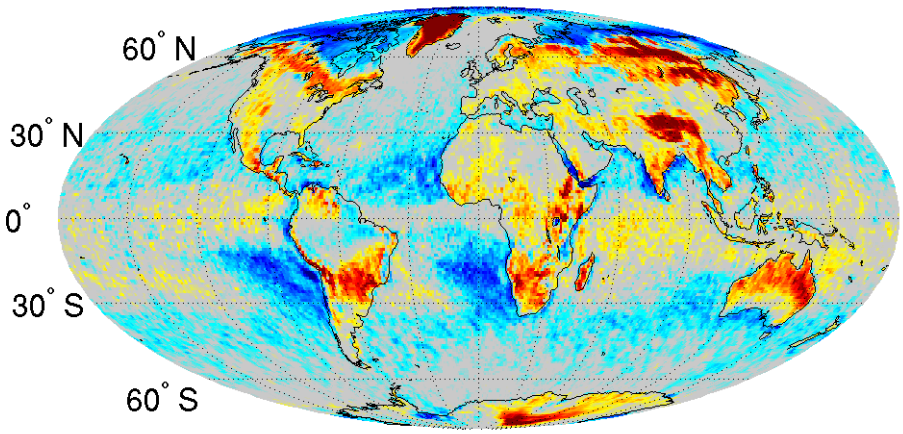

June

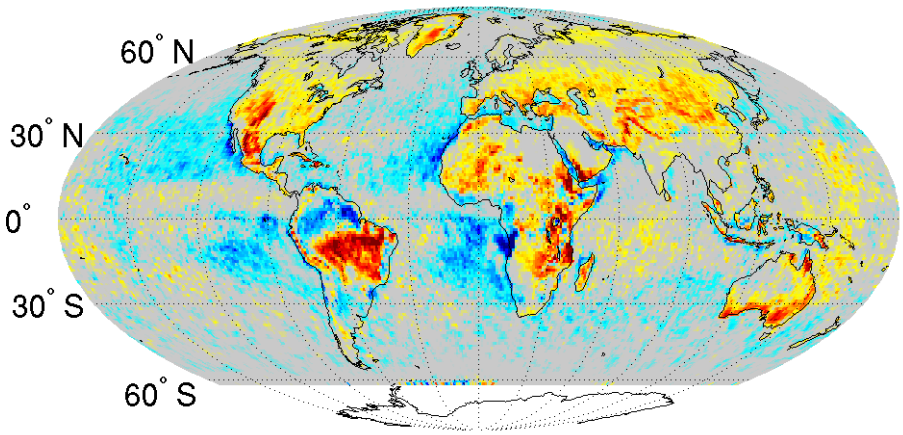

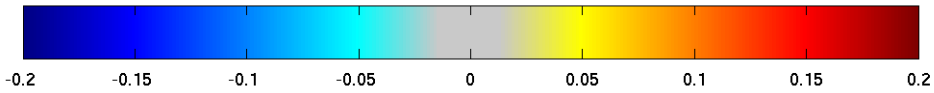

September

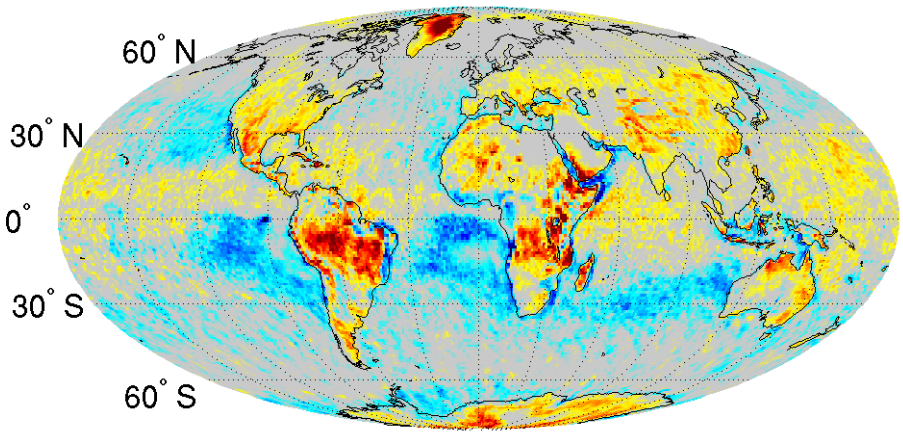

December

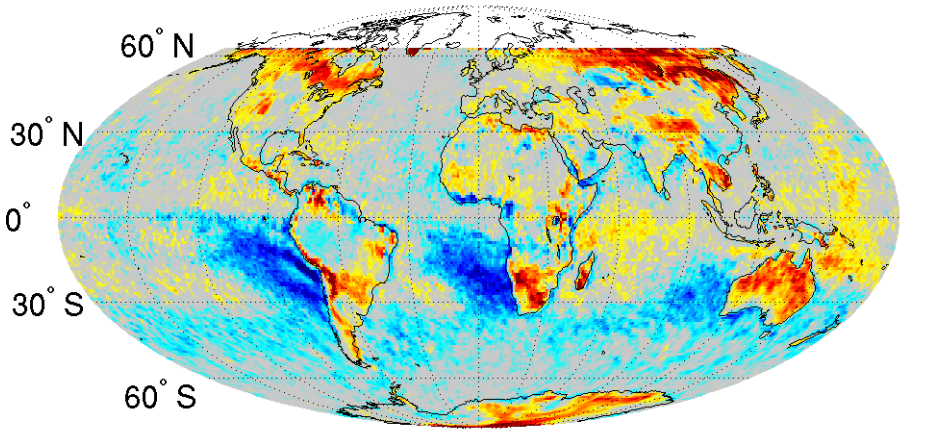

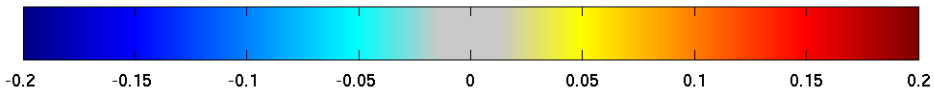

Figure 2: The images show MODIS Aqua minus MODIS Terra monthly mean daytime cloud fraction for 5 years (August 2002 – July 2007) for March, June, September and December.

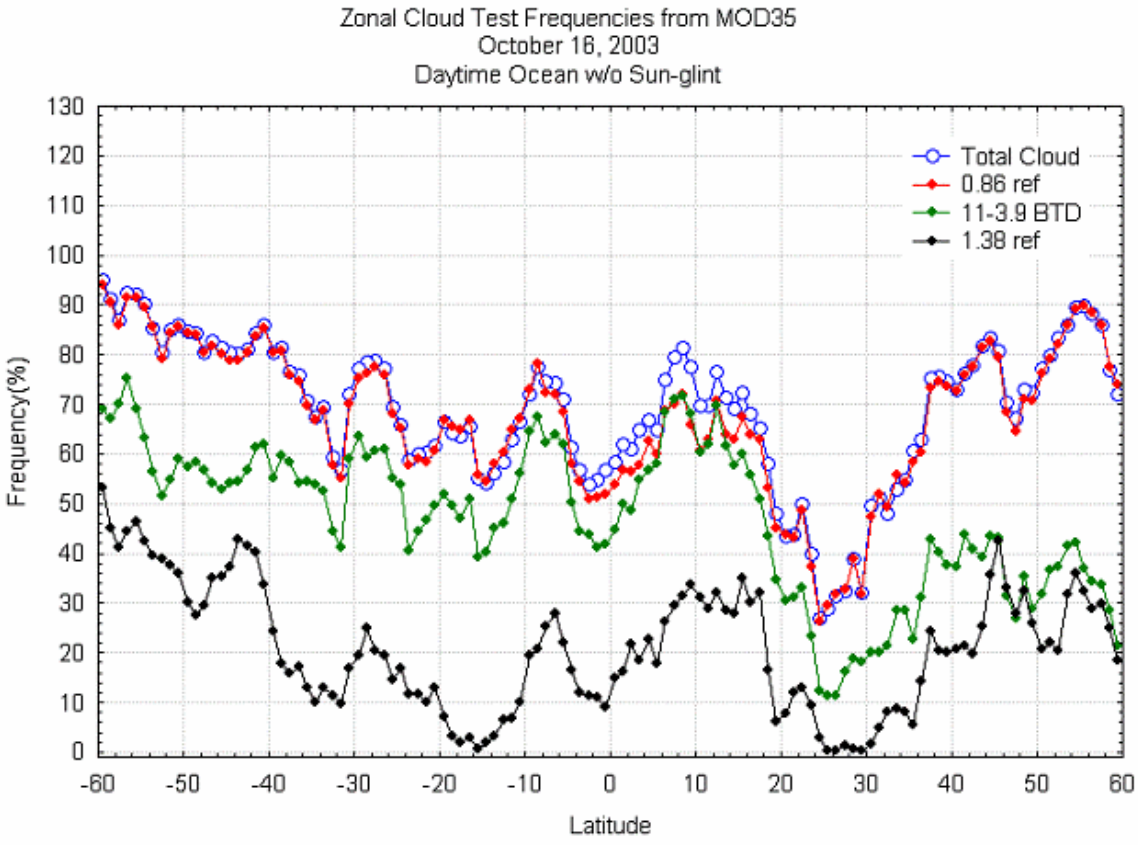

Figure 3 Zonal mean frequencies of cloudy conditions for October 16,2003, daytime ocean scenes as a function of three threshold cloud detection tests and the combination of all 16 tests from MODIS.

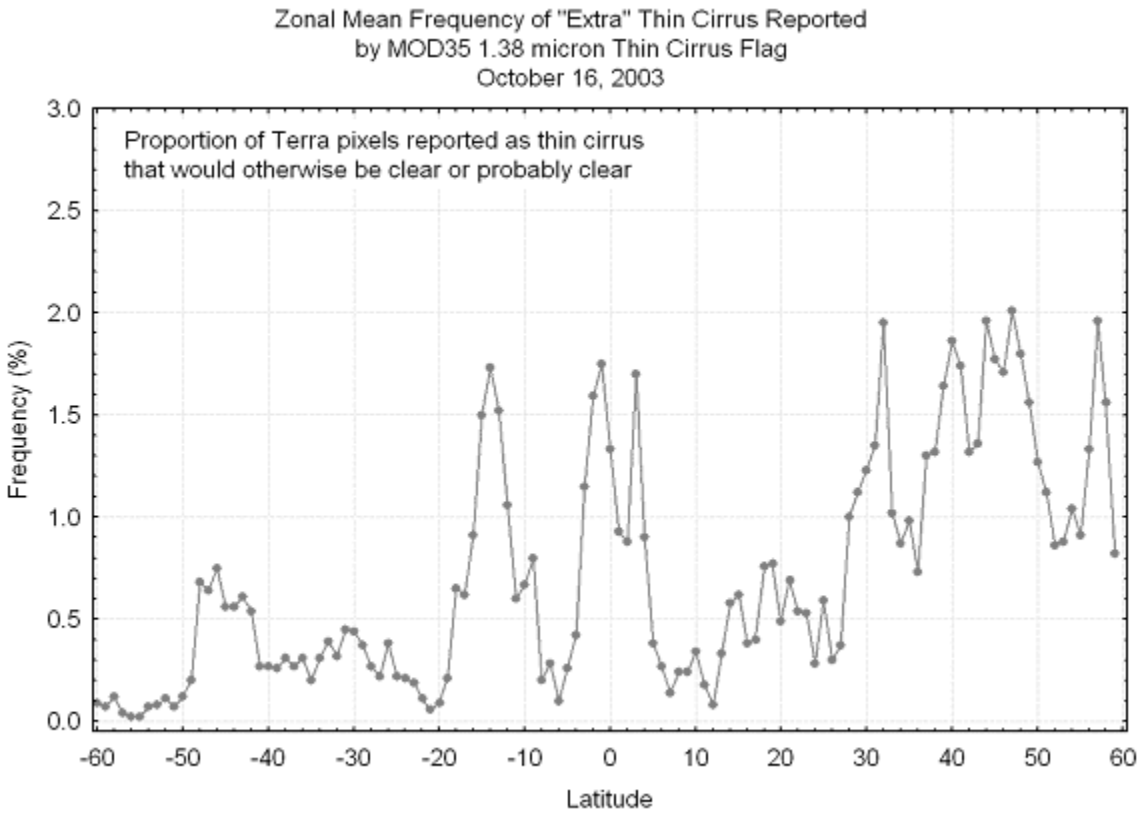

Figure 4 Additional zonal mean cloud fraction due to thin cirrus using the 1.38 micron channel of Terra MODIS. Other tests in the algorithm indicate the pixel to be clear or probably clear.

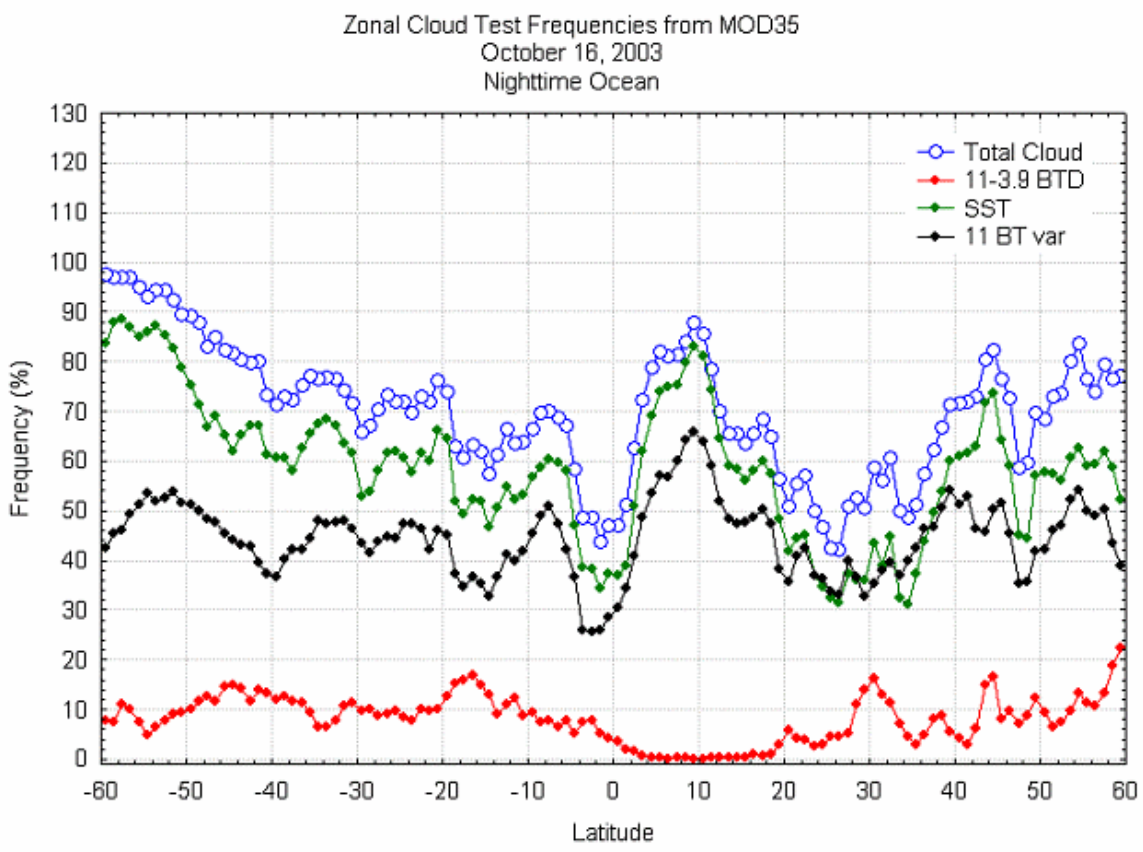

Figure 5 Zonal mean frequencies of cloudy conditions for October 16, 2003, nighttime ocean scenes as a function of three cloud detection tests and the combination of all tests (blue) from MODIS.

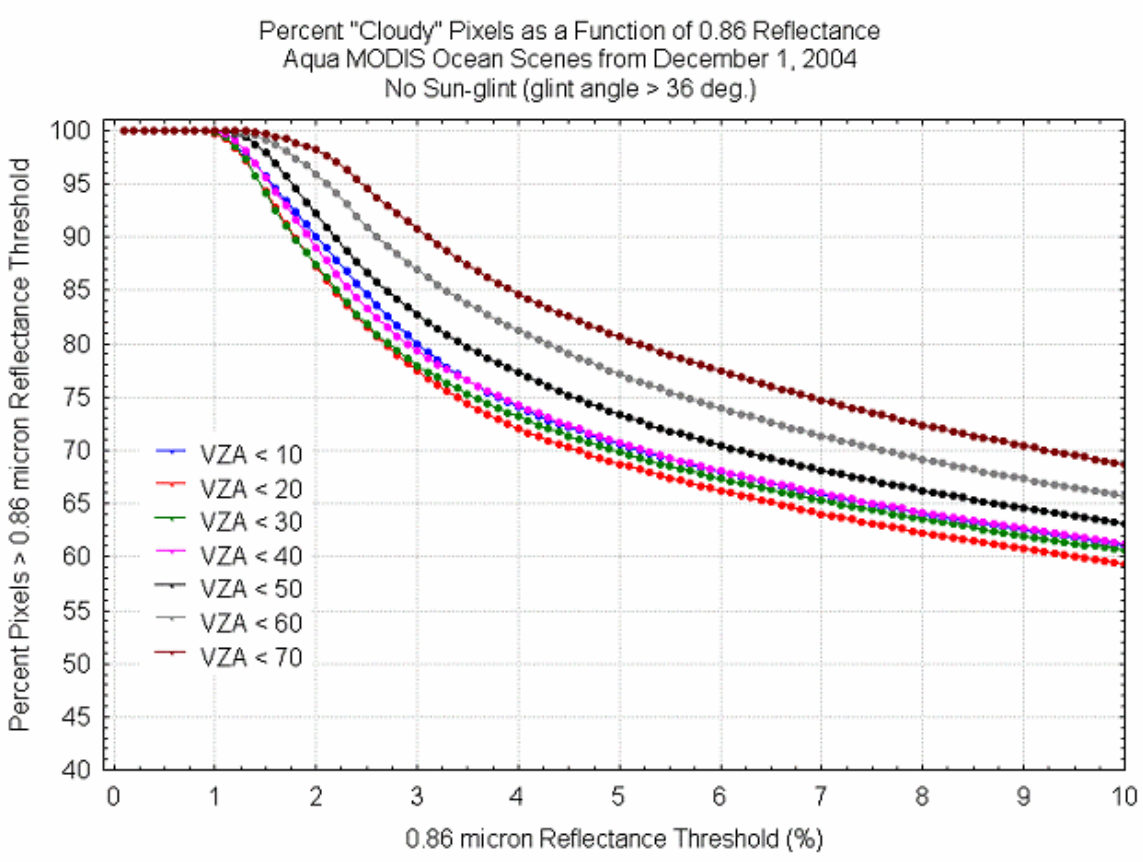

Figure 6 The percentage of pixels with a reflectance at 0.686 microns greater than a given value for seven viewing zenith angles. Aqua MODIS data was collected on December 1, 2004 over ocean scenes outside of the sun-glint region.

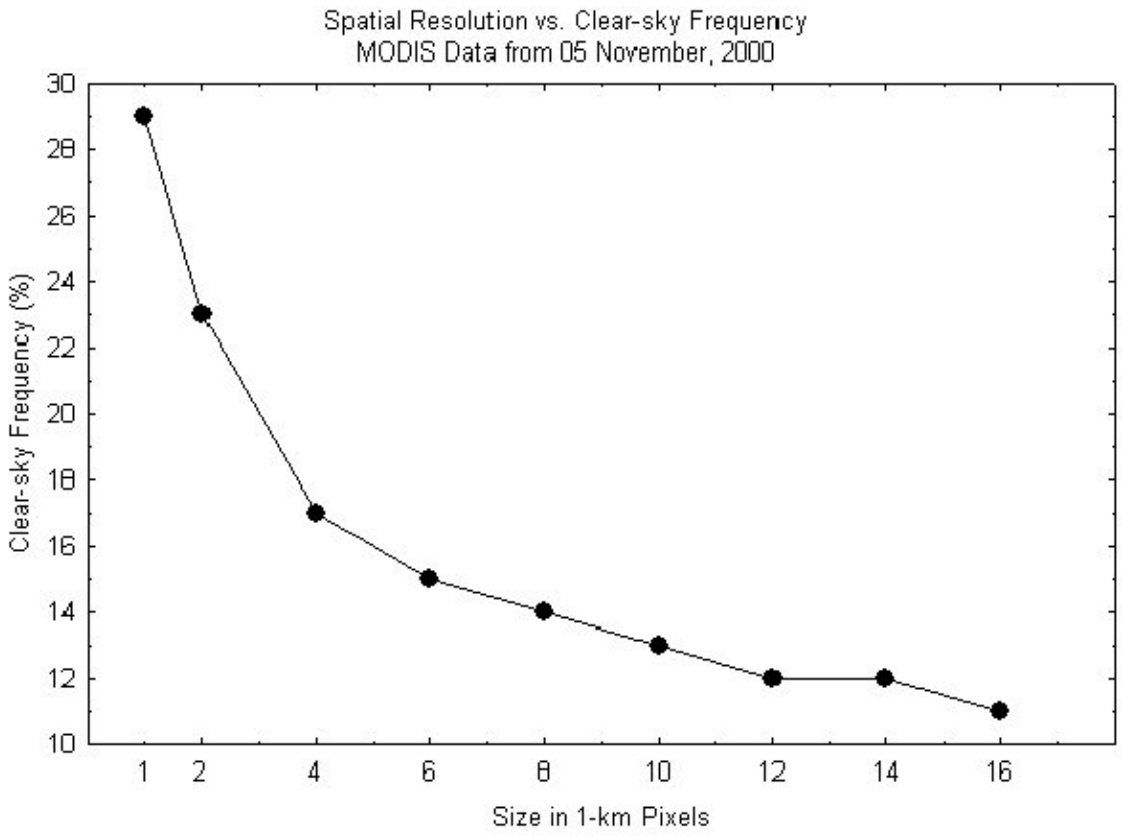

Figure 7 The percentage of pixels labeled as confident clear or probably clear as a function of simulated pixel size using MODIS data collected on November 5, 2000.

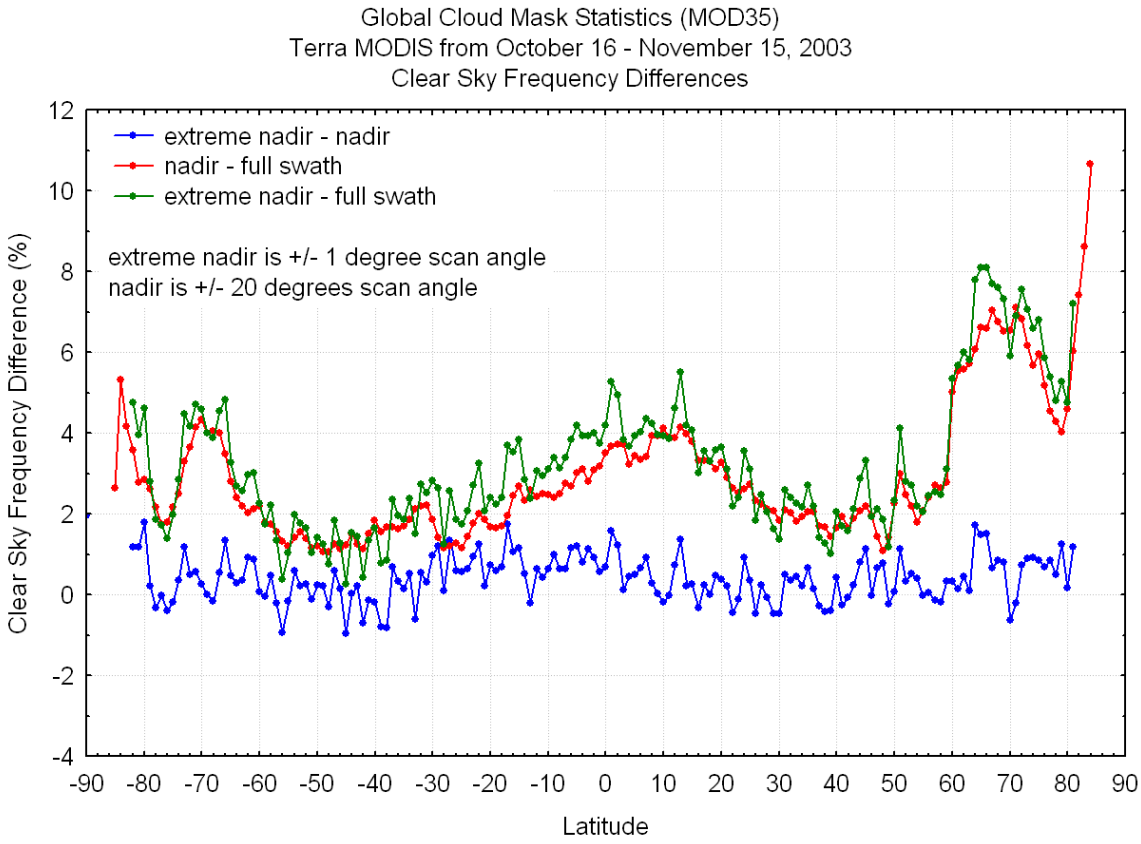

Figure 8 Zonal mean differences (as noted in the legend) in clear-sky frequency between 3 sampling strategies, extreme nadir minus full swath (green), nadir (within 20° of nadir) and extreme nadir (within 1° of nadir) (blue) and nadir and full swath (green). Pixels with high confidence clear or probably clear are considered clear in this study.

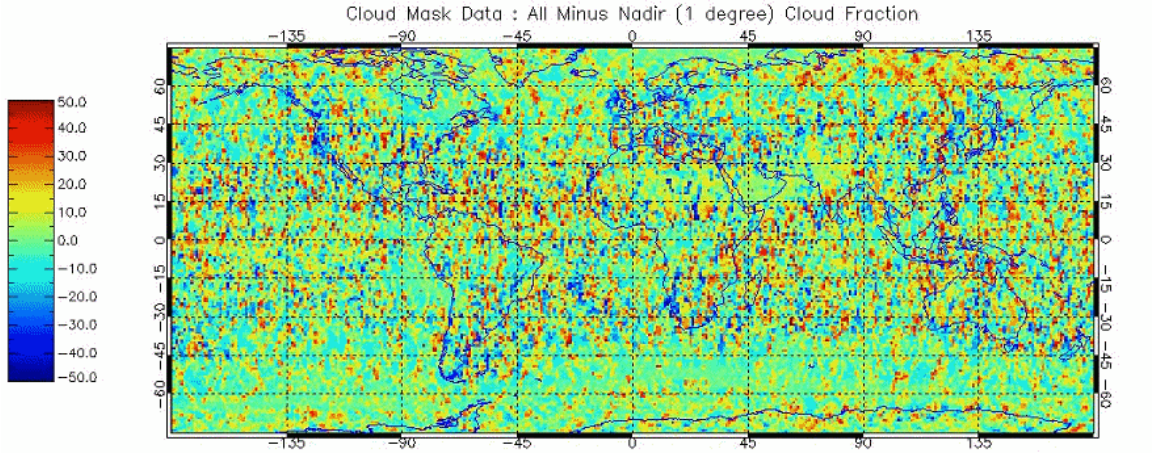

Figure 9 The MODIS cloud mask minus the MODIS nadir only cloud fraction from Terra MODIS from October 16-November 15, 2003.

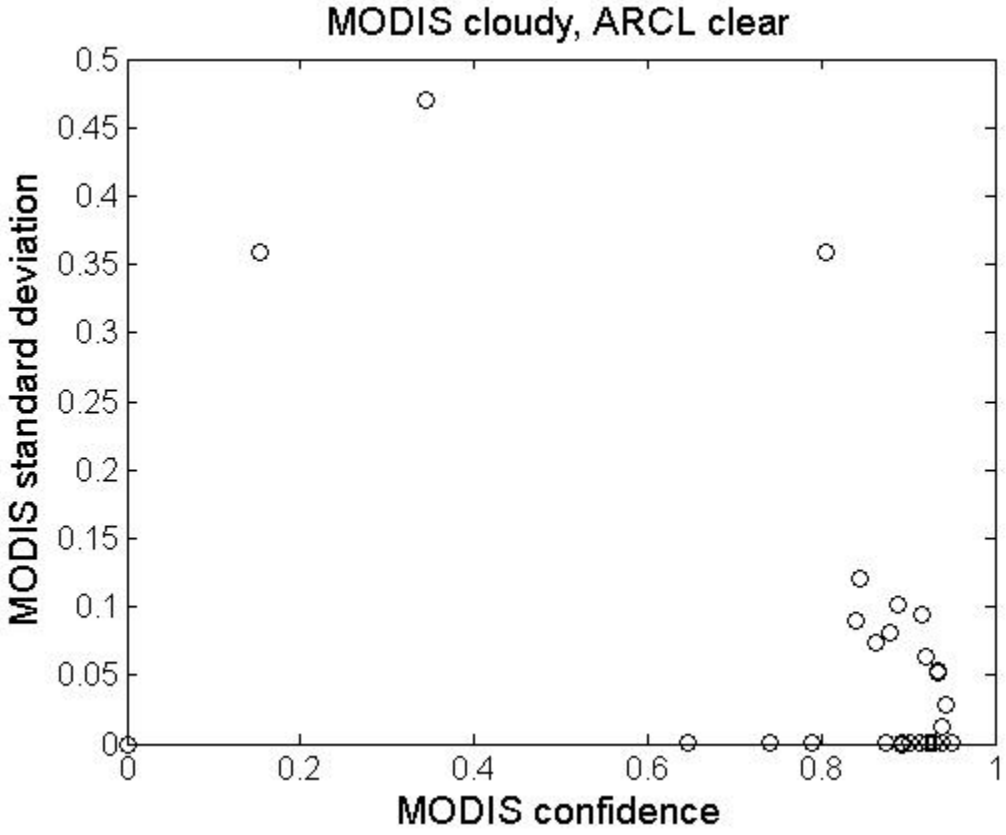

Figure 10 MODIS average confidence level versus standard deviation for cases labeled by MODIS as cloudy and by the ARSCL algorithm as clear. The clear-sky confidence threshold is 0.95.

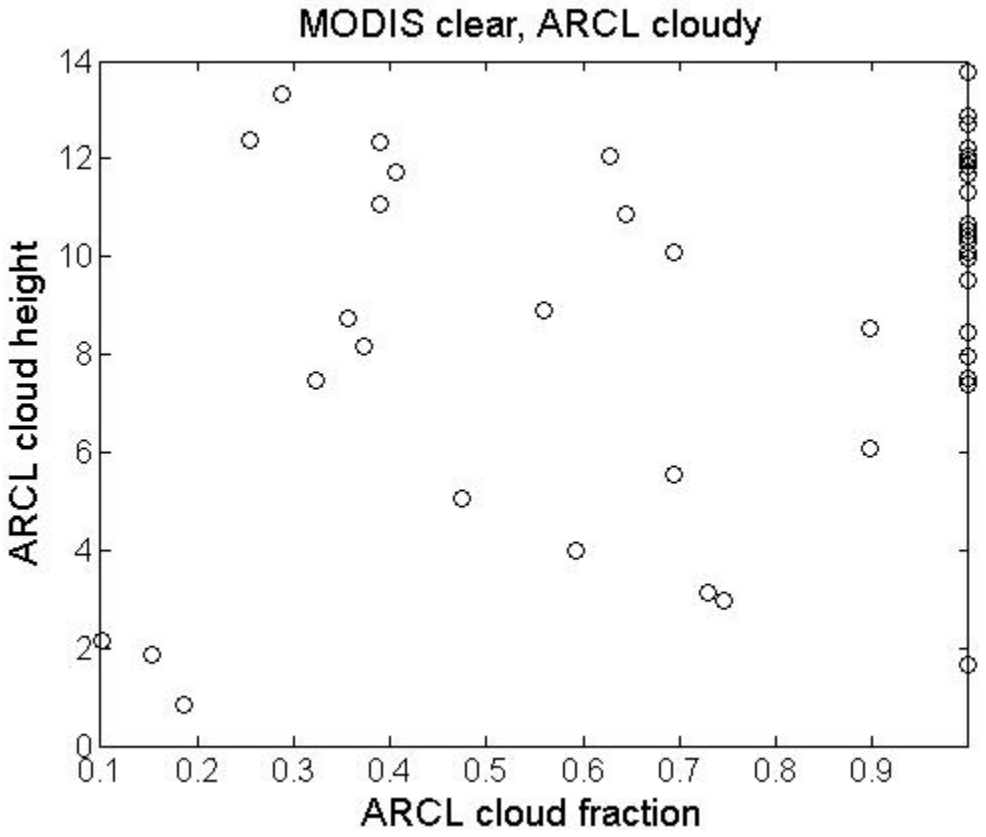

Figure 11 ARSCL cloud fraction as a function of cloud height for those cases labeled as clear by the MODIS algorithm.

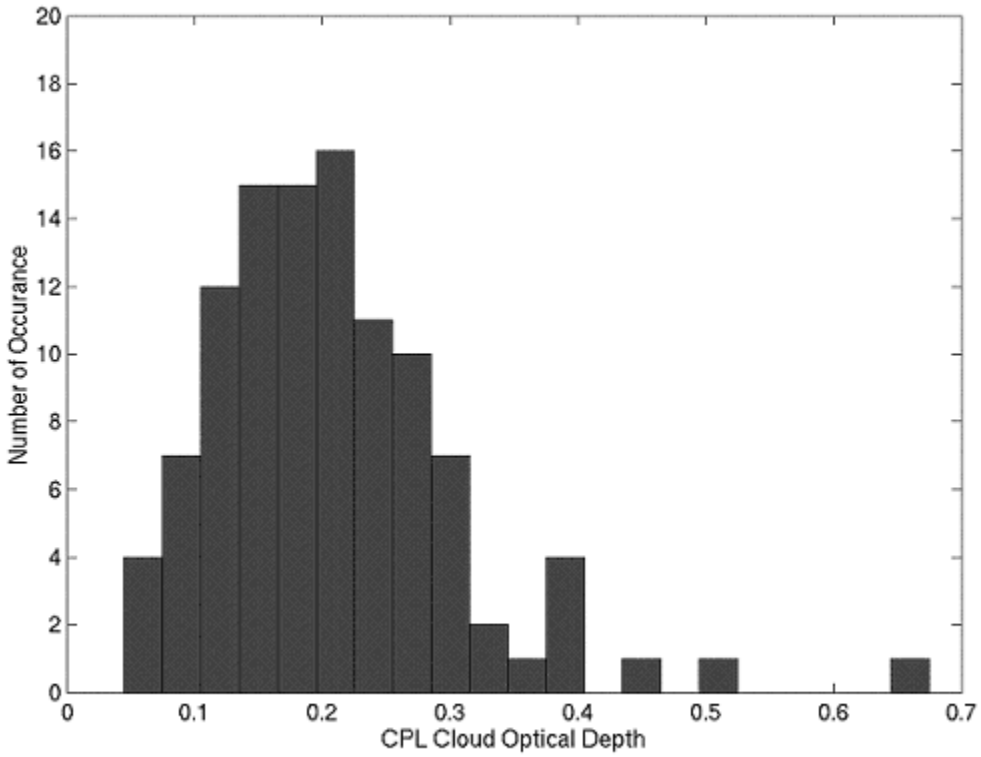

Figure 12 The number of occurrences that a MAS pixel was identified as clear but the CPL (McGill, 2002) detected a cloud with a given cloud optical depth.

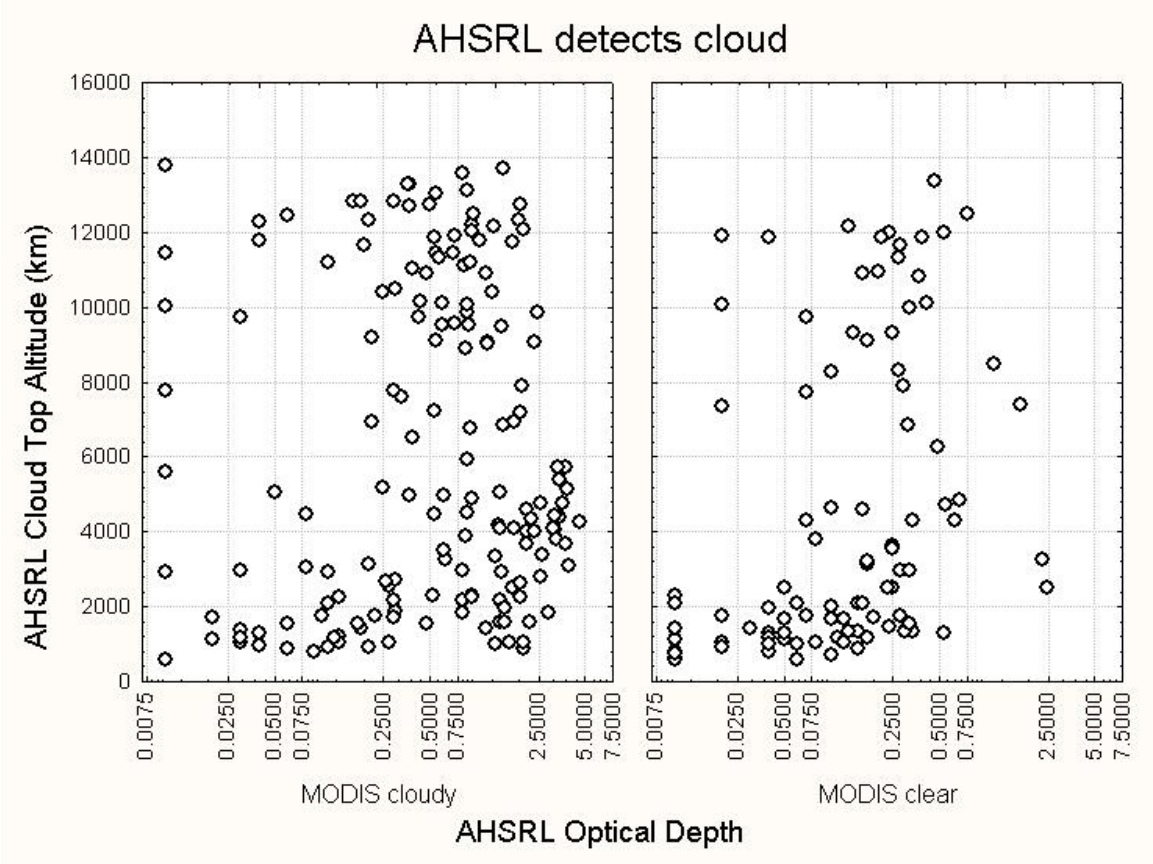

Figure 13 Left: Scatter plot of AHSRL Optical Depth versus AHSRL cloud top altitude for cases where AHSRL and MODIS detected cloudy (considered as MODIS cloudy). Right: Scatter plot of AHSRL Optical Depth versus AHSRL cloud top altitude for cases where AHSRL detected a cloud and MODIS cloud mask indicated clear (Labeled MODIS Clear). Time period for both is January – August in Madison WI in 2004, for both Terra and Aqua overpasses.

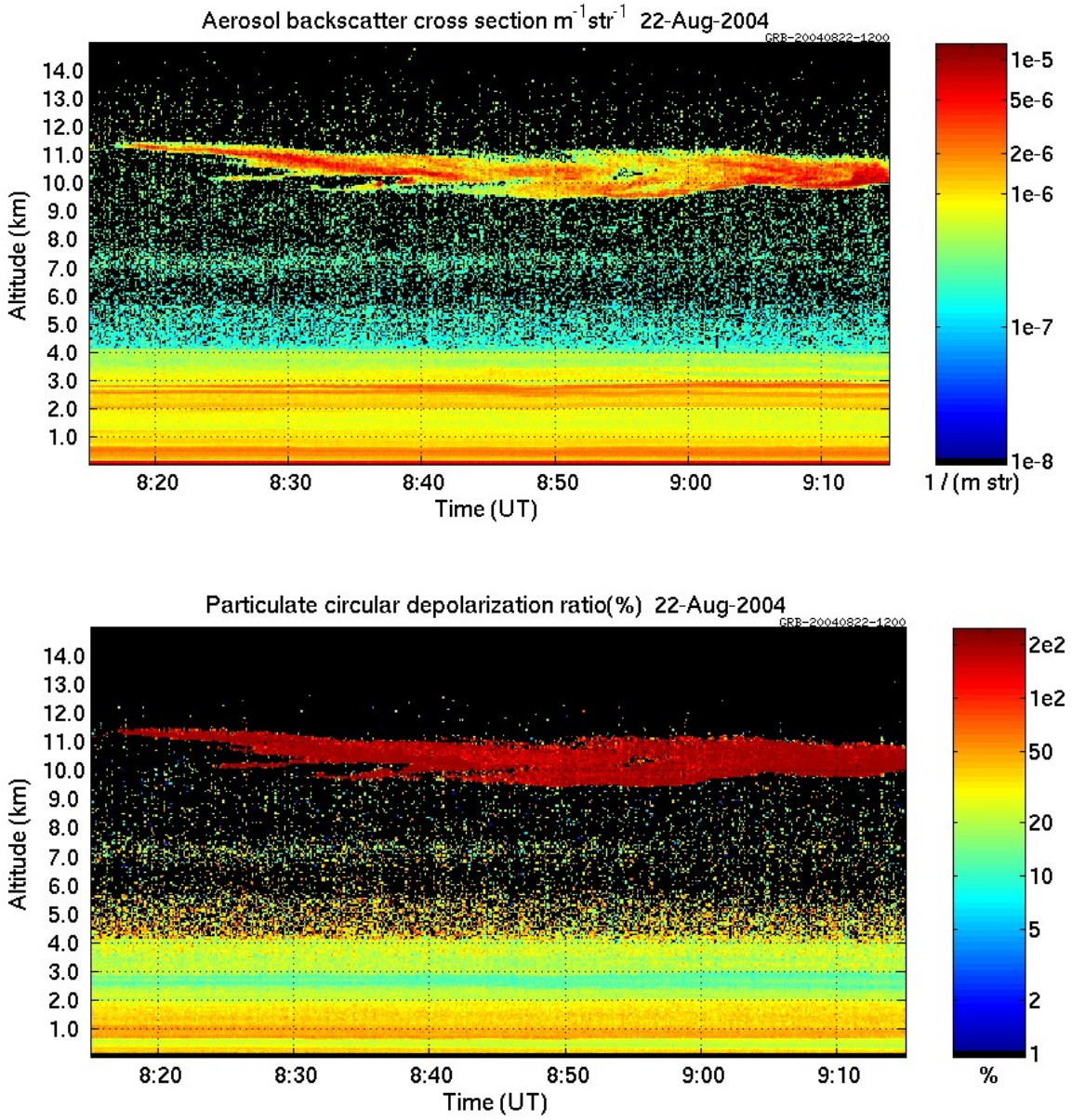

Figure 14 Top: AHSRL cloud and aerosol backscatter (top) and circular depolarization ratio (bottom) on August 22, 2004 over Madison WI between 0815 and 0905 UTC. The MODIS overpass at approximately 8:39 UTC indicated a clear scene. The total cloud/aerosol optical as measured by the AHSRL is approximately 0.2.

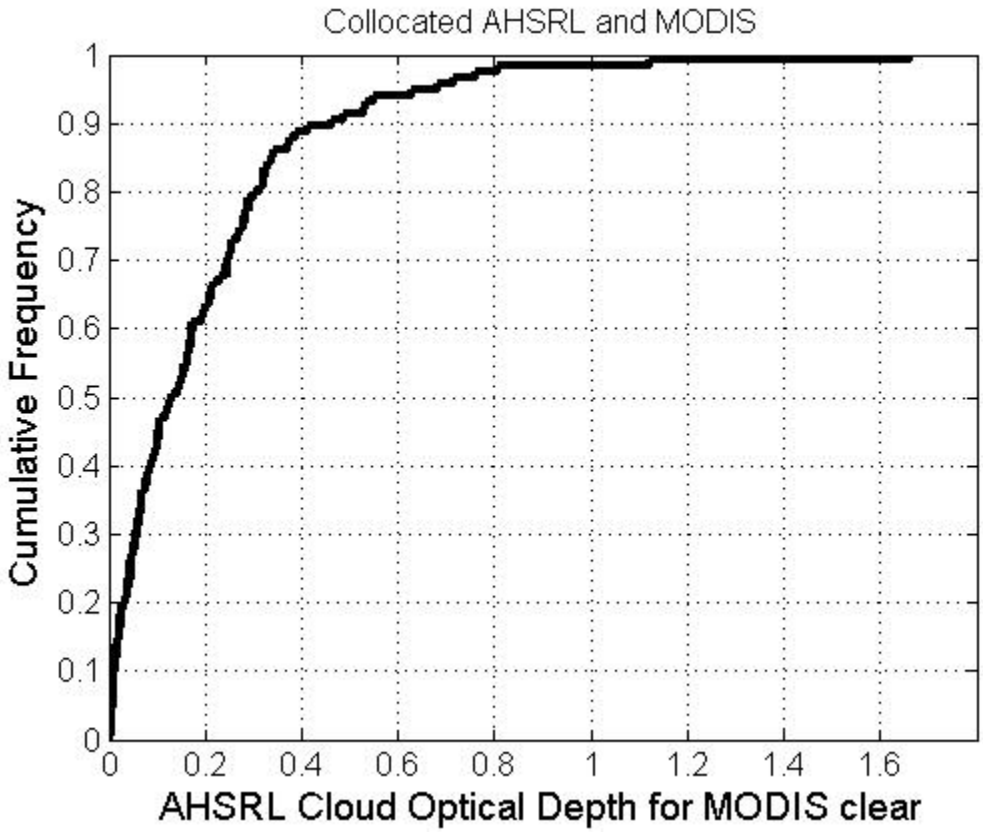

Figure 15 The cumulative frequency of optical depth when a MODIS pixel was identified as clear by the MODIS cloud mask algorithm but the AHSRL detected a cloud with a given cloud optical depth for both Terra and Aqua overpasses between January – August in Madison WI.

October 16 to November 18, 2003: MODIS Cloud Frequency

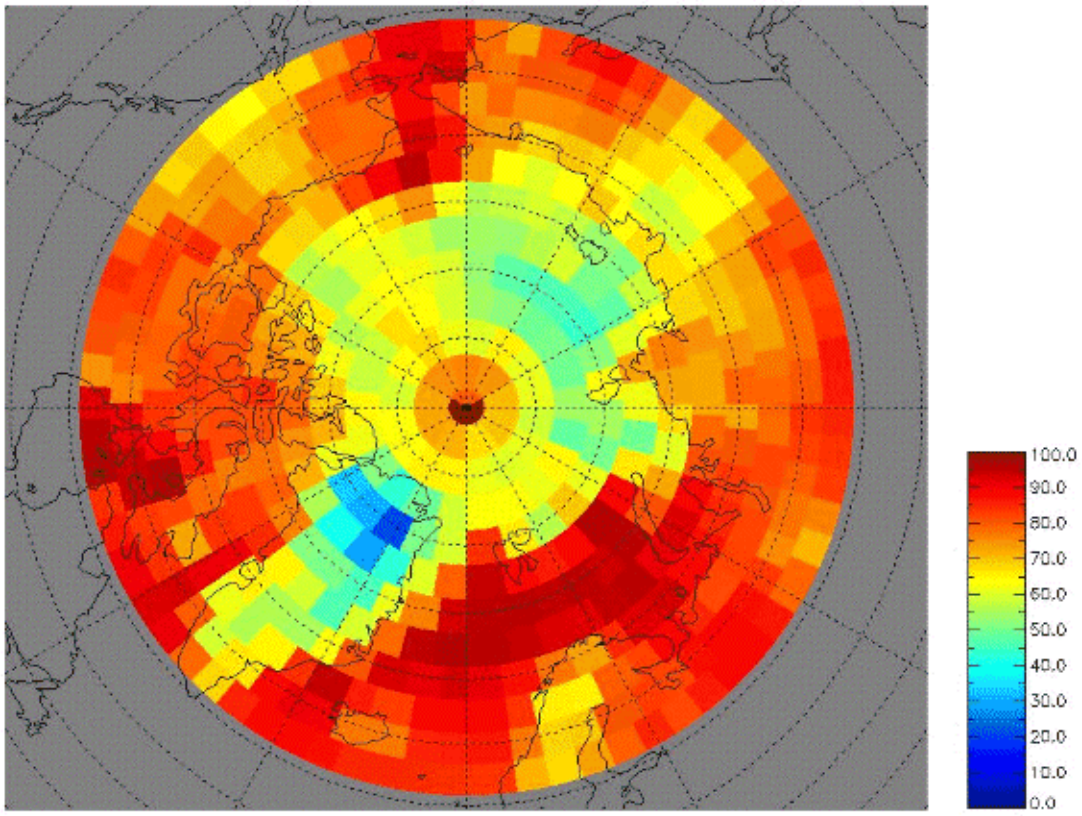

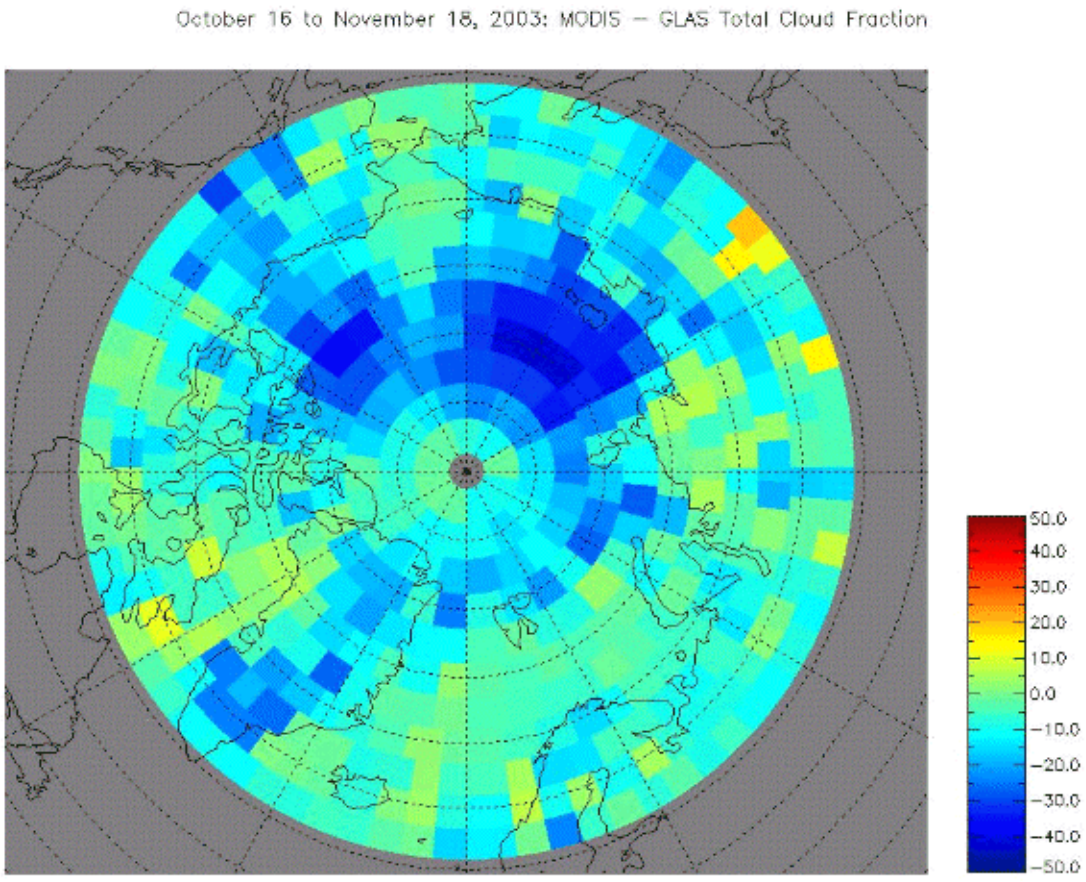

Figure 16 A) MODIS Terra Collection 5 cloud frequency from 60-90 N. B) MODIS minus GLAS cloud frequency. GLAS data product is the medium-resolution (one value per second) cloud frequency.

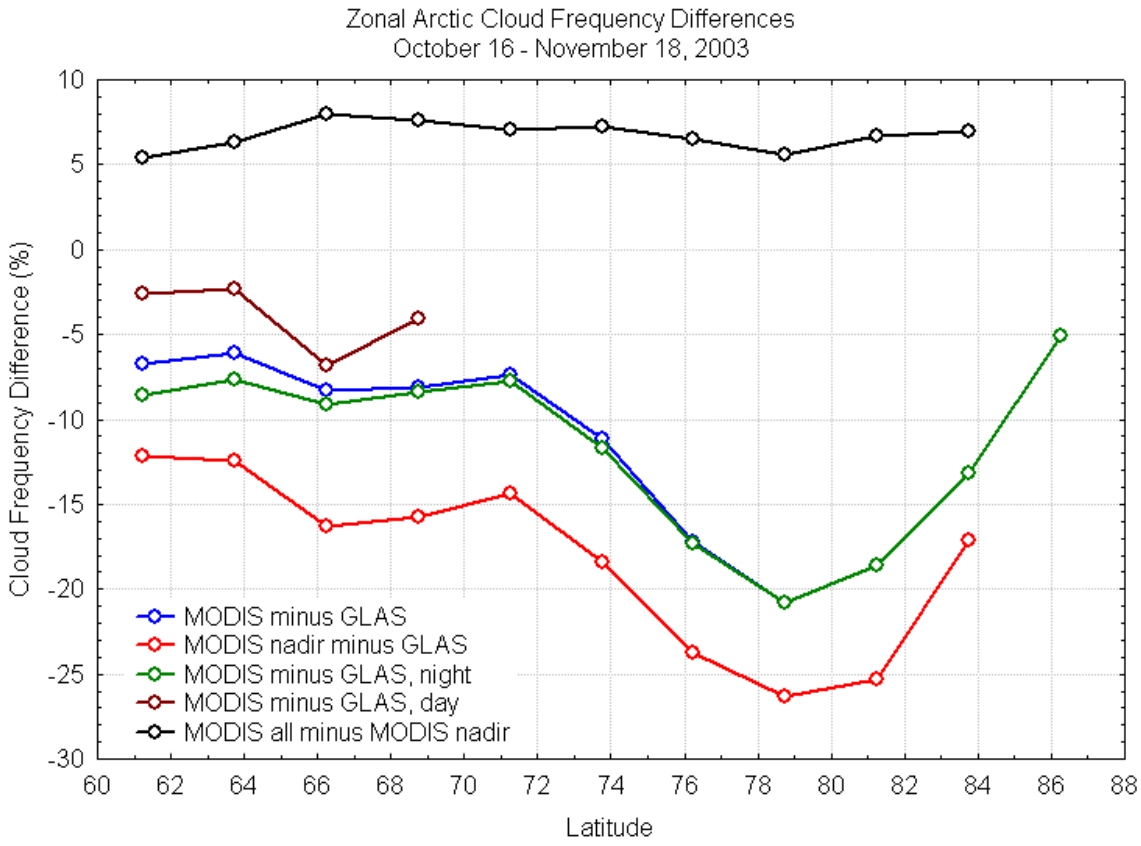

Figure 17 MODIS and GLAS cloud fraction differences. North of approximately 76 degrees latitude "all" and "night" categories are the same due to the season. Nadir MODIS data represents the 2 MODIS pixels near nadir, day and night combined.

Computationally Efficient Methods of Collocating Satellite, Aircraft, and Ground Observations

FREDERICK W. NAGLE AND ROBERT E. HOLZ

Space Science and Engineering Center, University of Wisconsin—Madison, Madison, Wisconsin

(Manuscript received 17 June 2008, in final form 20 October 2008)

ABSTRACT

The usefulness of measurements from satellite-borne instruments is enhanced if these measurements can be compared to measurements from other instruments mounted aboard the same or different satellite, with measurements from aircraft, or with ground measurements. *The process of associating measurements from disparate instruments and platforms is referred to as collocation.* In a few cases, two instruments mounted aboard the same spacecraft have been engineered to function in tandem, but commonly this is not the case. The collocation process may then become an awkward geometric problem of finding which of many observations within one dataset corresponds to an observation in another set, possibly from another platform. This paper presents methods that can be applied to a wide range of satellite, aircraft, and surface measurements that allow for efficient collocation with measurements having varying spatial and temporal sampling. Examples of applying the methods are presented that highlight the benefits of efficient collocation. This includes identifying the occurrence of simultaneous nadir observations (SNOs); collocation of sounder, imager, and active remotely sensed measurements on the NASA Earth Observation System (EOS); and collocation of the polar orbiting imager, sounder, and microwave measurements with geostationary observations. It is possible, using an inexpensive laptop computer, to collocate Moderate Resolution Imaging Spectroradiometer (MODIS) imager observations from the *Aqua* satellite with geostationary observations rapidly enough to deal with these measurements in real time, making either dataset, enhanced by the other, a potentially operational product. A ''tool kit'' is suggested consisting of computer procedures useful in collocation.

1. Introduction

For more than 40 yr, satellites have monitored the earth's weather and climate with significant advancements in the quality and scope of the observations. However, no single measurement provides the necessary information to characterize all relevant atmospheric properties. For this reason it is desirable to combine multiple measurements often on different satellites with diverse viewing geometries and sampling characteristics. This collocation process can be time consuming if the two instruments have not been engineered to function in tandem, as is often the case. This paper presents methods that allow a user to quickly find relevant observations within one set of data with matching or collocated data within another set from another instrument. The algorithms presented provide the capability to collocate two or more measurements, mounted aboard different spacecraft with different viewing geometries and temporal sampling.

The collocation methods can be applied to a wide variety of satellite and aircraft measurements including imager, infrared sounder, microwave, and active sensors. Recent applications include combined sounder and imager retrievals using collocated Atmospheric Infrared Sounder (AIRS) (Aumann et al. 2003) and Moderate Resolution Imaging Spectroradiometer (MODIS) (Justice et al. 1998) observations (Li et al. 2005), and global comparisons of cloud detection and height between the Cloud-Aerosol Lidar with Orthogonal Polarization (CALIOP) and MODIS (Holz et al. 2008). For these applications the multiple spacecraft and different spatial and temporal sampling required an efficient and accurate collocation provided by the collocation methods presented in this paper. Applications to aircraft measurements have facilitated comparisons between hyperspectral sounder, lidar, and imager retrievals (Holz et al. 2006). The methods can also be applied to collocate geostationary

Corresponding author address: Frederick W. Nagle, SSEC, 1225 W. Dayton Street, Madison, WI 53706.
E-mail: fredn@ssec.wisc.edu

DOI: 10.1175/2008JTECHA1189.1

and polar orbiting measurements and to determine simultaneous nadir observations (SNOs), and can be extended to the case in which one of the two or more instruments to be coutilized is mounted aboard an aircraft or ground station. This is accomplished by creating a fixed master field of view (FOV) with a radius corresponding to the sampling of the ground observation.

2. Navigation

a. Master and slave

We shall use the term *master* to denote the instrument onto whose footprint the observations of a second instrument, the *slave*, are to be projected. A typical example might be the collocation of AIRS and MODIS instruments, both carried aboard the *Aqua* spacecraft. The subsatellite diameter of the AIRS FOV is roughly 13 km, whereas the MODIS has a much higher spatial resolution, with more then 150 MODIS observations within a single AIRS quasi-oval. In this case, we consider AIRS to be the master, and MODIS the slave. As it happens, AIRS and MODIS are comounted aboard the same spacecraft, but in the following discussion no use is made of this fact. One might even envision a case of self-location in which the same instrument is both master and slave. For instance, one could seek a set of AIRS observations today and another set as nearly as possible over the very same set of geographical points a week later for the express purpose of observing the weekly variation.

b. Coordinate systems

Vector notation is used in much of what follows because of its facility in representing geometric relationships. The manner of implementing such relationships in a computer program is discussed presently. Vectors are indicated by bold roman type.

It is almost impossible to deal with satellite navigation without becoming involved in three different coordinate systems, as presented in Fig. 1. By the *celestial frame of reference* (CFR), which some may call an inertial system, we mean an orthonormal coordinate set, or basis, defined by three unit vectors, **I**, **J**, and **K** (which, respectively, lie along the x, y, and z axes in the figure), in which the **I** vector is directed from the center of the earth as origin toward the vernal equinox, an imaginary point in the sky defined as one of two intersections of the plane of the ecliptic with the plane of the equator. [The plane of the ecliptic would be seen to be the apparent annual path of the sun about the earth if the earth's daily rotation did not mask the sun's annual motion (see Smart 1977).] The **J** vector is 90° to the east of the **I** vector, in the plane of the equator. The **K** vector is directed from the center of the earth toward the North Pole. The *terrestrial frame of reference* (TFR) is similar in structure but with the **i** and **j** vectors fixed to the rotating earth, with **i** pointing from the earth's center toward the Greenwich meridian, **j** pointing to a longitude 90° east of Greenwich, and the **k** axis again pointing through the North Pole. Both these systems are dextral (right hand) orthonormal bases. The third system is the familiar latitude/longitude and central distance (LLD), that is, the distance from the earth's center to an object, with the caveat that we must be careful to distinguish between geodetic and geocentric latitude (see below). There is a fixed association between LLD and TFR, since they are both fixed to the earth. Time is not involved in this relationship.

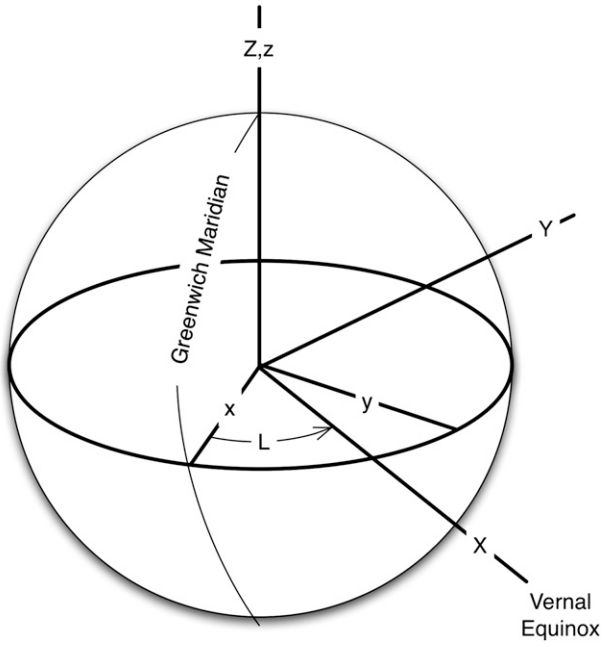

FIG. 1. The relationship between the celestial and terrestrial coordinate systems is presented. The origin of both the celestial and terrestrial systems is the center of the earth. The celestial X axis is directed toward the vernal equinox, with the Y axis 90° to the east. The x axis of the terrestrial system is directed toward the Greenwich meridian, and its y axis toward the meridian of 90°E. The Z and z axes of both bases pass through the North Pole.

However, the relation between the celestial and terrestrial bases is a function of time because of the apparent rotation of the vernal equinox about the earth once per sidereal day, and in fact this rotation defines the sidereal day. Montenbruck and Pfleger (2000) have provided an algorithm for computing the longitude of the vernal equinox as a function of time, which in turn allows simple interconversion between celestial and

terrestrial coordinates. With this longitude known, the reader can think of the transformation of a vector from the TFR to the CFR as

$$V_C = \begin{vmatrix} \cos(L) & \sin(L) & 0 \\ -\sin(L) & \cos(L) & 0 \\ 0 & 0 & 1 \end{vmatrix} V_T \qquad (1a)$$

and the inverse as

$$V_T = \begin{vmatrix} \cos(L) & -\sin(L) & 0 \\ \sin(L) & \cos(L) & 0 \\ 0 & 0 & 1 \end{vmatrix} V_C, \qquad (1b)$$

where L is the instantaneous longitude of the vernal equinox and hence a function of time. These matrices are orthogonal, implying that their inverses are also their transposes. Aitken (1956) discusses orthogonal matrices.

Many polar orbiting weather satellites are sun synchronous, and hence they pass over a given region at roughly the same local time each day. Given the apparent annual revolution of the sun about the earth, the right ascension of the ascending node of such satellites (the celestial point where they cross the equator flying north), measured in degrees, must increase about 360/365.25, or roughly 1°, per day. Since such satellites typically make about 14 orbits per day, the instantaneous plane of the satellite's motion precesses about 1/14 of a degree per orbit in celestial space. This fact permits a simplification in estimating satellite positions in the absence of a formal prediction model. With negligible (and easily corrected) error we can speak of the *orbital plane* of a sun-synchronous orbit over a limited time (e.g., 25 min) in the CFR. The rotation of the earth beneath the satellite invalidates a similar assumption in the TFR, and the subsatellite track traced onto the rotating earth departs markedly from a great circle.

Satellite navigation uncertainties arise from failures to discriminate carefully between geodetic and geocentric latitude. The earth-located coordinates of datasets are usually rendered in geodetic latitude, while satellite navigation software typically returns its results in geocentric. For a discussion of geodetic and geocentric latitude, see Bowditch (1977). For the earth model used by the authors, the equation

$$b^2 \tan(d) = \tan(c)$$

can be used to interconvert between geodetic and geocentric latitude, where d is geodetic, c is geocentric, and $b = 6\,356\,911.946/6\,378\,388$, the ratio of polar to equatorial radius.

c. Forward and inverse navigation

It is no surprise that the collocation of satellite observations requires the ability to specify the location of a satellite as a function of time. We refer to this computation as *forward navigation*. It is equally important to employ some technique of *inverse navigation,* by which we mean determining the time when a satellite is over or abeam of a given point on the surface. Inverse navigation may not always be needed (e.g., in the case when master and slave are mounted aboard the same spacecraft, so that the times of the observations are the same or nearly so). However, if the instruments are mounted aboard different spacecraft, then we must know the time when the slave satellite is in a position to observe the master field of view. This problem is straightforward if the slave instrument is a cross-scanner, for example, MODIS, AIRS, etc., but can become a bit awkward otherwise, as with a conical scanner.

Satellite forward navigation software is available from sundry sources, but the authors developed the inverse navigation software. For reasons of policy or convenience, one may decide to use only the satellite positioning data contained within the data files delivered to the investigator from the source agency [i.e., National Aeronautics and Space Administration (NASA), National Oceanic and Atmospheric Administration (NOAA), etc.], without recourse to formal navigation routines that would also demand the availability of concurrent orbital parameters. (However, if orbital parameters are wanted, the user can visit the Web site celestrak.com.) The satellite orbital location at the time of an observation is not always provided in the data files. For these cases, the satellite location must then be approximately inferred from the distribution of the geolocated FOVs. Knowledge of the master satellite's location at an observation time need not always be known to extreme accuracy. The reason for wanting the satellite's approximate position is to provide an estimate of the size, orientation, and elongation, or eccentricity, of a quasi-ellipsoidal master FOV as it is projected onto the surface at a high scan angle. Often we assume that a satellite's spatial attitude is nominal, so that it views its own nadir when the instrument scan angle is zero, and for this case the position of the satellite is taken to be the zenith of the center point of a scan at a known or presumed altitude. If the satellite exhibits a known pitch, roll, or yaw, the needed correction is not difficult. For this case the most difficult component to estimate is the satellite's altitude if it is not provided with the observations. It has been found, at least in the case of a cross-scanning instrument like MODIS or AIRS, that the altitude can be computed to

an accuracy of about 0.05 km by examining the locations of the FOVs along a scan line, and driving the projection geometry backward to infer the satellite's altitude (i.e., triangulating on the satellite from various earth locations). This scheme presupposes that the satellite's attitude is nominal or nearly so.

INVERSE NAVIGATION

Inverse navigation is a major portion of collocation. If we can estimate closely the time at which a slave satellite passes abeam of a master FOV on the surface, we have greatly restricted the amount of slave data that must be searched to find collocations.

Let a satellite's position at a given moment be expressed by the vector $\mathbf{S}(t)$, and its velocity by $\mathbf{V}(t)$ as presented in Fig. 2. The satellite's angular momentum vector $\mathbf{A}$, which is normal to the quasi plane of the orbit in celestial space, is given by $\mathbf{A} = \mathbf{S} \times \mathbf{V}$; $\mathbf{A}$ can also be thought of as the vector orbital plane, since knowledge of $\mathbf{A}$ defines the orientation of the orbital plane in the CFR. As noted, the direction of $\mathbf{A}$, which is all that interests us, is almost invariant over a brief period (i.e., 25 min or a quarter-orbit). Let $\mathbf{G}(t)$ be the position vector of an arbitrary point on the ground in the CFR. It is a function of time in celestial space because of the earth's rotation.

Let $\mathbf{R}(t) = [\mathbf{G}(t) - \mathbf{S}(t)]$ at time t denote the slant vector from the satellite to this ground point. We seek to know when the satellite is over or abeam of this point, that is, when $\mathbf{G}$ lies in the plane containing both $\mathbf{S}$ and $\mathbf{A}$, or equivalently, when the cross product $\mathbf{S} \times \mathbf{R}$ has no component along the vector angular momentum $\mathbf{A}$. This condition is fulfilled when the triple scalar product P vanishes, that is,

$$P = \mathbf{S}(t) \times \mathbf{R}(t) \cdot \mathbf{A} = 0. \quad (2)$$

Equation (2) is the governing equation for inverse navigation. We can solve the inverse navigation problem if we have any scheme for finding the value of t that makes Eq. (2) a true statement.

If approximating polynomials are used to estimate the satellite's position and velocity (see below), and because the rate of the earth's rotation is a known constant, then (2) can be formally differentiated to find dP/dt, and a Newton–Raphson iteration used to seek the value of time t that satisfies (2):

$$t(1) = t(0) - P[t(0)]/(dP/dt). \quad (3)$$

If we have no approximating polynomials, but possess only a full-scale forward navigation model for obtaining $\mathbf{S}$ and $\mathbf{V}$, then formal differentiation of (2) is not feasible and we then begin with some initial guess for $t(0)$, and use finite differences in consecutive iterations of the value of P to approximate the rate of change of P with respect to t. Note that a Newton–Raphson approximation as expressed by (3) displays geometric convergence, meaning that with each iteration we roughly double the number of correct digits, so that convergence is rapid.

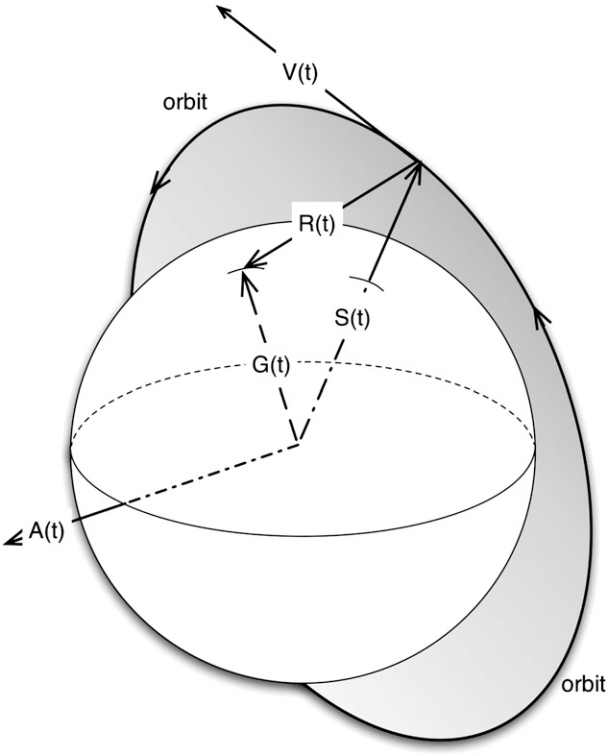

FIG. 2. Computing the moment when a slave satellite views the master FOV: $\mathbf{S}(t)$ is the position of an orbiting satellite; $\mathbf{V}(t)$ is its vector velocity; $\mathbf{A}(t) = \mathbf{S} \times \mathbf{V}$ is the angular momentum vector, or the vector orbital plane; and $\mathbf{R}(t)$ is a slant range from the satellite to a point on the ground. The satellite is abeam of this point when the triple scalar product $\mathbf{S} \times \mathbf{R} \cdot \mathbf{A} = 0$.

To create a ''quick-and-dirty'' navigation model that lends itself either to forward or inverse navigation, we can proceed as follows: We compute four satellite positions in the celestial system (the earliest, the latest, and two intermediate points) based on the scan line centers from our dataset, encompassing not more than 25 min, by converting the four earth locations to celestial coordinates and projecting them upward to a computed or nominal altitude. We can make this conversion using the transform in Eq. (1a), assuming the times of these four earth locations are provided with the data. Let these four celestial positions be $\mathbf{V}_i$, where $i = 1, 4$. We can then create two cubic polynomials, shown in nested form:

$$D(t) = a_0 + t[a_1 + t(a_2 + a_3 t)],$$

$$C(t) = c_0 + t[c_1 + t(c_2 + c_3 t)].$$

Here $D(t)$ is the angular displacement in the orbital plane from the initial position $\mathbf{S}_0$, and $C(t)$ is the central distance of the satellite as presented in Fig. 3. Let $\mathbf{R}(\mathbf{S}, \mathbf{A}, x)$ be an operator that rotates vector $\mathbf{S}$ clockwise about $\mathbf{A}$ in the amount of x degrees. In Fig. 3 the satellite's vector orbital plane, or angular momentum vector, is given by the cross (vector) product $\mathbf{A} = \mathbf{S} \times \mathbf{V}$, and points out of the paper toward the reader. Further, let $\mathbf{U}$ be a unitizing or normalizing operator that reduces its vector argument to a unit vector. Since $D(t)$ and $C(t)$ are differentiable functions of time, we can use their derivatives to find the velocity $\mathbf{V}$ at a given moment. The desired satellite position at an arbitrary time is given by

$$\mathbf{S}(t) = C(t)\mathbf{U}\{\mathbf{R}[\mathbf{S}_0, \mathbf{A}, -D(t)]\}. \quad (4)$$

This approximation of the satellite's position involves little more than evaluating the two polynomials, and since these polynomials are easily differentiated, we effectively have an inverse navigation model using a Newton–Raphson inverse solution for t, given $\mathbf{S}(t)$.

An alternate scheme, instead of using a subset of points chosen from the dataset, is to use *all* satellite locations derived from the subsatellite data track and then to compute a least squares cubic or quadratic fit as a function of time for both the angular displacement along the track and the radius vector of the satellite.

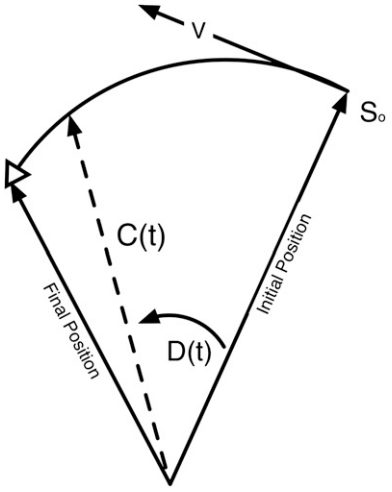

FIG. 3. Given an initial satellite position $\mathbf{S}_0$ in the plane of the satellite's motion in the CFR, and final position some minutes later, we can express an intermediate displacement $D(t)$ by a cubic polynomial based on the initial, final, and two intermediate positions. The central distance $C(t)$ is likewise expressed by a cubic polynomial.

3. Simultaneous nadir observations

The term *simultaneous nadir observation* (SNO) is something of a misnomer, because it rarely happens that two satellites will pass over any point on the ground at precisely the same moment. In using this term, we mean only ascertaining within some acceptable time window for example, 15 min, when and where two satellites will pass over a common point on the earth's surface. The SNOs thus identified may be scattered in a seemingly random manner over the earth, or if the orbits have nearly identical periods, the SNO points may be confined to restricted latitude bands in both the Northern and Southern Hemispheres. Satellites with slightly differing orbital periods will experience numerous SNOs for a period of time, and then, like two clocks ticking in the same room at slightly different rates, they will pass through a prolonged period of many weeks during which there are no SNOs within the stated time window. The choice of time window is a scientific judgment dictated by the perishability or timeliness of data that are not coincident in time with other data.

Ascertaining the occurrence of SNOs for a given pair of satellites is actually rather rapid. For this purpose we need a fairly general orbital prediction model (OPM), as well as a general inverse navigation algorithm, and orbital parameters for a time period covering the period of interest, say several months to a year. Again, we use the convenient fact that the orbital plane of a sun-synchronous satellite has an almost constant orientation in the CFR over a time span of a single orbit, that is, its motion is essentially planar over a limited time span.

Let us choose two satellites, satellite 1 and satellite 2, and select an arbitrary initial time t_0. At this time we obtain the position $\mathbf{S}$ and velocity $\mathbf{V}$ of both satellites, and from these we obtain their two vector orbital planes (or angular momentum vectors),

$$\mathbf{A}_i = \mathbf{S}_i \times \mathbf{V}_i = 1, 2.$$

Refer to Fig. 4. In celestial coordinates, two possible SNO points will lie along the intersection of the two orbital planes, that is, they will lie on the vector cross product $\mathbf{P} = \mathbf{A}_1 \times \mathbf{A}_2$ and on diametrically opposite sides of the earth in the CFR. This expression for $\mathbf{P}$ presupposes that the two orbital planes are not nearly coincident as in the cases, say, of Cloud-Aerosol Lidar and Infrared Pathfinder Satellite Observation (CALIPSO) and *Aqua*, for in such cases the angle between the two planes is so small that the cross product $\mathbf{A}_1 \times \mathbf{A}_2$ is ill defined.

Let us select one of the two possible SNO points, say the one most closely following time t_0. Let us call this point P in Fig. 5. The angular speed of a satellite is only slightly variable, about 3.66° min^{-1} for most of the

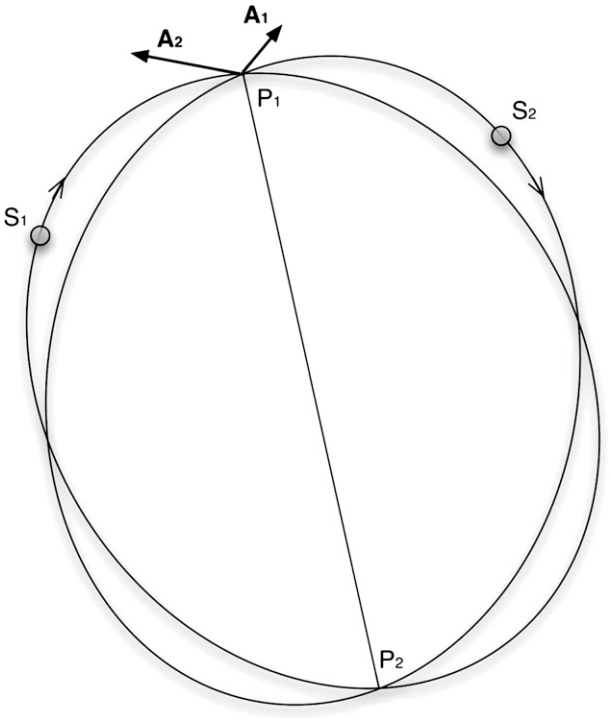

FIG. 4. In celestial coordinates two nonparallel orbits will intersect at a point lying along the dihedral intersections of their orbital planes, that is, along the vector cross product $\mathbf{A}_1 \times \mathbf{A}_2$. The respective satellites are S_1 and S_2.

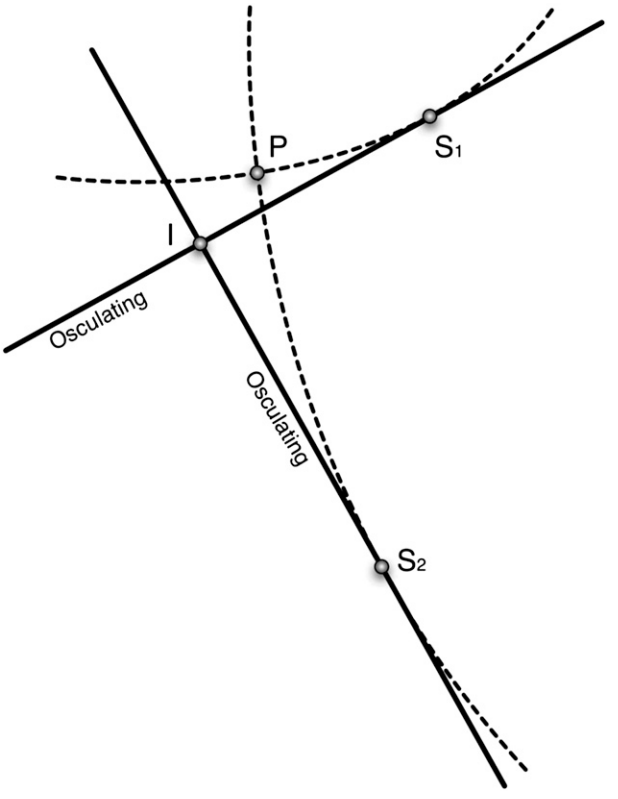

FIG. 5. Two satellites are initially at points S_1 and S_2, and will later fly over point P, which we seek to identify. A first estimate of point P is point I, defined as the cross product of the two osculating plane vectors calculated at an initial time. The procedure can then be iterated to improve our estimate of P.

satellites of interest, so that we can compute the time t_1 of the arrival of satellite 1 at P by some scheme of successive approximation. In like manner we find the time t_2 of arrival of satellite 2 at this point. From our orbital model we also know the velocity of each satellite at point P. Keep in mind that P is defined in celestial coordinates, not terrestrial. If the difference $|t_1 - t_2|$ is greater than the acceptable time window, we discard this case and advance the time t_0 by about 50 min, or half an orbit, and repeat the process.

But assume the satellites both reach point P within a suitable time interval of each other. We seek to learn the unique point on the earth's surface over which both satellites will pass, though in general not at precisely the same moment. For each satellite we convert its position and velocity at its arrival time t_i to the TFR, using the relation (1b). Since the satellites in general will not arrive at the celestial point P at the same moment, the subsatellite points on the earth beneath P at t_1 and t_2 will be slightly different, owing to the rotation of the earth during the interval between t_1 and t_2. Transforming a satellite's position to terrestrial coordinates is straightforward, but in converting velocity we face the complication that the satellite's apparent velocity over the earth is altered by the eastward rotation of the earth, so that as seen by an earth-bound observer the subsatellite track has a westward component equal to the eastward speed of a point of the earth at its given latitude H. In other words, the satellite's apparent velocity vector is

$$\mathbf{V_A} = \mathbf{V}_t + E\cos(H)\mathbf{W}, \tag{5}$$

where $\mathbf{V_A}$ is the apparent velocity over the earth, $\mathbf{V}_t$ is the celestial velocity converted to the terrestrial frame [based simply on (1b) and unadjusted for the speed of the rotating earth], $\mathbf{W}$ is a unit vector pointing toward local west at the given ground point, and E is the eastward speed of rotation of the earth at the equator. At time t_i, we can regard the velocity over the ground as described by $\mathbf{V_A}$ as lying in the *osculating* plane of the satellite's motion as seen by an earth-bound observer. The orientation of this osculating plane is defined by expressing it as the cross product

$$\mathbf{O}_i = \mathbf{S}(t_i) \times \mathbf{V_A}_i$$

for each satellite. The intersection of the two osculating planes, one for each satellite, represents an approximate

point in the TFR on the earth's surface over which the satellites will fly at times t_1 and t_2, respectively. This intersection **I** of the two osculating planes is found from

$$\mathbf{I} = (\mathbf{S}_1 \times \mathbf{V}_{\mathbf{A}1}) \times (\mathbf{S}_2 \times \mathbf{V}_{\mathbf{A}2}),$$

where $\mathbf{V}_{\mathbf{A}1}$ and $\mathbf{V}_{\mathbf{A}2}$ are found from (5) for each satellite, and the vector **I** is an approximate point on the earth overflown by both satellites. Using the inverse navigation scheme mentioned above, that is, solving (2) for t, we compute for each satellite new values of t_1 and t_2, the times when they are over or abeam of **I**, and repeat the process described above, this time with more accurate values of t_1 and t_2. That is, at the new times t_1 and t_2 we compute new satellite positions, convert these to a terrestrial frame, recompute osculating planes, obtain an improved value of **I**, etc., until the changes in **I** from one iteration to another fall below some threshold. Three iterations of this procedure are quite adequate.

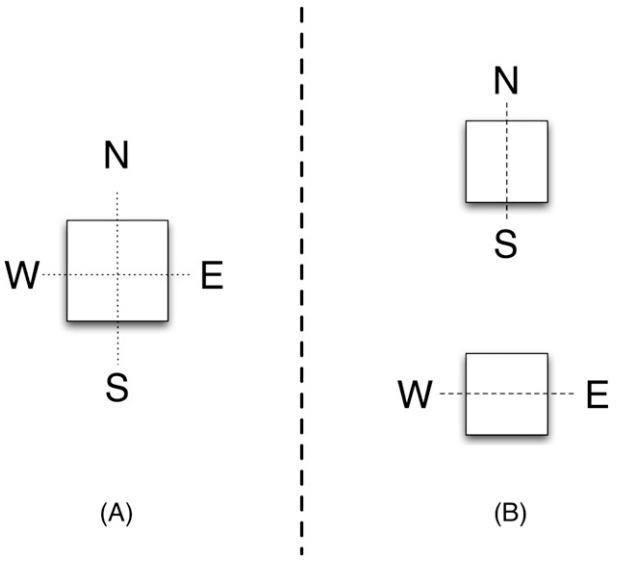

FIG. 6. The geometry of intersecting line segments is presented. (a) An example of intersection and (b) a nonintersecting geometry. A line connecting two partners is analogous to a data swath on the surface of the earth.

4. Intersecting data swaths

To hasten the collocation process, it is desirable to know if two data swaths intersect at all. For instance, the nadir-viewing lidar instrument aboard the CALIPSO traces a data swath along the subsatellite track. It may or may not intersect a data swath created by the cross-scanning MODIS instrument carried aboard *Aqua*. Plotting the swaths on a map would show instantly that they do or do not intersect, but what is a convenient way of determining this analytically?

Imagine two couples playing bridge, seated around a table, with east facing west and north facing south. Let their vector positions be **E**, **W**, **N**, and **S** as presented in Fig. 6a. The position of the origin is arbitrary. East sees north on his right and south on his left. East turns his head to the right to look at north, then leftward to look at west, and still more to the left to look at south. In vector terms the scalar product

$$(\mathbf{N}-\mathbf{E}) \times (\mathbf{W}-\mathbf{E}) \cdot (\mathbf{W}-\mathbf{E}) \times (\mathbf{S}-\mathbf{E}) > 0. \qquad (6a)$$

Both cross products in (6a), by the customary right-hand rule of vector algebra, are directed upward toward the ceiling, and hence their scalar product is positive. By the same token,

$$(\mathbf{E}-\mathbf{S}) \times (\mathbf{N}-\mathbf{S}) \cdot (\mathbf{N}-\mathbf{S}) \times (\mathbf{W}-\mathbf{S}) > 0, \qquad (6b)$$

and because both (6a) and (6b) are positive, the segment connecting east and west intersects the segment connecting north and south at the center of the table.

After the game the couples go to lunch, and sit at different tables (Fig. 6b). In such a case, there will be no intersection because at least one player will see both his opponents on his left or both on his right.

In the case of data swaths, let the latitude/longitude of the end points of swath A and swath B be converted to terrestrial vectors (see the tool kit below). Then the beginning and end points of swath B can be viewed analogously with east and west, and the end points of swath A with north and south. In analogy with the bridge partners, the swaths intersect if the two scalar products are both positive:

$$(\mathbf{B}_1-\mathbf{A}_1) \times (\mathbf{A}_2-\mathbf{A}_1) \cdot (\mathbf{A}_2-\mathbf{A}_1) \times (\mathbf{B}_2-\mathbf{A}_1) > 0$$

$$(\mathbf{A}_2-\mathbf{B}_1) \times (\mathbf{B}_2-\mathbf{B}_1) \cdot (\mathbf{B}_2-\mathbf{B}_1) \times (\mathbf{A}_1-\mathbf{B}_1) > 0.$$

5. Detecting overlap

In some approaches to collocation, an investigator is satisfied to know merely if a slave observation does or does not overlie a master oval. For example, the template approach suggested by Aoki (1980) produces a yes/no response to this question. However, in the case of most sounders, the instrument spatial response function is strongly dependent on the distance from the center of the FOV. Often the half-power distance from the center is used arbitrarily to define the radius at nadir. In such a case, an investigator may prefer to assign a lesser weight to an overlying slave observation that falls near the circumference of a master oval and greater weight near

the center. The techniques described in this article determine not only if a slave observation falls within a selected master oval, but also assign a linear weight to each slave observation, varying from one at the center to zero at the edge. A user can choose to use only those slave observations whose weights exceed some threshold or apply the weighting to a predetermined spatial response function.

a. The quasi-elliptical approach

If a satellite-borne earth-observing scanning instrument has a circular field of view when aimed at a point directly beneath the satellite, the fields of view become egg-shaped, or oviform, as the scan moves away from nadir. The FOVs are not exactly elliptical, owing to the fact that a perceptible curvature of the earth exists even within a small FOV. However, the approximation to an ellipse is often so close that the FOV may be regarded as quasi-elliptical for purposes of collocation, provided the scan is not close to the limb of the earth, where the FOV ceases to be even quasi-elliptical. The quasi-elliptical assumption is more valid the smaller the FOV. It is not difficult to compute the size, orientation, and eccentricity of a quasi-elliptical FOV. See Fig. 7a.

In the following, we assume that a master FOV is not at the master satellite's nadir. If we let **F** be the vector position of the nominal center of the master FOV, computable from its latitude, longitude, and earth radius, and **S** the vector position of the satellite, then the slant range vector, earth to satellite, is the vector difference $\mathbf{R} = \mathbf{S} - \mathbf{F}$. The vector or cross product $\mathbf{F} \times \mathbf{R}$ is oriented along the minor axis, and its length is the diameter of the FOV at nadir multiplied by the ratio of slant range to satellite altitude. We use the vertical bars | | to denote the scalar magnitude of a vector, and **U** to be a unitizing or normalizing operator that produces a unit vector in the direction of its argument:

$$\mathbf{B} = |\mathbf{R}|\mathbf{U}(\mathbf{F} \times \mathbf{R})/z,$$

where z is the altitude of the satellite, the scalar D is the diameter of the FOV at nadir, and **B** is the vector minor axis. Figure 7b enlarges the quasi-elliptical field of view. The major axis **A** is of course normal to both **B** and **F**, and hence its direction is given by their cross-product $\mathbf{B} \times \mathbf{F}$. If **A** is thus computed, it will point in the general direction of the subsatellite point. The length of the major axis equals the length of the minor axis, multiplied by the secant of the satellite zenith angle as seen at the FOV. Let us introduce the vertical caret ^ to denote the unsigned angle in degrees between two vectors. Then

$$\mathbf{A} = \mathbf{U}(\mathbf{F} \times \mathbf{B})|\mathbf{B}| \,\text{secant}(\mathbf{F}\text{^}\mathbf{R}).$$

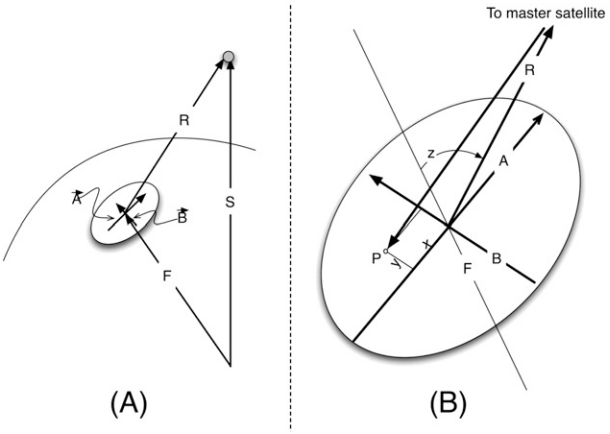

FIG. 7. The geometry of determining whether a slave point (P) does or does not fall within a master FOV. (b) An enlargement of the (a) quasi-elliptical FOV. The x and y coordinates of a slave observation within the master FOV lie along the major and minor axes of the master FOV. The axes are computed as described in the text.

The angle **F**^**R**, indicated as z in Fig. 7b, is the zenith angle of the satellite seen from the FOV. The eccentricity of the quasi-elliptical oval, if it is wanted, is implied by the values of the major and minor axes |**A**| and |**B**|, respectively.

We have now defined the quasi ellipse on the earth's surface of the master observation. Again let the vector **F** represent the terrestrial position vector of the center of the master quasi ellipse. Assume we are given the coordinates of a slave observation from which we are to decide if the slave does or does not fall within the master, and if so with what weight. First, we convert the coordinates of the slave observation to a terrestrial vector **P**. See Fig. 7b. We define the x coordinate of the slave observation as the component of its displacement along the major axis and the y component along the minor axis:

$$x = \mathbf{U}(\mathbf{A}) \cdot (\mathbf{P} - \mathbf{F})$$

$$y = \mathbf{U}(\mathbf{B}) \cdot (\mathbf{P} - \mathbf{F}),$$

where the dot · denotes the dot or scalar product of two vectors. If the distance D given by $|\mathbf{P} - \mathbf{F}|$ is less than the semiminor axis, the slave spot falls within the master FOV. If it is greater than the semimajor axis, it falls outside the master FOV. In the intermediate ambiguous case, the slave spots falls outside if $y^2 > b^2(1 - x^2/a^2)$. Letting $a = |\mathbf{A}|/2$ and $b = |\mathbf{B}|/2$, the semimajor and semiminor axes, the weight assigned to an overlapping slave observation is

$$w = 1 - (x^2 + y^2)/[x^2 + b^2(1 - x^2/a^2)].$$

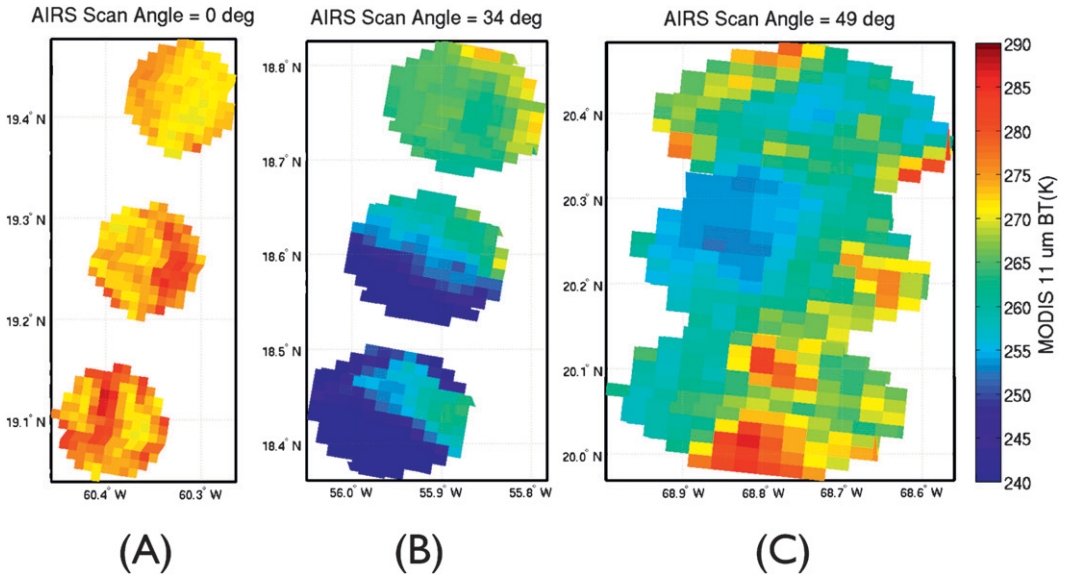

FIG. 8. An example of applying the collocation to an imager (MODIS) and infrared sounder (AIRS) measurements is presented for three different AIRS scan angles. The images present the collocation applied to the MODIS 1-km-resolution 11-μm BT measurements.

This represents a linear weighting from zero at the edge of the FOV and one at the center.

Figure 7 is somewhat misleading in that it suggests that the slave instrument, whose FOV is the point P, is mounted on the same satellite as the master. This condition, however, is not a requirement.

As a means of verifying the accuracy of collocated slave points, it is a simple matter to compute the angular distance between the centroid of the slave points within the master FOV, and the center of the master FOV. This centroidal distance should typically equal a small fraction of a kilometer. The centroid is found from the sum of the overlapping vector slave positions. This method is sufficiently rapid to allow for collocation in real time of geostationary and polar orbiting imager measurements.

The quasi-elliptical approach applied to MODIS 1-km-resolution imager measurements with AIRS is presented in Fig. 8 for a nadir, 34°, and 49° AIRS scan angles. The figure presents the MODIS 11-μm brightness temperature (BT) measurements found to be collocated within each AIRS FOV. Notice that as the AIRS scan angle increases, the projected AIRS FOV becomes increasingly more quasi-elliptical at large scan angles. Using this methodology, AIRS retrievals of temperature and water vapor within partially cloudy FOV have been improved by integrating the MODIS cloud mask using the collocation (Li et al. 2005).

b. *Quasi-conical approach*

Another approach may be easier than the quasi-elliptical method, especially if both master and slave instruments are mounted aboard the same spacecraft. It avoids any exercise in analytic geometry involved in determining whether a slave observation falls within a master oval on the surface (see Fig. 9).

Let us make the assumption, not always strictly correct, that the master instrument views the underlying earth as if through a cone whose angular opening is determined by the size of the master FOV when seen at nadir, with the apex of the cone at the satellite. Then any slave observation viewed within the solid angle of the cone overlaps the master FOV on the ground. We need not concern ourselves with the size, shape, or orientation of the master FOV on the surface. Let A be the angular half-width of the master FOV, $\mathbf{S}$ the vector position of the satellite, and $\mathbf{F}$ and $\mathbf{E}$ be the surface vector positions of a master and slave FOV, respectively. Then if

$$(\mathbf{F} - \mathbf{S})\hat{}(\mathbf{E} - \mathbf{S}) < A,$$

the master FOV is overlapped by the slave observation, that is, if the angular difference between the satellite-to-ground slant ranges is less than the half-aperture of the master FOV. If desired, a weight can be assigned to an overlapping slave observation by the amount of the angular difference. If the difference is zero, then we assign a weight of one. If the angular difference of the master and slave slant ranges is at the angular limit A, then we would assign a weight of zero.

The quasi-conical approach suffers from the drawback that computing a small angle between two nearly parallel vectors demands an accurate arccosine routine,

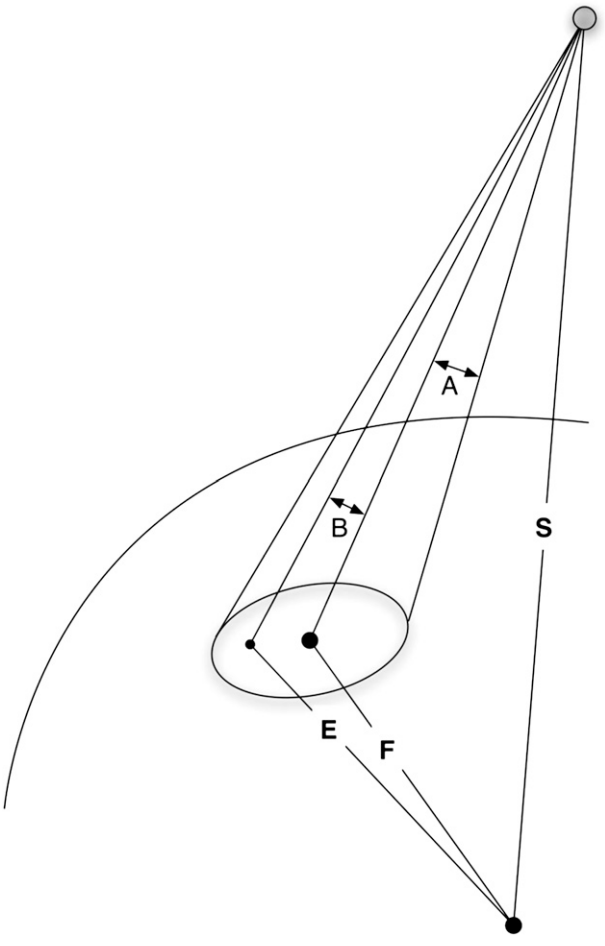

FIG. 9. A conical FOV at the satellite projects into a quasi ellipse on the surface. A slave observation with position vector **E** lies within the master FOV, whose center is given by the vector **F**, if the angle B between the slant vectors **F–S** and **E–S** is less than the FOV angular radius *A*.

given that the cosine function has a zero derivative when its argument is zero, so that the inverse function is ill defined. This problem is amplified for the case when one satellite is geostationary, with a very high altitude, and in such a case the quasi-elliptical approach is not recommended.

6. General procedure

Let us sketch a sequence of events in collocating a set of MODIS slave points (imager) over an AIRS (sounder) FOV. In this example the slave instrument is a cross-scanning instrument.

1) We are given an arbitrary master FOV. The diameter or radius of this FOV at nadir is known, for example, from the half-power point of the signal. Using an inverse navigation scheme such as described above, we estimate the time at which the satellite carrying the slave instrument is over or abeam of the master FOV. The slave-carrying satellite may or may not be the same as the master-carrying satellite.
2) Knowing the approximate time of transit (i.e., time over or abeam), we now know the approximate row or rows of the slave observations that are likely to overlie the master FOV, since each slave observation has an associated time, and shall confine our search to these rows. It may be adequate initially to inspect all the slave observations in the row for possible overlap, but on subsequent passes we shall already know approximately which points along the slave scan line will overlap.
3) Using one of the overlap-detecting schemes outlined above, we identify those slave observations, and assign weights to them, that overlap the given master FOV. The indices of these slave observations (row and spot indices) are then recorded.
4) Another master FOV is selected, and if it is contiguous to the previously chosen master FOV, we already know the general location of the slave observations that are likely to overlap it, thus hastening our search.

The time of an observation may be provided to an investigator in a variety of ways. The authors have often been given time as the number of seconds elapsed since some epoch, usually 0000 UTC 1 January 1993, including intercalated leap seconds. Conversion to the civil calendar and coordinated universal time is straightforward, with each day consisting of 86 400 s, but with adjustment for the intervening leap seconds.

The authors use a flat time field (i.e., free of years, months, days, hours, leap years) based on the Julian day number (JDN), which is itself defined as the number of mean solar days elapsed since 1 January 4713 BCE. This is a large number in the modern era, being 2454101 on 1 January 2007, and for this reason the authors use a modified Julian day number (MJDN) in which the JDN of 1200 UTC 1 January 1970 is subtracted. (The reason for using 1200 UTC 1 January 1970 is that a Julian day begins at noon UTC, not midnight.)

7. Collocation software

In preparing a set of programs to deal with collocation, the authors recommend that whatever the computer language being used, routines be available to compute the following:

1) The sum, difference, dot product, cross product, and angle between two 3D Cartesian vectors, so that

vectors can be used as entities, and not dealt with by their three separate components.
2) The position in either the CFR or the TFR of a meteorological satellite at a given time, given the orbital parameters.
3) From a position in either the CFR or TFR the corresponding position in the other frame of reference, with latitude/longitude as a variant in the TFR.
4) The position on the surface of the earth directly beneath the known position of a satellite, considering the ellipsoidal shape of the earth, and the possibility that a satellite may experience an attitudinal perturbation;
5) Either geodetic or geocentric latitude from the other;
6) The time at which a satellite is directly over or abeam of a given point on the earth's surface, that is, a general inverse navigation algorithm, or a solution of Eq. (2).
7) Time expressed in one system (civil calendar, coordinated universal time, elapsed seconds from an epoch, Julian day number or a variant of it, etc.) from its value in another system.

The computer programming needed to accomplish collocation can be done in any language with which the programmer feels comfortable. The language used by the authors was Meteorological FORTRAN (MeteFor), an enhancement of FORTRAN-77 developed at the Space Science and Engineering Center, Madison, Wisconsin, that incorporates vector and matrix algebra within its syntax. This allows, for instance, lengthy vector expressions to be contained within a single line of code.

Acknowledgments. We would like to acknowledge the NASA Atmospheric Product Evaluation and Test Element (PEATE) Grant number NNX07AR95G for supporting this research. This research was funded under NASA grants.

REFERENCES

Aitken, A. C., 1956: *Determinants and Matrices*. 9th ed. Interscience Publishers, 144 pp.

Aoki, T., 1980: A method for matching HIRS/2 and AVHRR pictures of TIROS-N satellites. Meteorological Satellite Center Tech. Note, 2, 15–26.

Aumann, H. H., and Coauthors, 2003: AIRS/AMSU/HSB on the AQUA mission: Design, science objectives, data products, and processing systems. *IEEE Trans. Geosci. Remote Sens.,* **41,** 253–264.

Bowditch, N., 1977: *Waves Wind and Weather: Selected from American Practical Navigator*. D. McKay, 185 pp.

Holz, R. E., S. Ackerman, P. Antonelli, F. Nagle, R. O. Knuteson, M. McGill, D. L. Hlavka, and W. D. Hart, 2006: An improvement to the high-spectral-resolution CO_2-slicing cloud-top altitude retrieval. *J. Atmos. Oceanic Technol.,* **23,** 653–670.

——, S. A. Ackerman, F. W. Nagle, R. Frey, S. Dutcher, R. E. Kuehn, M. A. Vaughan, and B. A. Baum, 2008: Global Moderate Resolution Imaging Spectroradiometer (MODIS) cloud detection and height evaluated using CALIOP. *J. Geophys. Res.,* **113,** D00A19, doi:10.1029/2008JD009837.

Justice, C. O., and Coauthors, 1998: The Moderate Resolution Imaging Spectroradiometer (MODIS): Land remote sensing for global change research. *IEEE Trans. Geosci. Remote Sens.,* **36,** 1228–1249.

Li, J., C.-Y. Liu, H.-L. Huang, T. J. Schmit, W. P. Menzel, and J. Gurka, 2005: Optimal cloud-clearing for AIRS radiances using MODIS. *IEEE Trans. Geosci. Remote Sens.,* **43,** 1266–1278.

Montenbruck, O., and T. Pfleger, 2000: *Astronomy on the Personal Computer*. 4th ed. Springer, 300 pp.

Smart, W. M., 1977: *Textbook on Spherical Astronomy*. 6th ed. Cambridge University Press, 431 pp.